

*ANATOMICAL AND FUNCTIONAL
CHARACTERIZATION OF THE MOUSE
INSULAR CORTEX*



Daniel Gehrlach

Dissertation

der Fakultät für Biologie

der Ludwig-Maximilians-Universität München

München, den 16.01.2020

Erstgutachter: Prof. Dr. Rüdiger Klein

Zweitgutachter: Prof. Dr. Laura Busse

Tag der Einreichung: 16.01.2020

Tag der mündlichen Prüfung: 19.06.2020

Eidesstattliche Erklärung

Ich versichere hiermit an Eides statt, dass die vorgelegte Dissertation von mir selbständig und ohne unerlaubte Hilfe angefertigt ist.

München, den16.01.2020..... Daniel Gehrlach
.....
(Unterschrift)

Erklärung

Hiermit erkläre ich, *

- dass die Dissertation nicht ganz oder in wesentlichen Teilen einer anderen Prüfungskommission vorgelegt worden ist.

- dass ich mich anderweitig einer Doktorprüfung ohne Erfolg **nicht** unterzogen habe.

- dass ich mich mit Erfolg der Doktorprüfung im Hauptfach
und in den Nebenfächern
bei der Fakultät für der
(Hochschule/Universität)
unterzogen habe.

- dass ich ohne Erfolg versucht habe, eine Dissertation einzureichen oder mich der Doktorprüfung zu unterziehen.

München, den.....16.01.2020..... Daniel Gehrlach
.....
(Unterschrift)

*) Nichtzutreffendes streichen

ABSTRACT

The insular cortex (IC) processes sensory information from within and outside the body and has been implicated in emotion regulation and homeostasis. To date, there is no comprehensive connectivity map of the mouse IC. Therefore, in the first part of this thesis, I created a whole-brain connectivity map of long range connections of the mouse IC. The IC was subdivided into three equally long parts (anterior, medial and posterior IC). Then, I performed cell-type specific monosynaptic rabies tracings to quantify afferent connections of excitatory and inhibitory IC neurons, while adeno-associated viral tracings allowed the detection of excitatory efferent axons. My analyses revealed that all parts of the insula are highly interconnected with multiple cortical and subcortical brain regions, which implies a complex integration of multi-sensory and emotional information in each insular subdivision. The anterior IC displays a distinctive connectivity pattern compared to the medial and posterior IC. While the connectivity of the mIC and pIC suggests a primary role in visceral and sensory integration, the aIC seems to play a central role in manipulating goal-directed motor behavior. These results provide an anatomical framework to guide the design of mechanistic investigations as well as working models of insular cortex function.

In the second part of this thesis, I combined insights from optogenetic behavior experiments, fiber photometry-based calcium imaging and the above-mentioned anatomical data to reveal a role of the posterior insula in processing aversive sensory stimuli and bodily states. By performing projection-specific optogenetics, I functionally characterized an insula-to-central amygdala pathway and could show that it mediates anxiety-related behaviors, while an independent nucleus accumbens-projecting pathway regulates feeding upon changes in bodily state.

In summary, the data presented in this thesis support a model in which the insular cortex detects aversive internal states and subsequently manipulates behavior, providing a mechanistic framework for IC function. These findings might aid in understanding how alterations in insula circuitry contribute to neuropsychiatric conditions such as obesity or anorexia, addiction and depression.

ACKNOWLEDGEMENTS

First, I want to thank Nadine Gogolla for giving me the opportunity and trust to help starting up her lab and performing my doctoral studies under her supervision. She was a great mentor that heavily influenced me and my scientific thinking during the last 5 years. On top of that, it was a humbling experience to be one of the first PhD students in a junior group.

I would also like to acknowledge my thesis advisory committee members Ilona Grunwald-Kadow and Bastian Hengerer for their valuable input.

I'm deeply thankful for the intense collaboration and *teamgeist* our lab developed, especially with Alex, Nate, and our (Master-) students Arthur, Daniela, Michaela and Caro. I am also grateful for the support of Marion Ponserre, who shared valuable information and reagents for rabies tracings.

Next, I want to thank Tom Gaitanos for helping me with the analysis of the anatomy study. Further, I am thankful for Alja's and Tom's helping hands during the revisions for my first paper.

Most importantly, I want to thank my parents Cristina and Helmut Gehrlach as well as my wife Ellen for always supporting and believing in me. I would be nothing without them and they deserve all the credit. Thank you!

CONTENTS

1 INTRODUCTION.....	1
1.1 ANATOMY OF THE RODENT INSULAR CORTEX.....	1
1.1.1 <i>Cyto- and Chemoarchitecture of the Insular Cortex</i>	2
1.1.2 <i>Connectivity of the Mouse Insular Cortex</i>	2
1.2 FUNCTIONS OF THE INSULAR CORTEX.....	3
1.2.1 <i>Interoception</i>	3
1.2.2 <i>Autonomous Functions</i>	4
1.2.3 <i>Food Consumption and Gustation</i>	4
1.2.4 <i>Nociception</i>	5
1.2.5 <i>Fear and Anxiety</i>	6
1.2.6 <i>Social Interaction</i>	6
1.2.7 <i>Addiction</i>	7
1.2.8 <i>Conclusion</i>	7
1.3 ANATOMICAL TRACING TECHNIQUES.....	8
1.3.1 <i>Monosynaptic Retrograde Rabies Tracing</i>	8
1.3.2 <i>Axonal Anterograde Viral Tracing</i>	10
1.4 OPTOGENETICS.....	10
1.5 FIBER PHOTOMETRY.....	11
1.6 RODENT BEHAVIORAL TESTING.....	12
1.7 AIMS OF THE STUDY.....	16
2 RESULTS.....	17
2.1 WHOLE-BRAIN CONNECTIVITY MAP OF THE MOUSE INSULAR CORTEX.....	17
2.1.1 <i>Starter Cell Characterization for RV and AAV Tracings</i>	17
2.1.2 <i>Whole-Brain Connectivity Map of IC</i>	19
2.1.3 <i>Pair-wise Correlations of Rabies and AAV tracings</i>	20
2.1.4 <i>IC - Amygdala Connectivity</i>	23
2.1.5 <i>IC – Striatum Connectivity</i>	25
2.2 FUNCTIONAL CHARACTERIZATION OF POSTERIOR INSULAR CORTEX.....	27
2.2.1 <i>Optogenetic Stimulation of IC Induces a Mixture of Aversive Behaviors</i>	27
2.2.2 <i>Bulk Calcium Imaging of IC Activity during Anxiety-Related Behavioral Tests</i>	32
2.2.3 <i>Optogenetic Manipulation of pIC during Anxiety-related Tests enables Bi-directional Modulation of Anxiety-like Behavior</i>	35
2.2.4 <i>pIC→CeA and pIC→NAcc projector neurons form non-overlapping populations..</i>	41
2.3 FUNCTIONAL CHARACTERIZATION OF PIC→CEA AND PIC→NAcc.....	44
2.3.1 <i>Stimulation-induced Behaviors</i>	46
2.3.2 <i>Real-time Place Aversion Assay</i>	47

2.3.3 Breathing Rate.....	48
2.3.4 Real-time Optogenetic Manipulation during EPM and EZM.....	49
2.3.5 Sucrose Preference Test.....	51
2.3.6 Feeding under Optogenetic Stimulation.....	54
2.3.7 Quinine Avoidance Test.....	55
2.3.8 Social Interaction.....	56
2.3.9 Lithium Chloride-induced Anorexia.....	57
2.3.10 Fear-induced Anorexia.....	58
2.3.11 Controlling for Back-propagating Action Potentials induced by Projection-specific Stimulations.....	60
3 DISCUSSION.....	62
3.1 CONNECTIVITY OF THE MOUSE INSULAR CORTEX.....	62
3.2 FUNCTIONAL CHARACTERIZATION OF PIC.....	66
3.2.1 Global pIC Manipulation.....	66
3.2.2 pIC-to-Central Amygdala Pathway.....	67
3.2.3 pIC-to-Nucleus Accumbens Core Pathway.....	69
3.3 LIMITATIONS OF THE STUDY.....	71
4 MATERIALS AND METHODS.....	73
4.1 ANIMALS.....	73
4.2 VIRAL CONSTRUCTS.....	75
4.3 STEREOTAXIC SURGERIES.....	75
4.4 HISTOLOGY.....	76
4.5 IMAGE PROCESSING AND DATA ANALYSIS OF TRACINGS.....	77
4.6 HEART- AND BREATHING RATE MEASUREMENTS IN ANAESTHETIZED MICE.....	80
4.7 BEHAVIORAL TESTS.....	80
4.8 FIBER PHOTOMETRY.....	85
4.9 STATISTICAL ANALYSIS.....	88
5 REFERENCES.....	91
6 APPENDICES.....	107

LIST OF ABBREVIATIONS AND ACRONYMS

2P	Two-photon
5-HT	Serotonin
AAV	Adeno-associated virus
aBLA	Basolateral amygdala, anterior part
ACC	Anterior cingulate cortex
aIC	Anterior insular cortex
AIP	Agranular insular cortex, posterior
AP	Anterior-posterior
APir	Amygdalo-piriform transition area
APs	Action-potentials
Au2	Auditory cortex, secondary
BDA	Biotinylated dextran amine
BDNF	Brain-derived neurotrophic factor
BLA	Basolateral amygdala
BNST	Bed nucleus of the stria terminalis
BW	Body weight
CamKII	Ca ²⁺ /calmodulin-dependent protein kinase
CAV2	Canine adenovirus
CeA	Central amygdala
CeC	Central amygdala, capsular part
CeL	Central amygdala, lateral part
CeM	Central amygdala, medial part
CGIC	Caudal granular insular cortex
ChR2	Channelrhodopsin-2
CM	Centromedian nucleus of the thalamus
CNO	Clozapine-n-oxide
CPu	Caudate putamen

CTA	Conditioned taste aversion
CTB	Cholera toxin subunit B
D1R	Dopamine 1 receptor
D2R	Dopamine 2 receptor
DI	Dysgranular insular cortex
DMT	Dimethyltryptamine
DREADD	Designer receptors exclusively activated by designer drugs
DV	Dorso-ventral
ECT	Ectorhinal cortex
ENT	Entorhinal cortex
EnvA	Envelope protein A
EPM	Elevated-plus maze
eYFP	Enhanced yellow fluorescent protein
EZM	Elevated-zero maze
fMRI	Functional magnetic resonance imaging
GABA	Gamma-aminobutyrate
GFP	Green fluorescent protein
GI	Granular insular cortex
GRIN	Gradient index
HSV	Herpes simplex viurs
IC	Insular cortex
IPAC	Interstitial nucleus of the posterior arm of the anterior commissure
LA	Lateral amygdala
LFP	Local field potential
LH	Lateral hypothalamus
LiCl	Lithium chlordie
LSD	Lsyergic acid diethylamide
LTD	Long-term depression

LTP	Long-term potentiation
M1	Motor cortex, primary
MD	Mediodorsal nucleus of the thalamus
MeA	Medial amygdala
mIC	Medial insular cortex
ML	Medio-lateral
mPFC	Medialprefrontal cortex
MSN	Medium-spiny neuron
NAc	Nucleus accumbens
NAcc	Nucleus accumbens core
NBQX	(2,3-Dihydroxy-6-nitro-7-sulfamoyl-benzo[f]chinoxalin-2,3-dion)
NpHR3.0	Halorhodopsin 3.0
NTS	Nucleus of the solitary tract
OF	Open field test
OFC	Orbitofrontal cortex
pBLA	Basolateral amygdala, posterior part
PBN	Parabrachial nucleus
pIC	Posterior insular cortex
Pir	Piriform cortex
PRh	Perirhinal cortex
RAIC	Rostral agranular insular cortex
ROI	Region of interest
RTPA	Real-time place aversion
RTPP	Real-time place preference
RV	Rabies virus
S1	Somatosensory cortex,primary
S2	Somatosensory cortex,secondary
SPECT	Single photon emission computertomography

SSRIs	Selective serotonin reuptake inhibitors
TMT	Trimethylthiazoline
TVA	Cellular receptor for subgroup A avian leukosis viruses
VP	Ventral pallidum
VPL	Ventral posteriolateral nucleus of the thalamus
VPM	Ventral posteromedial nucleus of the thalamus
VPMpc	Ventral posteromedial nucleus of the thalamus, parvicellular part
WGA	Wheat germ agglutinine

1 INTRODUCTION

Affective as well as homeostatic states are strongly influencing ongoing behavior. These states arise from extended neural circuits through integration of internal and external stimuli^{1,2}. In particular, aversive states such as pain and negative moods tune behavior towards survival programs³. The insular cortex (IC) is a major cortical convergence site for internal and external sensory information⁴⁻⁸. While rodent studies suggest an important role for the insula in processing taste and bodily signals, human imaging studies have linked the IC with emotion processing and regulation^{5,8-10}. With this evidence, our laboratory hypothesized that the insula serves as an interface between bodily and emotional states. How this is mechanistically implemented is currently not known. In the following, I will briefly review the anatomy and function of the rodent insular cortex and introduce the main techniques that I used in this thesis.

1.1 Anatomy of the Rodent Insular Cortex

In animals that have a smooth-surfaced cortex, such as rats and mice, the insular cortex is located above the rhinal fissure on the lateral surface of the brain. The rodent insular cortex consists of several heterogeneous regions with distinct cytoarchitectural and connective features¹¹. In the following, I will introduce the cyto- and chemoarchitecture as well as the connectivity of the rodent insular cortex

1.1.1 Cyto- and Chemoarchitecture of the Insular Cortex

The insula is comprised of (at least) three cytoarchitecturally distinct areas, according to the presence of granular layer 4 neurons. Based on this presence, the insula is separated into the granular (GI), dysgranular (DI) and agranular insula (AI). While the GI is organized in the classical six-layered prototypical cortical arrangement, the DI shows a progressive loss of the fourth layer.

Where this loss is complete, the AI begins and is composed of only three soma carrying layers (2/3, 5 and 6)¹². AI, DI and GI form strong interconnections along the dorso-ventral and rostro-caudal axes^{13,14}. Along the rostro-caudal axis, the insula has been further divided into the anterior insula (aIC), and the posterior insula (pIC). In rats, these are also sometimes referred to as rostral agranular insular cortex (RAIC) and caudal granular insular cortex (CGIC). The cytoarchitectural argument for a division into anterior and posterior part of the insular is less clear. The delineation of aIC and pIC are rather based on connectivity and functional responses.

Chemoarchitectural features of the insular cortex include the presence of acetylcholinesterase in the agranular insula, strongly reduced myelination in dysgranular and agranular insula, absence of SMI-32 immunoreactivity in the entire insula and reduced number of parvalbumin-positive interneurons in the agranular insula¹⁵. Further, several neurotransmitter receptors are expressed, such as the D1- and D2 dopamine receptors¹⁶, β -Adrenergic receptors¹⁷, cannabinoid CB1-receptors¹⁸, serotonin receptors 5-HT_{1A}¹⁹, 5-HT_{2A}¹⁹, 5-HT_{2C}²⁰, 5-HT₃²¹ and possibly 5-HT_{4,5,6,7}²², μ -, δ -, and κ -opioid receptors²³ as well as nicotinic acetylcholine receptors²⁴.

1.1.2 Connectivity of the Mouse Insular Cortex

The connectivity of the insular cortex has been characterized in rats and primates, but so far not as a comprehensive quantitative dataset. For the mouse, very few tracing studies exist^{25,26}, however, the Allen Brain Mouse Connectivity Atlas²⁷ provides several anterograde axonal AAV tracings from regions including IC. Yet, a brain-wide input map of the IC is completely lacking for the mouse. However, what studies have shown so far is that the IC receives information from external as well as internal senses via brainstem, thalamic and cortical inputs. These afferents are topographically organized leading to functional specializations, such as the ‘visceral insular cortex’, the ‘gustatory cortex’ (the primary taste cortex), or the insular auditory and somatosensory fields and potential many more²⁸⁻³¹. Despite the specialization, it is important to note that these regions integrate cross-modal inputs as well³². Next to its sensory afferents, the limbic system reciprocally connects to the insular cortex; for example the LA and BLA¹³.

Further, the IC projects to BNST, the MD of the thalamus, the LH as well as to parahippocampal areas¹¹. The IC is also heavily interconnected with other cortical regions¹¹. Of interest in emotion-regulation and decision-making is its reciprocal connectivity with prefrontal areas such as the OFC, mPFC and ACC. These regions are heavily implicated in executive-, cognitive- and emotional processing³³. Further, the insular cortex, in particular the aIC has been shown to strongly project to the ventral striatum in primates^{34,35} and rats³⁶ and this connection has been implicated in behavioral flexibility in reward contexts^{37,38}.

Taken together, the IC and its subdivisions display a heterogeneous and extensive connectivity with limbic- sensory-, memory- and executive systems, which places the insula in a unique position for integration of multi-sensory, emotional and cognitive information. There is evidence that within the IC distinct connectivity profiles exist, suggesting different functional roles of the aIC and pIC.

1.2 Functions of the Insular Cortex

Human fMRI studies and electrophysiological recordings in primates and rats have revealed that the insula is involved in a plethora of situations but it is unclear what its exact role is³⁹. In the following, I will briefly introduce some key findings of the insular cortex stemming from both human and animal studies.

1.2.1 Interoception

Interoception – sensing the state of the body – has been correlated with activity in the insular cortex^{8,40}. Anatomically, this is supported by inputs from nuclei of the thalamus which convey information about the heartbeat, blood pressure, blood oxygenation levels, bowel movements, nociceptive stimuli, hunger, disgust, nausea, tickle, itch and many more^{5-7,10,40}. The posterior insula might be the first node in the brain, where all bodily information is integrated and monitored⁴⁰. Subsequent processing towards more anterior parts of the insula is thought to further integrate the emotional state, goals and memories⁴⁰. This positions the insula to detect salient stimuli regarding bodily integrity and homeostasis. Evidence supporting this, comes from experienced mindfulness meditators, which display an increased activation as well as an increased grey matter volume of the right anterior insula^{41,42}. Another very interesting finding that corroborates the role of IC in interoception and self-awareness came from the group of Robin Carhart-Harris in 2016. They wanted to image human brains under the influence of the

hallucinogenic compound LSD (lysergic acid diethylamide). After administration of LSD (i.v., 75 µg) the healthy volunteers were subjected to fMRI scans. Strikingly, the functional connectivity density of the insular cortex was highly correlated with self-reports of ego dissolution. This indicates a higher functional connectivity of the insular cortex with other cortical areas under the influence of LSD, possibly explaining out-of-body experiences or delusions to transform into an animal (lycanthropy)⁴³. Another potent psychedelic substance Dimethyltryptamine (DMT), which is the main ingredient in the ancient shamanic Amazonian brew “Ayahuasca”, has strong anti-depressant and ego-dissolving effects. Interestingly, healthy and depressed subjects receiving Ayahuasca and undergoing single photon emission tomography (SPECT) displayed a strong modulation of insular cortex activity^{44,45}. Almost all of the other functions of IC that I will discuss below might eventually be related back, at least in part, to the interoceptive role of the insular cortex.

1.2.2 Autonomous Functions

In addition to sensing bodily aspects – i.e. interoception – the insular cortex can also affect autonomic functions directly, such as regulating the heartbeat, blood pressure or bowel movements⁴⁶⁻⁵⁰. It is unclear, *via* which pathways these effects could be mediated, but likely candidate projections include those to the BNST, CeA, LH or PBN. Studies in rats uncovered adjacent ‘pressor’ and ‘depressor’ sites within the pIC by electrical microstimulation in anesthetized animals⁵¹. Stimulation of these sites displayed opposing effects on the heart rate and blood pressure. This implies the existence of separated and antagonistic circuits very close to each other within the insula. This makes the insula an interesting structure in the etiology of psychosomatic disorders.

1.2.3 Food Consumption and Gustation

Multiple neuroimaging studies in humans and experiments in rodents revealed the contribution of the insula in gustation^{52,53}, for visual food cues^{54,55}, or olfactory food cues⁵⁶, but also during craving for food⁵⁷. Ultimately, eating is a multimodal experience composed of taste, smell and texture⁵⁸. These sensory cues are thought to be combined within the anterior insula, as suggested by overlapping activation of parts of the anterior insula after independent stimulation with odor and taste cues^{59,60}. In addition, the viscosity and texture of food is correlated with activity in the

aIC and mIC^{61,62}. An important role of the assessment of the consumed food is how one's body feels after having eaten. This relates to the interoceptive role of the insula, as described above⁴⁰.

Another supporting evidence that the IC is implicated in gustation and consummation of food is insular pathophysiology in eating disorders. A meta-analysis found a decreased mIC activity in overweight compared to lean subjects⁶³. The authors hypothesize that a maladaptive interoception, causing a misinterpretation of appetite signals of the gut, could increase food intake in obese subjects.

Conditioned Taste Aversion

Conditioned taste aversion (CTA) is an acquired avoidance of a novel taste (= conditioned stimulus) if it has been previously paired with the sensation of visceral malaise or sickness (= unconditioned stimulus)⁶⁴⁻⁶⁶. In animal models, this can be reliably induced by pairing a novel taste with the administration of lithium chloride (LiCl)⁶⁴. The mechanisms mediating conditioned taste aversion have been extensively studied in rats and mice and revealed, that lesions or pharmacological silencing encompassing the insular cortex prevent the acquisition, storage and expression of conditioned taste aversion to novel but also to familiar tastes⁶⁷⁻⁷⁰. Further studies showed the involvement of cholinergic and dopaminergic signaling in regulating insular plasticity during CTA^{71,72}. Recently, Lavi et al. found that conditioned taste representations within the IC selectively shift to BLA-projecting IC neurons⁷³. These results suggest the presence of valence-specific neurons with a direct influence on the expression of taste aversion. Through learning, sensory stimuli are assigned to such valence-specific neurons, or in the case of innate preference for sucrose or avoidance of bitter taste, may be hard-wired.

To summarize, the aIC and mIC seem to be multimodal integration hubs for the processing of food-related stimuli and maladaptive responses in these areas could underlie or promote obesity. Further, the insular cortex plays a pivotal role in the acquisition, storage and recall of conditioned taste aversion.

1.2.4 Nociception

Noxious somatosensory stimuli often activate the insular cortex, which has been suggested to play an important role in pain processing⁷⁴⁻⁷⁶. The pIC responds to the somatosensory aspects of pain, while the aIC has been shown to mediate its affective features⁷⁷. Accumulating evidence implicates anatomical and functional alterations in the IC in the expression of chronic pain and with cognitive and affective disorders⁷⁸. Interestingly, alterations in insular grey matter volume

due to chronic pain could be partially reversed after successful therapy of trigeminal neuralgia⁷⁹. The role of the insula in pain is again closely intertwined with interoception, particularly, in the shaping of pain perception. Here, the aIC integrates multimodal information including nociception to give rise to the affective dimensions of pain.

1.2.5 Fear and Anxiety

Human imaging studies as well as animal studies have revealed a role for the insular cortex in representing positive and negative emotions, such as anger, sadness, fear and anxiety, disgust, happiness or joy, trust, surprise, as well as social emotions^{39,40,80}. Emotional stimuli of various modalities, such as touch, vision or olfaction, elicit IC responses. Thus, a growing number of studies suggest an important role for the IC in fear and anxiety^{10,39,40,81}. Human fMRI experiments detected a functional and structural connectivity of the IC with other limbic brain areas, in particular with the amygdala and the strength of this connectivity has been shown to correlate with the anxiety levels of healthy subjects^{81,82}. In animal studies, electrophysiological recordings during fear-conditioning experiments revealed a population that responds to freezing and extinction within pIC⁸³. Furthermore, irreversible lesion experiments as well as temporary pharmacological inhibition of the rat IC revealed a role of the IC in consolidation of learned fear^{84,85}. Interestingly, the IC seems to be also involved in the learning of safety cues, which signal the absence of the unconditioned stimulus^{86,87}. Therefore, both fear increasing as well as fear reducing circuits were found within the IC.

1.2.6 Social Interaction

Social animals need to be able to recognize and transmit social cues that facilitate and enable social interaction⁸⁸. This is achieved by the social-decision-making network⁸⁹, which is thought to include the insular cortex, as lesions of IC in humans and rodents results in deficits in emotion recognition and empathy⁹⁰⁻⁹³. This is further supported by changes in insular cortex activity and connectivity in autistic subjects⁹⁴⁻⁹⁶. Of particular interest in the context of social interaction is the oxytocin-releasing projection from the paraventricular nucleus of the hypothalamus to the agranular insula⁹⁷. A recent study in rats has shown that oxytocin-release in the IC orchestrated approach or avoidance to stressed or non-stressed conspecifics⁹⁸. A follow up study by the same lab identified the projection of the IC to the NAc to modulate social approach⁹⁹. As social interaction seems to be based on recognizing one's own bodily and emotional state and integrate it with those of a conspecific, the interoceptive function of insular cortex make it a prime candidate for modulating social interactions.

1.2.7 Addiction

Addiction, also defined as “substance use disorder” in the DSM-5 (Diagnostic and Statistical Manual of Mental Disorders, 5th edition), is a mental disease that is defined by compulsive drug use and seeking despite negative consequences¹⁰⁰. Furthermore, frequent relapse behavior is characteristic of addictive behavior¹⁰⁰. Functional imaging studies in addicted human subjects have repeatedly and across several drugs of abuse detected correlations of insula activity upon drug consumption and drug seeking¹⁰¹. In addition, grey matter volume of the insular cortex is reduced in cocaine addicts¹⁰². In a very interesting analysis, Naqvi et al. report that stroke patients with lesions including the insular cortex, display an immediate and long lasting cessation of smoking in heavy smokers. These patients reported a lack of conscious bodily urge to smoke after the stroke. This was not the case in stroke patients where the insular cortex was not affected by the stroke¹⁰³. Rodent studies have further supported the role of the insula in the formation of amphetamine-induced conditioned place preference, a model for drug seeking behavior⁴. Another study in rats has found that aversion-resistant intake of alcohol is sustained by glutamatergic projections from the insula and mPFC to the nucleus accumbens core¹⁰⁴. Further, intra-venous self-administration of nicotine in rats was reduced upon infusion of a dopamine D1-receptor antagonist into the insular cortex, showing the importance of the dopamine system in the insular cortex for drug rewards¹⁰⁵.

These studies in rodents and humans suggest two modes of action by which the IC could influence addictive behavior. First, the acute urge to seek and consume a drug – i.e. craving, seems to be manifested *via* the IC. Second, aversion-resistant drug consumption might be caused through maladaptation of insular circuits that would otherwise terminate ongoing drug use.

1.2.8 Conclusion

As introduced above, the insular cortex has been implicated in a broad variety of functions, from taste over pain to addiction. Although at first many functions seem to be unrelated to each other or incoherent, a general finding shared across different species does emerge. The insula serves as a hub where various sensory, emotional and memory systems are integrated. Through its afferents, the insular cortex is in a perfect position to monitor the internal as well as external environment of an organism. Further, the insula adapts its predictions of future internal states through learning, as is evident by conditioned taste aversion. It therefore plays an important role in capturing the valence of internal or external stimuli, which might be maladapted, e.g. in drug or food addiction. These findings could explain why insula integrity is necessary for learning, emotion regulation,

and decision-making. In addition, evidence points to the fact that the insula is part of a salience detection network, which prioritizes the processing of acutely relevant stimuli. How exactly this is implemented on a mechanistic or cellular level is currently unknown. We also have little information about the function of specific output pathways or how such circuits might differ in their connectivity.

1.3 Anatomical Tracing Techniques

1.3.1 Monosynaptic Retrograde Rabies Tracing

Non-viral tracing techniques, such as Cholera toxin subunit B (CTB), biocytin, biotinylated dextran amine (BDA), wheat germ agglutinin (WGA), fluorogold, retrobeads, and others, were invaluable in assessing the connectivity of the brain. However, these methods cannot account for cell-type specific differences of connectivity and they do not provide information about monosynaptic inputs.

Retrograde viral tracing techniques based on neurotropic viruses, such as herpes-simplex virus (HSV), canine adenovirus type 2 (CAV2) and rabies and pseudo-rabies virus (RV, PRV), exploited the ability to traverse (multi-)synaptic pathways while being amplified at every step. These methods required at least bio-safety level 2 laboratories and for multi-synaptic tracings, the timing of termination of the tracings determined how many synapses were traversed. As these viruses hijack the endogenous transport machinery, there can be a marked difference of how many synapses were traversed, depending on the physical length of the axons.

A major advance in rabies-based circuit tracing was the deletion of the glycoprotein “G” from the rabies genome, yielding RV Δ G, which is restricted to a single trans-synaptic retrograde traverse (i.e. monosynaptic)¹⁰⁶. In 2007, Wickersham et al. developed a cell-type specific monosynaptic retrograde rabies tracing technique by pseudotyping RV Δ G with the envelope protein A (EnvA) of the avian leukosis virus. This restricted rabies infection to cells that expressed the avian receptor TVA¹⁰⁷. By expressing the TVA receptor in a Cre-dependent manner, it became possible, to specifically trace direct inputs of genetically defined populations.

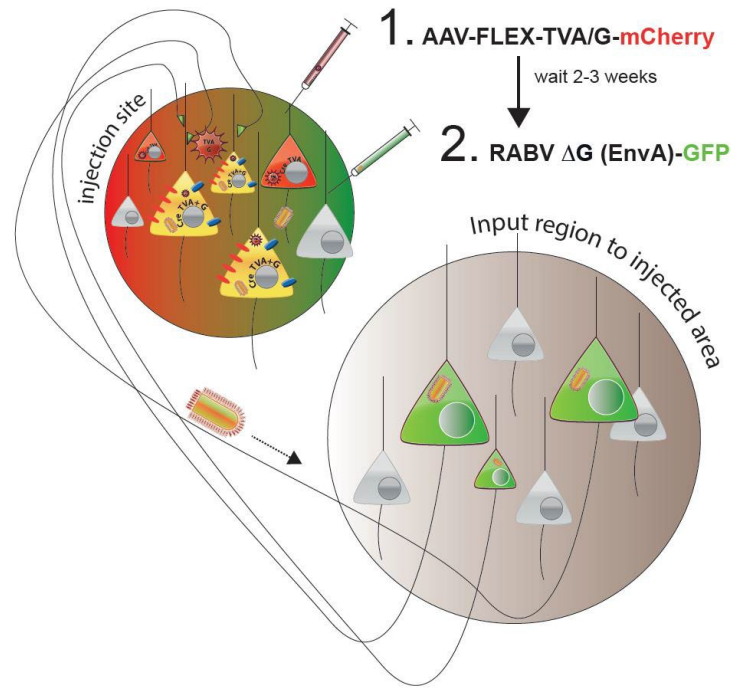


Figure 1. Schematic of cell-type specific monosynaptic rabies tracing. 1) A mixture of two Cre-dependent AAV helper constructs is injected into the target region. After 2-3 weeks, a sufficient expression of TVA and G should be achieved. 2) Then, the genetically modified rabies virus, lacking the gene for the G protein and pseudotyped with the EnvA capsid is injected into the same area. Neurons that were infected with both, the two helper constructs and the rabies virus represent the “starter cells” (yellow). The brain-wide presynaptic partners (input neurons) to these starter neurons will be retrogradely infected by the rabies virus and express GFP.

After retrogradely traversing from the starter neuron to the presynaptic partner, which must not express the G protein, a further trans-synaptic jump is not possible, thus only labeling direct monosynaptic input neurons.

This novel and powerful strategy was quickly adapted in the systems neuroscience field and has been used to trace from single neurons¹⁰⁸, from projection-defined neurons¹⁰⁹, from newborn cells¹¹⁰, and most frequently from genetically defined cell types using Cre driver lines^{111–116}.

Although various approaches are conceivable, most frequently, a Cre-dependent AAV construct coding for the G protein and the TVA receptor is injected into a brain region of interest in a Cre-driver mouse. After a period of 2-3 weeks allowing for sufficient expression of the gene products, a GFP-expressing EnvA-pseudotyped RABV Δ G is infused in a second stereotaxic surgery into the same region in order to infect the TVA- and G- expressing neurons (see **Figure 1**).

1.3.2 Axonal Anterograde Viral Tracing

In order to visualize brain-wide projections of neurons, neuroanatomists started using recombinant adeno-associated virus (AAV) expressing a fluorophore¹¹⁷. AAV vectors are based on non-pathogenic and defective human parvovirus and they cannot replicate without a helper virus. The major advantage of recombinant AAV (rAAV) is its very low toxicity and stable long-term expression of gene products¹¹⁸. Aside from anatomical tracing studies, this makes the AAV system an attractive technique to deliver gene therapy¹¹⁸.

The combination of the Cre-LoxP technology with rAAVs enables cell-type specific anterograde axonal tracings. To achieve this, the recombinant gene of interest, which is cloned into the AAV sequence, is flanked by two LoxP sites, rendering it dependent on the Cre-recombinase for efficient gene expression. In neurons that do not express Cre, very low levels of the gene product are observed. For anatomical studies, a fluorescent reporter protein such as the green fluorescent protein (GFP) are usually employed. GFP expression fills the entire neuron after a few weeks enabling the brain-wide visualization of its axons. This allows for a qualitative and quantitative measurement of innervation patterns of given cell-types.

1.4 Optogenetics

The development of optogenetics allowed neuronal manipulation *in-vitro* and *in-vivo* with a high-temporal and cellular precision¹¹⁹. The principal idea of optogenetics is to exploit the light-sensitivity of microbial opsins, to control ion-flow in neurons. Opsins are seven-transmembrane proteins, which exist in many variants, differing in their photocurrents, ion-specificity, kinetics and expression profiles. A major breakthrough was achieved in 2005 in Karl Deisseroth's lab at Stanford, which performed experiments expressing the algal protein Channelrhodospin-2 (ChR2) in cultured neurons¹²⁰. They could reliably control neuronal firing in a millisecond-timescale by applying blue light (473 nm). In the last 14 years many new genetically engineered and optimized opsins became available, leading to a large repertoire of specialized tools to either activate or inhibit neuronal spiking or gene expression, on varying time-scales.

The *in-vivo* use of optogenetics led to an unprecedented advance in understanding the function of neural circuits. By expressing activating or inhibiting opsins in genetically defined neurons and implanting optic fibers over these neurons to deliver light, we gained mechanistic understandings of circuits and their implications in behavior. An extensive introduction of current advances in optogenetics is out of scope of this thesis and I refer to the many excellent reviews and protocols

^{119,121,122}

However, very relevant to this thesis is the projection-specific manipulation of axon terminals *in-vivo*. This strategy specifically manipulates long-range projections of opsin-expressing neurons in a target region, by placing the optic fiber that delivers the light over that target region¹²¹. This enables the functional characterization of a specific pathway, without affecting the cell bodies of the opsin expressing neurons.

Nevertheless, there are caveats when applying optogenetics to study neural circuits *in-vivo*. Commonly, fixed stimulation frequencies, ranging from 1-60 Hz, have been used to stimulate large populations of neurons for one to many hundreds of seconds. Obviously, this pattern of activation does not resemble physiological firing of neurons and is highly artificial. Especially when assessing the behavioural outcome of these stimulations, one needs to consider that the observed behaviors might not occur in such a fashion in nature¹²³. However, compared to chemogenetic manipulation¹²⁴ or electrical microstimulation, optogenetics is still the most temporally precise tool to study genetically-defined neural circuits.

1.5 Fiber Photometry

Measuring neural responses *via* calcium imaging using genetically encoded calcium indicators, like the GCaMP¹²⁵ family, played an important role in the functional characterization of neural circuits in neuroscience. Two-photon imaging^{126,127} enabled the recording of many hundreds of single neurons in the layers 2/3 of cortex, and with recent advances in multi-photon imaging, neurons can be recorded up to >1 mm deep into cortex¹²⁸. However, these costly and delicate microscopes usually require the mice to be head-fixed or anesthetized. Single-photon calcium imaging of deep brain structures during freely moving behavior became possible with head-mounted miniature endomicroscopes¹²⁹, however, the weight (>2g) of such a microscope can be as much as 10-20 % of the bodyweight of a mouse. Further, to image deeper areas, the use of graded-index (GRIN) lenses is necessary, but the large diameter of these lenses (>500 μm) causes substantial damage to the brain. New two-photon miniature microscopes are being developed and show promising results¹³⁰, yet, the issue with the GRIN lenses and weight is not solved.

Alternatively, fiber photometry provides a comparably easy solution to record the bulk neuronal activity of genetically-defined populations^{131,132}. It makes use of the same multimode optical fibers that are also used for optogenetics and are implanted above the GCaMP-expressing neurons. Through the same fiber, excitation light is delivered to the neurons and the resulting fluorescent signal of the calcium indicator collected. Thus, the mobility of the mouse is only mildly affected and more complex behaviors, such as social interactions, can be studied. New multi-channel fiber photometry systems have emerged that allow simultaneous recordings of two¹³³ or more sites¹³⁴.

A disadvantage of fiber photometry is the loss of single neuron resolution, compared to microendoscopy. If the signal is recorded from a heterogeneous population, like in cortex, responses from sparse or rarely active populations might be underrepresented and those that fire in synchronicity or very frequently might be overrepresented. This issue can be tackled by further refining the cell-type specificity via projection targets or intersectional genetics. Nevertheless, the bulk activity can be a first step in characterizing the dynamics of a brain region.

1.6 Rodent Behavioral Testing

Behavior has been defined by Tinbergen as “the total movements made by the intact animal”¹³⁵. In order to understand how the brain generates a particular behavior, we need to identify the putative neural circuits that ultimately trigger the movement¹²³. In the case of emotion-related behaviors, exposing rodents to specific environments can trigger behaviors that resembles anxiety or fear in humans. Manipulating the activity or integrity of brain areas during such behavior has helped us identify and partially understand the neural circuits involved in motivated behavior. It is important to keep in mind that almost all commonly used behavioral tests use a reductionist approach to make a very specific set of behaviors amenable to neuroscientific analysis. A single behavioral test cannot and does not try to address all multifaceted and highly complex naturalistic behaviors at once. Instead, behavioral tests can be designed in such a way that they model very specific domains of behavior that can help us to eventually tackle the underlying causes for maladaptive disorders, such as anxiety, depression, or addiction. In the following, I will briefly introduce the behavioral tasks that will be used in this thesis.

Anxiety-related Behavioral Tests

Open Field Test

The open field test (OF) has been used in rodent behavioral research since 1934 and is one of the most frequently used instruments in animal psychology¹³⁶. It is so popular, because it is extremely simple to perform, does not require any training of the animal and there is a consensus on the interpretation of the results. Rodents are placed into a round or rectangular apparatus that is enclosed with walls and allowed to explore the novel environment. Originally, Hall developed the OF in 1934 to count the number of fecal boli of rats as an index of timidity¹³⁷. Over time, many more parameters have been added to the analysis of the OF. Today, most frequently assessed parameters are locomotor activity and the ratio between “time spent in the center” vs. “time spent in the periphery”. While stimulants such as amphetamine will strongly increase the

distance travelled in a OF, sedatives reduce locomotor activity^{136,138}. As rodents show an innate avoidance of brightly lit and open spaces, they will prefer to move along walls (thigmotaxis) and spend less time in the exposed center zone. Interestingly, the anxiolytic benzodiazepine diazepam increases the time spent in the center zone without affecting the total distance travelled¹³⁹. Since then, this constellation of results is considered to be indicative of an anxiolytic effect. Other measures related to the anxiety state of an animal include the stretched-attend position and rearings¹³⁶. Recent advances in quantification and characterization of behaviors by machine learning techniques enable sub-second classification of behaviors and provide novel ways of analyzing OF data¹⁴⁰.

Elevated-Plus Maze

The elevated plus maze (EPM) was first introduced in 1984 and relies on rodents' preference for darker and enclosed spaces and innate avoidance of heights and open spaces¹⁴¹. The EPM assesses the internal conflict of a rodent to avoid predation on one hand and to explore its surroundings for food and mating partners on the other hand. While the closed arms provide protection, the open arms expose the rodent to height and an open space, but also a potential – but ultimately not presented – reward. To perform the test, the animals are placed in the center of the maze facing a closed arm and their position in the maze is tracked for 5-10 min. The main readout for this behavioral task is the ratio of the time spent on the open arms vs. the closed arms, but parameters such as distance travelled, number of entries, number of stretched-attend postures, freezing or fecal boli might be of value¹⁴².

In general, mice will spend much more time in the closed arms and depending on the conditions (mouse strain, age, sex, handling, lighting, satiety, pre-exposure to novel environment, circadian rhythm, housing conditions, to name a few) between 5 and 30 % on the open arms.

What helped the EPM to gain traction in the preclinical research community was that compounds that display anxiolytic effects in humans, such as benzodiazepines, lead to an increase of time spent on the open arms, while leaving total distance travelled unaffected. In contrast, compounds that increase anxiety in humans also decreased the time spent on the open arms in rodents^{143,144}. This grants the EPM a high construct validity.

Nevertheless, criticism as a translation model of anxiety arose, as the EPM is only predictive for anxiolytic drugs acting on the GABAergic system, while newer compounds, e.g. 5-HT_{1A} antagonists or selective serotonin reuptake inhibitors (SSRIs), which have clinical evidence of anxiolysis in humans, do not influence the time spent on the open arms¹⁴⁵. Yet, the EPM and its variants, such as the elevated zero maze (EZM) remain the most popular anxiety-related tests to date.

Reward-related Behavioral Tests

Real-Time Place Preference or Avoidance

The Real-Time Place Preference (RTPP) or Real-Time Place Avoidance (RTPA) test is a modification of the classical conditioned place preference test (CPP)¹⁴⁶, but adapted to optogenetic manipulation. First, I will briefly introduce the CPP, which is an established test in neuropharmacological research to assess the motivational effects of psychoactive compounds. In essence, one compartment of a two-chambered behavioral apparatus is (repeatedly) paired with the administration of a compound of interest. Should the substance possess rewarding or habit-forming properties, animals will spend more time in the chamber that has been paired with the administration of the substance, as compared to the chamber where this pairing never occurred. In contrast, should the substance elicit aversive properties, the animals will avoid the paired chamber.

While the CPP assesses the memory of an outcome, the RTPP/RTPA enables the direct interrogation of the acute valence of an optogenetic stimulation. Analogous to the CPP, one of the two chambers is designated as the paired chamber, where optogenetic manipulation will occur. This is achieved by tracking the position of the animal in real-time and thereby constructing a closed-loop circuit which controls the laser emission. In case of a rewarding or pleasurable effect of optogenetic manipulation, the animals exhibit a real-time place preference. In contrast, aversive effects mediated by optogenetic manipulation should lead to reduced time spent in the stimulated chamber – a real-time place aversion. The RTPP has been a valuable tool in assessing positive or negative behavioral effects of optogenetic manipulations^{9,147–149}.

Sucrose Preference Test

The sensitivity to a hedonic stimulus, for example to a sucrose solution, can be tested with the sucrose preference test. The test measures, how much rodents prefer a sucrose solution over water. Under normal circumstances, most strains of rats and mice strongly prefer the sweet sucrose solution; however, when the animals become anhedonic, for example by exposing them to chronic stress or other models of depression, they reduce that preference. Therefore, the sucrose preference test is a very simple but yet powerful test to approximate the sensitivity to rewards. A major advantage of this assay is its technical simplicity. On the other hand, low reproducibility and high variability can be disadvantages. Interestingly, a study showed that the common practice of handling mice by their tails can decrease sucrose consumption and licking bouts¹⁵⁰. Therefore careful attention should be paid to adhering to a strict protocol when performing the sucrose test¹⁵¹. Important confounders are the duration of the test, the protocol for food and water deprivation, and the sucrose concentration of the solution.

As anhedonia presents a major symptom in depressed human patients but also in patients with schizophrenia, the sucrose preference test has been very frequently used in preclinical translational research¹⁵¹. Interestingly, administration of antidepressants, such as the SSRIs or tricyclic antidepressants, can restore the sucrose preference in rodent models of depression.

Social Interaction Test

Social motivation to interact with conspecifics is a powerful drive of humans and deficits in social interactions, as seen in autism spectrum disorder, can be very detrimental¹⁵². Mice are also a social species and exhibit many diverse social behaviors, such as reciprocal social interactions, social play, parenting, mating or aggressive behaviors¹⁵³. Researchers developed several behavioral assays to assess certain aspects of social behavior in mice¹⁵³. One of the most commonly used tests to measure social reward processing is the three-chamber social interaction test¹⁵⁴. Here, the animal can freely explore a maze in which one compartment of the chamber harbors another conspecific and the other compartment a non-social object. Under normal conditions, mice spend more time with the social stimulus than with a novel object. However, chronically stressed – i.e. “depressed” – animals reduce their social interaction time¹⁵³. Therefore, the social interaction test is another measure of the hedonic state of an animal, but not reliant on taste and thus an interesting complement to the sucrose preference test.

1.7 Aims of the Study

While anatomical investigations in diverse species highlight that the insular cortex is one of the most complex anatomical hubs in the mammalian brain^{50,155–158}, to date there is no comprehensive connectivity map of the mouse insular cortex.

Therefore, the **first goal of this thesis** was to map the input and output connectivity of IC excitatory as well as IC inhibitory neurons, by performing monosynaptic retrograde rabies tracings and anterograde axonal tracings of the mouse IC. I divided the IC into three equally large subdivisions, which I termed anterior, medial, and posterior insular cortex (aIC, mIC, and pIC, respectively). The resulting data set would serve as an anatomical framework to guide functional studies.

As the pIC has been hypothesized to be the entry point into the IC, the **second goal** was to functionally analyze the role of the pIC in emotion-related behavioral tasks. Previous work from the Zuker lab^{9,30,148} characterized the pIC in the processing of bitter taste, but evidence suggests that the pIC plays an important role beyond taste recognition^{4,86,159,160}. To clarify and further extend the idea that the pIC is involved in emotion-related processes, I employed optogenetic manipulations of the pIC during anxiety-related and consumption-related behavioral tasks.

Based on the anatomical findings I would obtain from the first goal, as a **third goal**, I wanted to then functionally characterize segregated IC populations that would project to interesting targets of the limbic system, such as the amygdala, mPFC, ventral striatum or ventral hippocampus and try to disentangle their specific roles.

2 RESULTS

2.1 Whole-Brain Connectivity Map of the Mouse Insular Cortex

2.1.1 Starter Cell Characterization for RV and AAV Tracings

I first checked the quality and distribution of the starter cell populations for both rabies virus (RV) tracings and adeno-associated viral (AAV) tracings with a CellProfiler pipeline that was created by myself with the help of T. Gaitanos, a further lab member (**Figure 2a, b** and Methods). For the RV tracings, I scored neurons as starter cells when they were double positive for eGFP (i.e. RV+) and mCherry (i.e. TVA+). For AAV tracings, starter neurons were detected as eYFP-positive cell bodies. This provided me with the total number and location of all starter cells, which are depicted in **Figure 2c**. The starter cell populations for the three IC subdivisions were separated and mostly non-overlapping for both AAV and RV tracings. In a few cases, a small amount of starter cells were found outside the IC (e.g. in Pir, S1 and S2, or M1). A comprehensive table containing information for all animals used for the anatomy study can be found in **Table 1** (Methods).

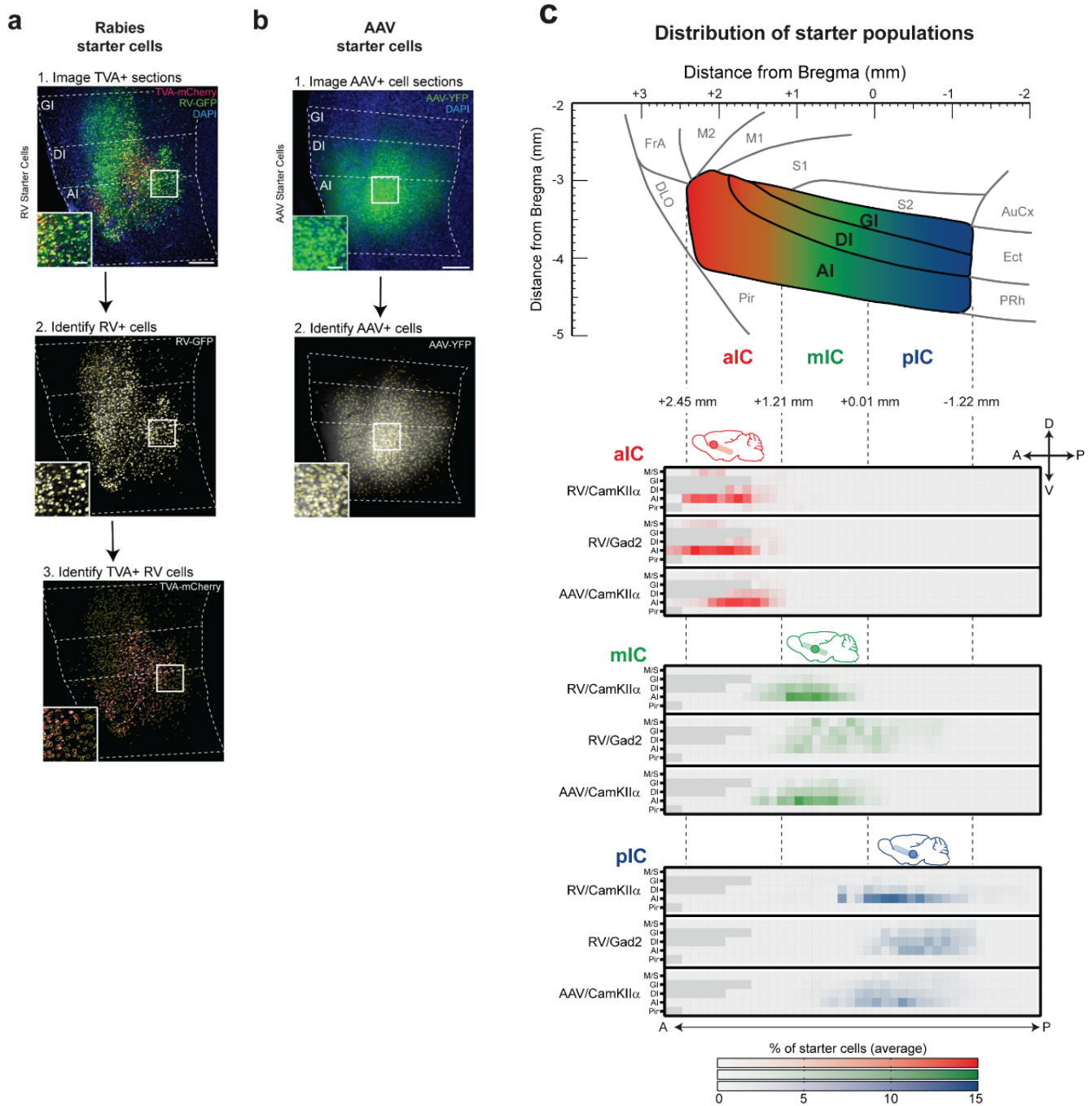


Figure 2. Characterization of starter neurons for RV or AAV tracings. a) Starter cell identification pipeline for Rabies tracings. 1. High resolution image of a representative section at the injection site in the IC. Starter cells are double-labelled with TVA-mCherry and RV-GFP, and appear yellow. Scale bars 200 μ m (main image), 50 μ m (inset). Number of starter cells was identified in an automated fashion using Cell Profiler. First RV+ cells were identified (image 2, yellow cell outlines) from the GFP image, then RV+ cells that also contain mCherry-TVA were identified from the mCherry signal (image 3, red rings within yellow RV+ cell outlines). Double labelled cells are counted as starter cells. b) Starter cell identification pipeline for AAV tracings. 1. Representative epifluorescent image of YFP-labelled AAV starter cells. Scale bars 200 μ m (main image), 50 μ m (inset). 2. YFP-positive cells were identified in an automated manner using Cell Profiler. c) Schematic illustration of the lateral view of the IC including distances from Bregma (top panel) and heatmap showing average starter cell distribution for each tracing strategy at each specific IC target (bottom panels). The three IC target subdivisions were mostly non-overlapping, and only a minimal percentage of cells were detected in the Motor and Sensory Cortex (M/S), or Piriform Cortex (Pir) neighboring the IC. $n = 3$ mice per injection site/tracing strategy. Heatmap intensity scale is the same for all three IC target subdivisions. Regions absent at specific Bregma levels are indicated by dark gray squares

2.1.2 Whole-Brain Connectivity Map of IC

To obtain an overview of the macro-scale IC connectivity, I created a brain-wide input and output connectivity map of excitatory and inhibitory neurons of the aIC, mIC and pIC. I segmented the data into 17 major brain regions that connect to the IC (**Figure 3**). As there was an order of magnitude difference between cortical and subcortical regions, I separated the data into these two categories for easier side-by-side comparison (**Figure 3**).

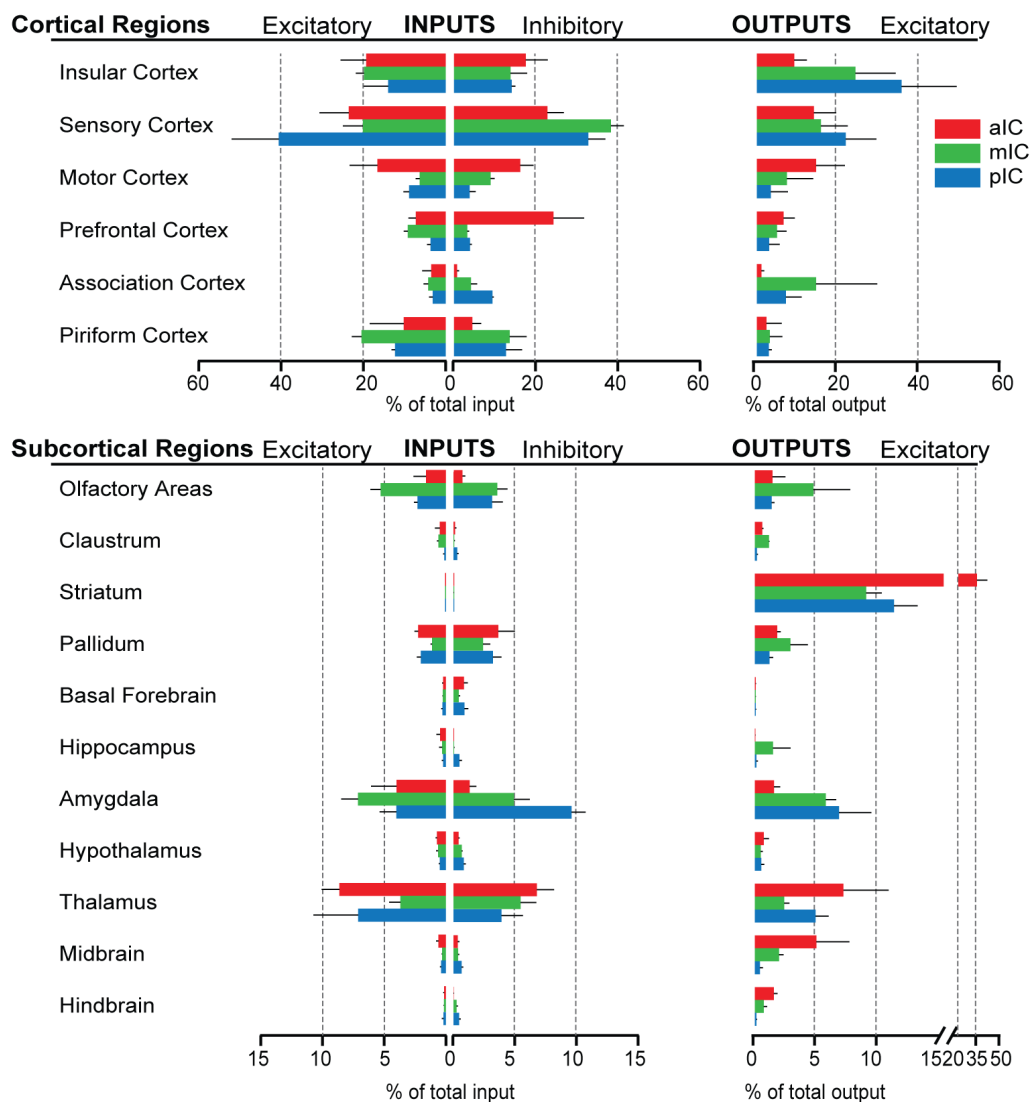


Figure 3. Whole-brain input and output map of the mouse insular cortex. Comparison of inputs to excitatory and inhibitory IC neurons (left) and outputs of excitatory neurons of the IC (right) of all three IC subdivisions (aIC, red; mIC, green; pIC, blue) across the 17 major brain regions that displayed connectivity. Region values are given as percentage of total cells (RV) or of total pixels (AAV). Data is shown as average \pm SEM. $n = 3$ mice per condition. Top panel shows cortical connectivity, bottom panel shows subcortical connectivity.

There were no substantial differences between the inputs to excitatory and inhibitory neurons, irrespective of the IC subdivision from which I traced. There was also no region, which solely innervated one of the three IC subdivisions. Yet, there were quantitative differences depending on region and IC subdivision. For example, there were around two times more inputs from the sensory cortex to the pIC ($41 \pm 11\%$ of total excitatory input connectivity) in comparison to the other IC subdivisions ($20 \pm 5\%$ and $23 \pm 7\%$ for mIC and aIC, respectively). In contrast, the motor cortex provided the majority of inputs to the aIC. In subcortical regions, the amygdala and thalamus provided most inputs to the IC.

While there was a strong bi-directional connectivity with other cortical regions, some subcortical regions showed a strong directional bias, favoring either inputs or outputs. For example the striatum, which did not project to the IC, but was heavily innervated by it. In particular, the aIC provided the strongest projection to the striatum ($32 \pm 6\%$, as compared to $9 \pm 1\%$ and $11 \pm 2\%$ for the mIC and pIC, respectively).

I also analyzed the data at a more detailed level, analyzing 75 brain areas separately. The resulting comprehensive data describe percent of total input to excitatory and inhibitory neurons, as well as outputs from excitatory neurons of the aIC, mIC and pIC. The tables containing these data can be found in the Appendix (see **Appendix 1, 2, 3**).

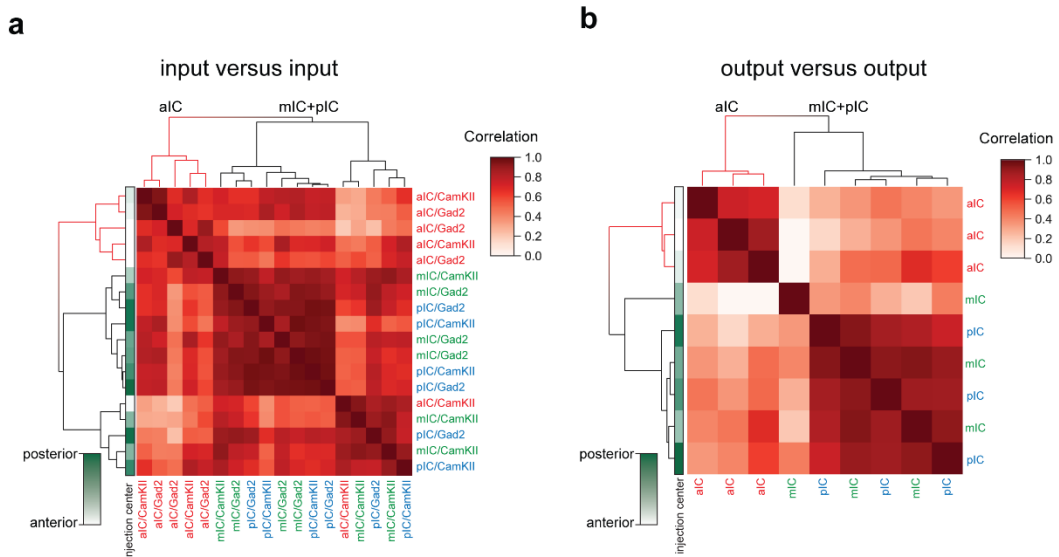
2.1.3 Pair-wise Correlations of Rabies and AAV tracings

Throughout my analysis, for both inputs and outputs, I noticed differences between the aIC, mIC and pIC. To test whether my observations could be confirmed by an unbiased statistical analysis, I correlated all input tracings (including inhibitory and excitatory mouse lines) to each other, as well as correlating all output tracings to each other. To do this, I calculated the pairwise correlation coefficients from the data of the 17 major brain regions (**Figure 4a,b**), but also at the highest resolution with all 75 regions of interest that have been used and applied a hierarchical clustering method (**Figure 4c,d**).

Comparing the data at the level of 17 major brain regions was chosen to detect a global and striking difference between major brain systems. This analysis showed that overall, the input-input comparisons displayed rather high correlation coefficients (**Figure 4a**, average correlation coefficients of 0.7 ± 0.16), indicating that across aIC, mIC and pIC for both excitatory and inhibitory neurons, inputs were scaling very similarly. The hierarchical clustering almost perfectly separated tracings from aIC (red labels and red dendrogram) of those from mIC or pIC, which were intermingled. The mIC and pIC cluster was further divided into two sub-clusters, however, this was neither due to injection site nor due to the genotype.

Surprisingly, when taking every ROI into account (**Figure 4c**, 75 brain regions) and performing the same analysis, the average of all correlations of the rabies tracings did not change (0.7 ± 0.17). This suggests that the main differences between the tracings are already evident at a higher level of the 17 major brain systems. Again, the hierarchical clustering grouped all except one tracing into the aIC cluster, while intermingling mIC and pIC tracings in the other cluster.

Comparing on the level of 17 major brain regions



Comparing on the lowest level of 75 brain areas

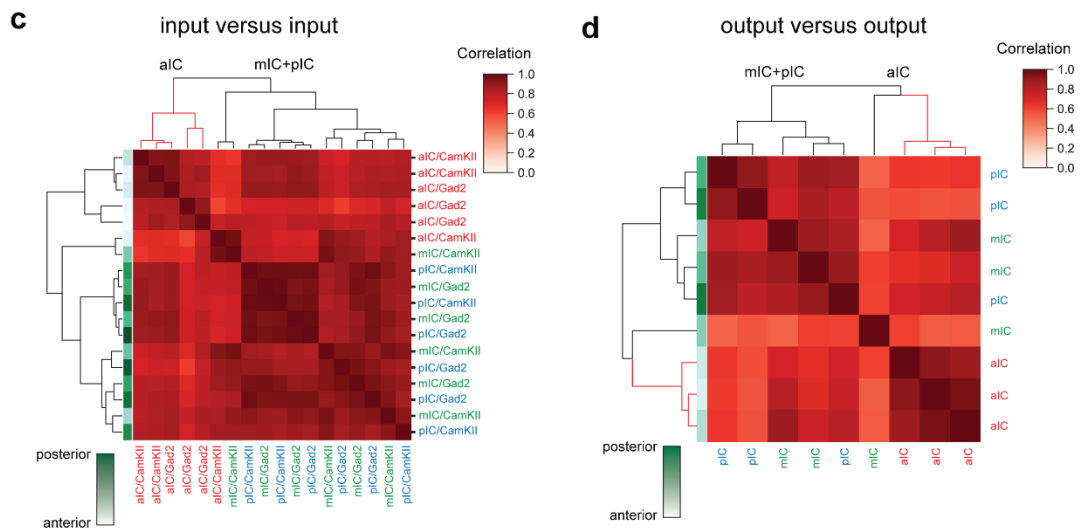


Figure 4. Hierarchical clustering separates aIC from mIC and pIC for inputs as well as outputs. This is the case when correlating averaged data of 17 major brain regions (a, b, higher hierarchy) and when correlating the lowest level of all 75 brain regions (c, d). Matrices of hierarchically clustered pair-wise correlation coefficients (Pearson's) of animals inputs vs. inputs a), c) or outputs vs outputs b), d). The pair-wise correlations were performed on the data organized into 17 major brain regions (see **Figure 3**), or on all 75 regions (see Appendices 1-3). Far left gradient bar (green hues) indicates the center of the starter cells, ranked relative to every mouse in the dataset. Note for both input and output correlations, a clear cluster forms from the aIC-targeted

animals (top left boxed sections and red-colored dendrograms), whereas the mIC- and pIC-targeted animals intermingle in a second cluster (larger boxed areas). Interestingly, the clustering algorithm did not separate excitatory (CamKII α) from inhibitory (Gad2) rabies tracings.

Analyzing the pairwise correlations for the AAV tracings at the 17 major brain region level, yielded an average correlation coefficient of 0.45 ± 0.28 (**Figure 4b**). This indicated that the outputs were still positively correlated with each other, but less so compared to the inputs vs. input correlations. Again, all three aIC AAV tracings were grouped into the same cluster, while AAV tracings from mIC and pIC were grouped together, except one outlier (mIC).

Repeating the analysis including all 75 regions yielded a very similar average correlation coefficient of 0.46 ± 0.27 . Again, this implies that most of variance is already captured with the 17 major brain regions.

To summarize, for both inputs and outputs, after applying hierarchical clustering, two distinct clusters formed, dividing the aIC animals from the intermixed mIC- and pIC mice. Indeed, for both input vs. input correlations as well as output vs. output correlations, the mIC and pIC tracings were interleaved, indicating a high degree of similarity between the medial and posterior regions of the IC. Neither the anterior-posterior coordinate of the starter cell population (left columns, green gradient), nor the cell-type from which I traced, could explain the sub-cluster within mIC and pIC targeted animals.

The striking difference of input- and output-patterns of aIC connectivity imply a functional difference as compared to mIC and pIC. In particular, for the efferents, a major difference arises from the strong projection to the striatum, and to a lesser extent, to the motor cortex (**Figure 3**). Overall, these findings suggest that the aIC might serve as a general output hub of IC.

2.1.4 IC – Amygdala Connectivity

The IC and amygdala are heavily interconnected through direct but also indirect pathways, some of which are reciprocal^{13,161–163}. Both regions are heavily implicated in emotional processing and I therefore focus on the IC-Amygdala connectivity in this section.

As expected, only cortex-like sub regions of the amygdala, such as the BLA or APir provided inputs to the IC subdivisions, whereas they were completely absent from striatum-like nuclei (CeA and MeA) (**Figure 5a, Figure 6a**). Interestingly, afferents from APir represented the only case where meaningful differences between tracings from excitatory and inhibitory neurons were detected.

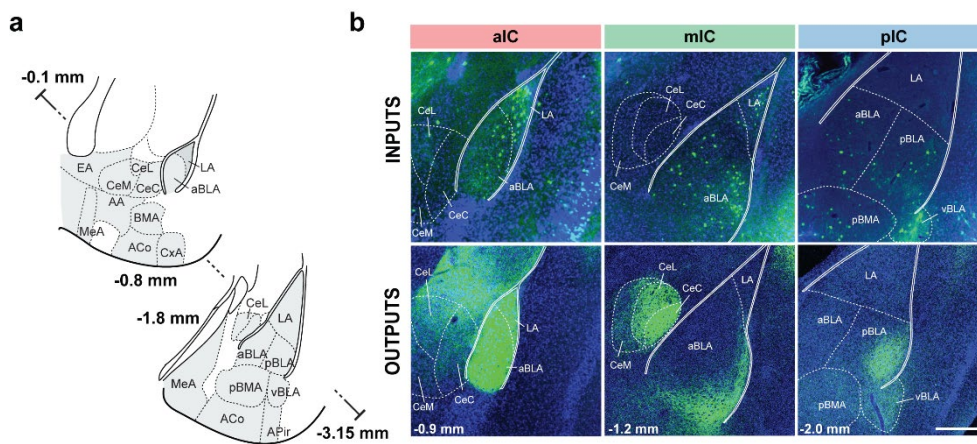


Figure 5. IC-amygdala connectivity. a) Coronal sections depicting the amygdala with its subregions. Distances are provided as anterior-posterior positions relative to Bregma. b) Representative images from excitatory inputs (top row, eGFP-expressing neurons) and outputs (bottom row, eYFP-positive neurons). Different Bregma levels are shown for each IC target site, as indicated on the images (-0.9 mm, -1.2 mm, -2.0mm). Scale bar = 200 μ m.

While inhibitory neurons of the aIC received very few inputs from the APir, excitatory neurons received considerably more (0.07% vs 1.50 %). In addition, I observed a pIC-to-aIC gradient regarding the APir inputs to the inhibitory neurons, with high input to pIC (>3% connectivity in the pIC) and very low to aIC.

Interestingly, only small variations were detected when comparing inputs from the amygdala to excitatory neurons between aIC, mIC and pIC, with the mIC receiving slightly more innervation. This finding was further supported by the analysis of input density, which revealed a broader rostro-caudal spread and higher density of mIC-projecting aBLA, pBLA and APir neurons (**Figure 6b**).

Regarding the outputs from the IC, all amygdalar regions were innervated except the MeA (**Figure 6a**). I found two opposing amygdala innervation gradients along the anterior-posterior axis of the IC. For instance, pIC strongly projected to the CeA, APir and pBLA, which confirms

retrograde CTB studies performed in rats and mice, respectively^{164,165}. In the second part of this thesis, I functionally analyzed the pIC→CeA pathway using optogenetics and could reveal an important role in anxiety-related behavior (see **Chapter 2.3**). On the other hand, the aIC mainly projected to the aBLA. Recently, this aIC-to-aBLA projection has been shown to elicit appetitive responses⁹. Further, the aIC did not innervate more posterior basolateral regions (pBLA), which can be seen in the innervation density plot in (**Figure 6b**). In addition, the aIC did not project to any other amygdaloid nucleus except from a sparse projection to the EA.

To summarize, there is a clear difference between the IC subdivisions when comparing outputs to the amygdala. Interestingly, the inputs to all subdivisions were quantitatively very similar.

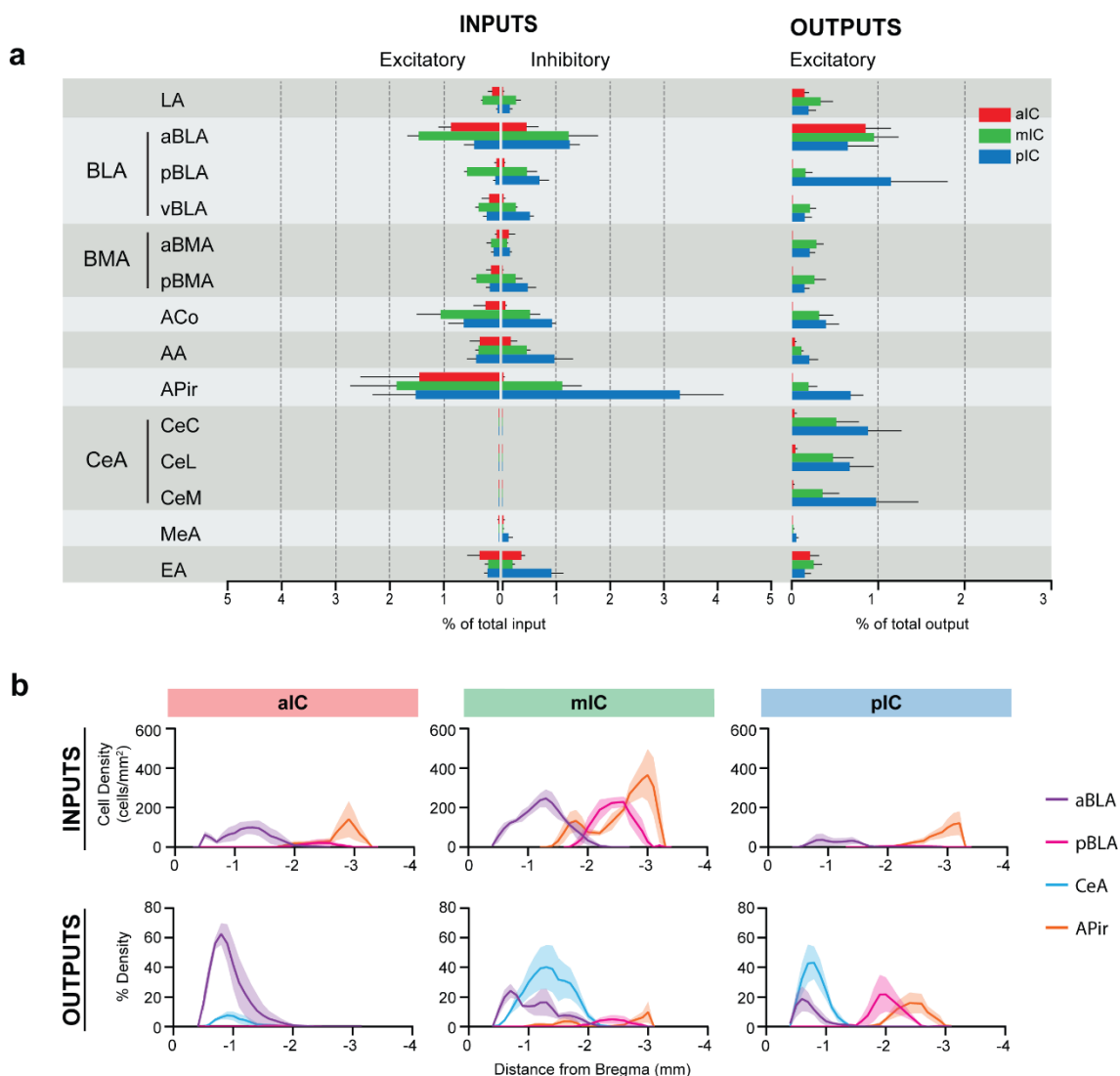


Figure 6. Quantification of Insula-Amygdala connectivity. a) Comparison of excitatory and inhibitory inputs detected in the amygdala (left) and excitatory outputs from the IC to the amygdala (right) in percent of total in- or output, respectively (aIC, red; mIC, green; pIC, blue). Data is shown as average \pm SEM. $n = 3$ mice per condition. b) Input cell density (top row) and percent output density (bottom row) plots along the anterior-posterior axis covering the entire amygdala. We selected aBLA, pBLA, CeA and APir to provide the areas with most differences between the IC subdivisions. $n = 3$ mice per condition. Data shown as average \pm SEM.

2.1.5 IC – Striatum Connectivity

In higher mammals, cortico-striatal projections have been shown to be topographically organized^{166,167} and play a role in goal-oriented behavior and initiation of movements¹⁶⁸. As I wanted to investigate the regulation of motivated behavior by the IC, the connectivity to the ventral striatum was of particular interest to me. As expected, there were no neurons projecting from striatum to cortex (**Figure 3**), and I therefore solely describe IC-to-striatum outputs in the following.

In accordance with a recent study¹⁶⁹, ventro-lateral parts of the striatum were more heavily targeted by IC projections than dorsal parts (**Figure 7b**). Notably, the vast majority of projections to the striatum arose from the aIC, which were high in density and spanning the ventro-lateral CPu along its entire rostro-caudal extent. Despite their low relative percentage of total outputs, the IPAC as well as the NAcc were densely innervated by aIC (**Figure 7d**).

The mIC and pIC also innervated the CPu, but much weaker than the aIC (ca. 5-fold lower). Yet, both mIC and pIC densely projected to the IPAC (to around 60% density). The NAcc was also innervated by the pIC, although much weaker than from mIC or aIC. In the second part of this thesis, I have functionally analyzed the pIC→NAcc projection using optogenetics (see **Chapter 2.3**) and could show that in spite of the relatively weak innervation, as compared to the mIC or aIC projection, consummatory behaviors could be potentially interrupted.

Overall, comparing mIC and pIC to each other, they displayed a very similar connectivity pattern to the striatum with 9% and 11% of total output, respectively. Remarkably, the aIC projection to the striatum represents the strongest output out of all regions innervated by aIC (31.8%).

To summarize, there is a noticeable difference in the projections to the striatum along the rostro-caudal axis of the IC, with the aIC being the most strongly connected part of IC.

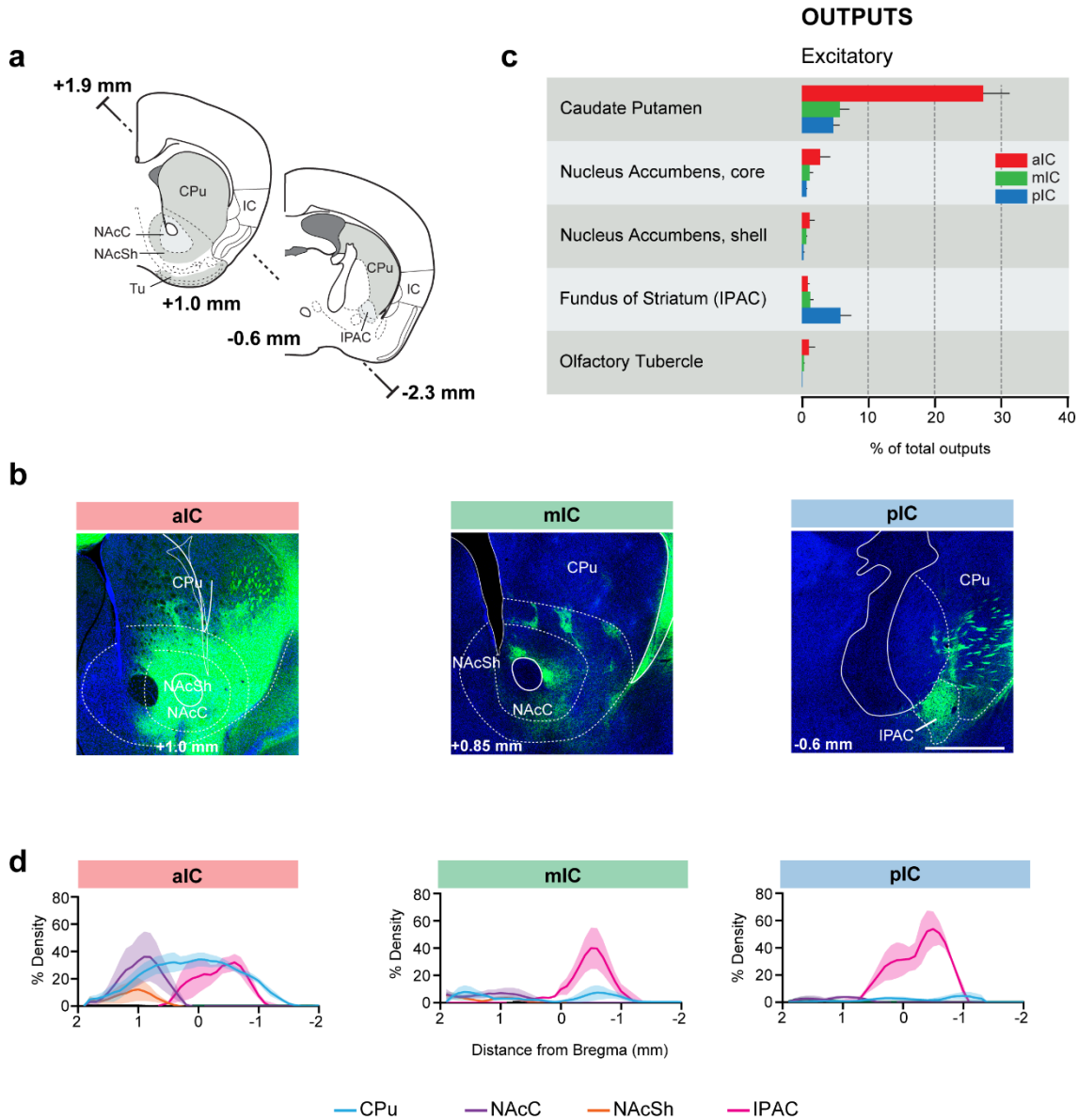


Figure 7. IC-striatum connectivity. a) Coronal sections depicting the striatum with its subregions. b) Representative images from excitatory outputs (eYFP-positive neurons). Note the strong innervation of CPu, NAcC and NAcSh by the aIC. Different Bregma levels are shown for each aIC, mIC and pIC, as indicated on the images. Scale bar = 500 μ m. c) Comparison of excitatory outputs from the three IC subdivisions to the striatum in percent of total output (aIC, red; mIC, green; pIC, blue). Values are given as percentage of total pixels. Data shown as average \pm SEM, $n = 3$ mice per condition. d) Plots depict the density of IC innervation along the anterior-posterior axis of the striatum. $n = 3$ mice per condition, data shown as average \pm SEM.

2.2 Functional Characterization of Posterior Insular Cortex

Having mapped the connectivity of the mouse insular cortex, I next wanted to investigate its implications in behavior. As has been suggested previously, the flow of information within the IC starts at the pIC and is progressively transmitted to the aIC^{40,77}. Craig suggested that sensory information about the body is first mapped in pIC and then subsequently remapped and integrated with emotional information in mIC and aIC^{77,170}. My rabies tracings in part support this view, as the pIC receives the majority of its inputs from sensory cortex (S1, S2, Pir, Au2), whereas the aIC connectivity is biasing motor related areas. Thus, I chose to functionally investigate the pIC - the potential primary entry point into the insula.

2.2.1 Optogenetic Stimulation of IC Induces a Mixture of Aversive Behaviors

To characterize the functional implications of the pIC on behavior, I used optogenetics to first broadly stimulate its activity. I infected excitatory pyramidal neurons of the pIC by bilaterally injecting 150 nl of AAV coding for ChR2 under the CamKII α promoter (AAV2/5-CamKII α -hChR2(H134R)-EYFP) and implanted optic fibers 500 μ m above the injection sites (**Figure 8a**). As my control condition, I used mice carrying bilateral optic fiber implants and that were injected with the same viral vector as for ChR2-mice but expressing only the fluorophore.

I titrated the stimulation parameters and found that 20 Hz stimulation often led to direct and mixed behavioral effects, which became more frequent upon consecutive stimulations (**Figure 8b,c**). A typical response pattern began with an interruption of ongoing locomotion, which quickly became freezing. Further stimulation elicited backward escape movements, movements of the jaw or salivation. This would build up with additional stimulations to eventually display very severe behavioral effects, such as jumping, vocalizing, lying on the side in a crouching position. In one case, an animal even died shortly after stimulation.

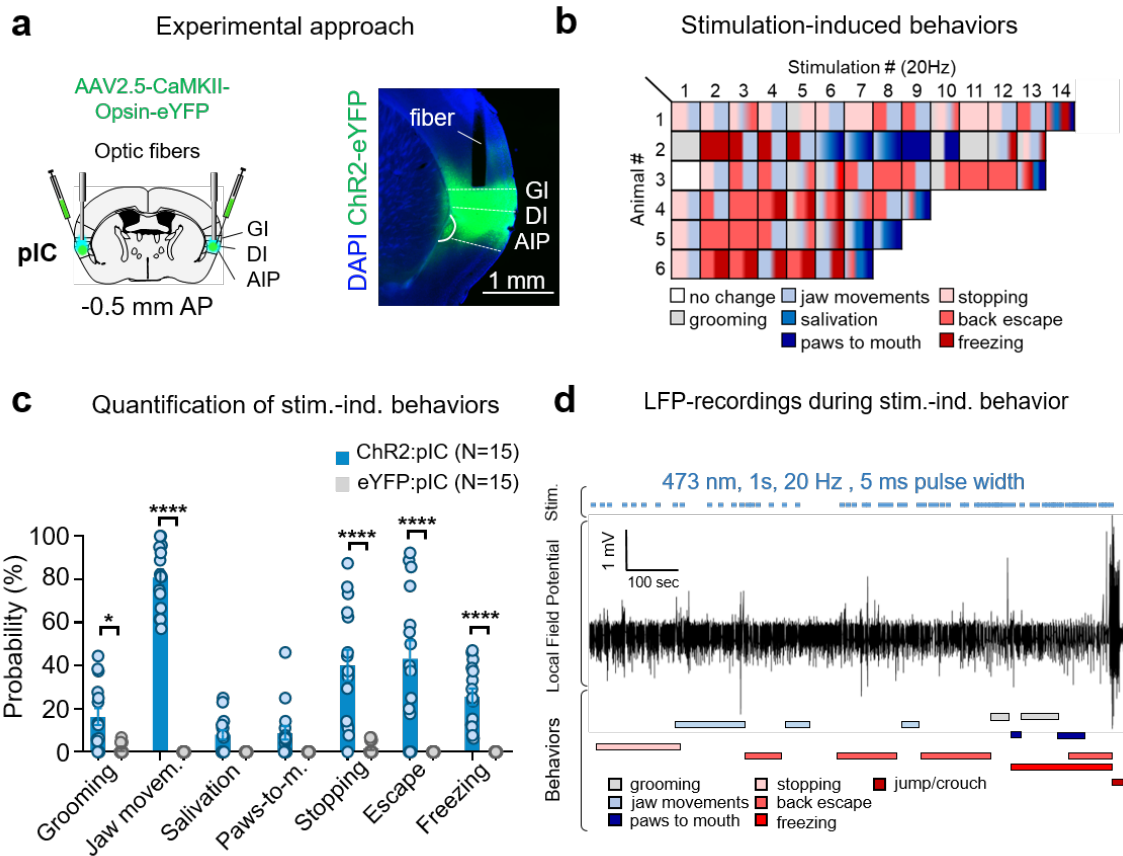


Figure 8. Bilateral optogenetic stimulation of pIC elicits various stimulation-induced behaviors. a) Optogenetic virus injections and optic fiber placements above the pIC. AP, anterior-posterior distance from Bregma. GI, granular insular cortex; DI, dysgranular insular cortex; AIP, posterior agranular insular cortex. b) Photostimulation triggered defensive behaviors in ChR2-expressing mice. Rows are reactions of representative individual mice to successive stimulations. Experiments were terminated after 5 minutes or when reaching severely aversive responses (animals 2-6). c) Quantification of light-evoked behavioral responses upon repeated 20 Hz stimulations ($n = 15$ mice / group derived from two independent experiments with similar results, two-way RM ANOVA, group (opsin) effect, $F(1, 28) = 857.6$, $p < 0.0001$; behavior effect, $F(6, 168) = 22.63$, $p < 0.0001$, group x behavior interaction, $F(6, 168) = 22.69$, $p < 0.0001$; Bonferroni post hoc analysis, grooming $*p = 0.0224$, jaw movements, stopping, escape and freezing $****p < 0.0001$, salivation ($p = 0.8581$) and paws-to-mouth ($p = 0.5988$) were not significantly altered). d) Example LFP trace from one ChR2-expressing animal during unilateral photostimulation-induced behaviors. Laser activations (473 nm, 1 s, 20 Hz, 5 ms pulse width, minimum of 4 s ISI) are indicated above the trace (blue) and observed behaviors are shown in color code below. Note the high amplitude LFP signal towards the end of the trace. Example LFP traces from different photostimulation-induced behaviors. Data from Panel d) was created and analyzed by Alexandra Klein. Panels a)-d) are adapted from my publication¹⁷¹ as permitted by the author reuse rights of Nature Springer.

Especially the last stages of this stereotyped sequence resembled seizure-like activity. Indeed, simultaneous local field potential (LFP) recordings during optogenetic stimulations, which were performed by my colleague Alexandra Klein, detected seizure-like LFP signatures during the jumping and crouching behaviors (**Figure 8d**).

To be able to characterize pIC function in behavioral tests whose readout is solely based on the analysis of locomotion, for instance the open field test (OF), the elevated-plus maze (EPM) or a real-time place aversion test (RTPA), I needed to titrate the optogenetic stimulation in such a way, that it did not directly affect locomotion. After screening a pilot cohort from a range of frequencies and inter-stimulus-intervals, I decided to further use a 1 s ON, 4 s OFF stimulation pattern with a stimulation frequency of 10 Hz with 5 ms pulse width (473 nm, 3-5 mW at the tip of the optic fiber). *Via* simultaneous LFP recordings, Alexandra Klein confirmed, that this protocol of light stimulation did not induce seizure-like LFPs (data not shown).

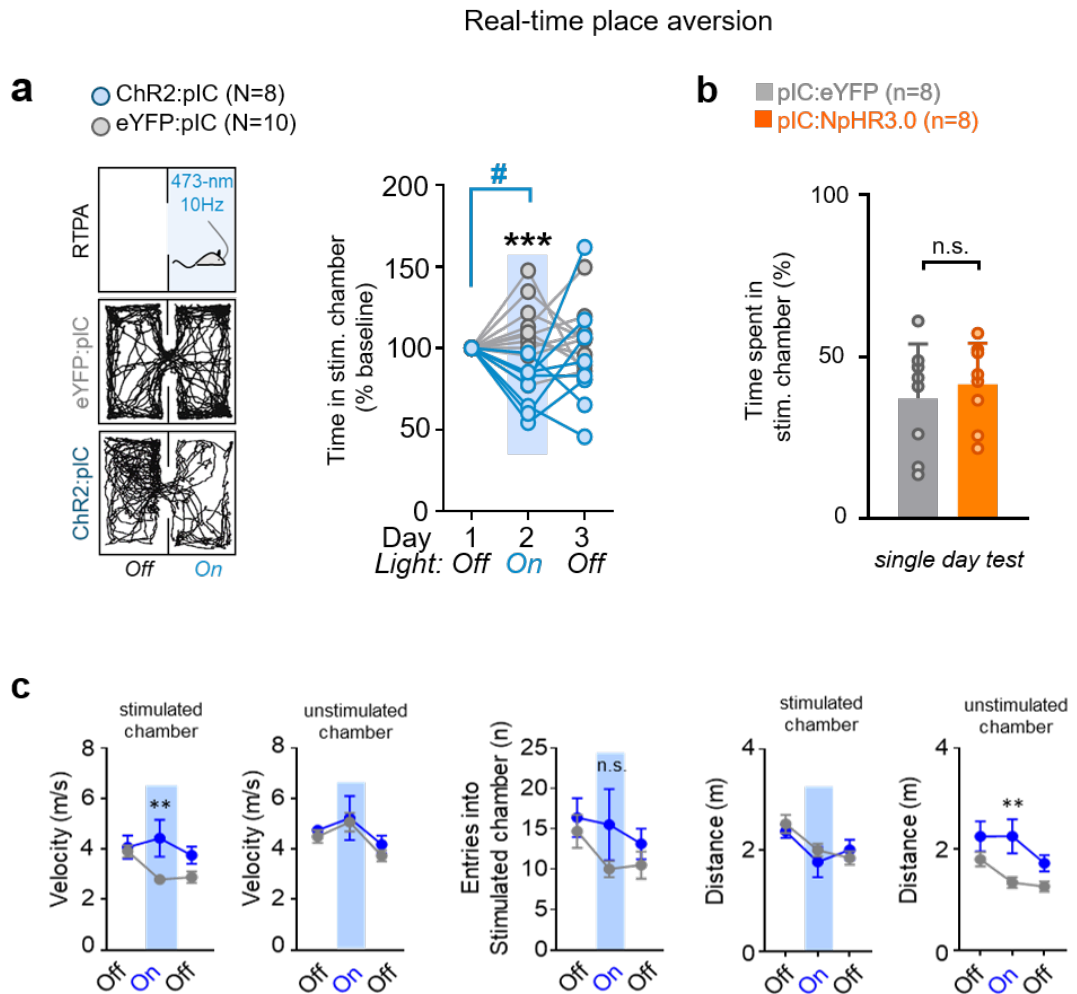


Figure 9: Real-time place preference test revealed that bilateral optogenetic pIC-activation is aversive. a) Left: schematic of the real-time place aversion assay (RTPA) and representative locomotor traces of eYFP and ChR2-expressing mice on the laser day. Right: Light activation of pIC neurons resulted in place aversion in ChR2 mice ($n = 8$ mice for ChR2 and $n = 10$ mice for eYFP, two-way RM ANOVA, group (opsin) $F(1,16) = 8.598$, $p = 0.0098$ and group \times time interaction $F(2,32) = 4.082$, $p = 0.0264$; Bonferroni post hoc analysis, $***p = 0.0008$ for ChR2 compared to eYFP; $\#p = 0.0463$ ChR2 laser off (day 1) versus laser on (day 2)). b) Inhibition of the pIC did not affect real-time place preference. Time spent in the laser chamber on the day of laser stimulation was not significantly different between eYFP- and NpHR- expressing animals ($n = 8$ mice / group, two-tailed unpaired t test, $t = 0.584$, $df = 14$, $p = 0.569$). c) Analysis of additional locomotion parameters of the RTPA assay ($n = 8$ ChR2, $n = 10$ eYFP mice). Left: stimulation of pIC increased velocity in the stimulated chamber (two-way RM ANOVA, $F(1, 16) = 5.225$, $p =$

0.0362, Bonferroni post-hoc, $**p=0.0099$ eYFP vs. Chr2 on laser 'on' day), but not in the unstimulated chamber (two-way RM ANOVA, $F(1, 16) = 0.8818$, $p = 0.3617$). Middle: Stimulation does not affect the number of entries into the stimulated chamber (two-way RM ANOVA, $F(1, 16) = 2.124$, $p = 0.1644$). Right: stimulation of pIC did not affect the distance travelled in the stimulated chamber (two-way RM ANOVA, $F(1, 16) = 0.2085$, $p = 0.6540$), but increased the distance travelled in the unstimulated chamber (two-way RM ANOVA, $F(1, 16) = 9.772$, $p = 0.0065$, Bonferroni post-hoc, $**p=0.0056$ eYFP vs. Chr2 on laser 'on' day). Data is plotted as mean + s.e.m. Panels a)-c) are adapted from my publication¹⁷¹ as permitted by the author reuse rights of Nature Springer.

To assess the valence of the stimulation-induced behaviors described above, I performed a real-time place aversion test. The advantage of this behavioral task is that the animals gain control over the optogenetic manipulation and by exhibiting a preference or avoidance they report if they perceive stimulation as positively or negatively valenced, respectively.

As has been previously reported¹⁴⁸, I confirmed that Chr2-expressing mice avoided the laser-coupled chamber, as compared to eYFP-expressing control animals (**Figure 9a**). In contrast to optogenetic stimulation, bilateral inhibition of the pIC in NpHR3.0-expressing mice had no effect on their place preference (**Figure 9b**). The avoidance of the chamber was not due to the animals moving less or slower on the stimulated side. The increased velocity in the stimulated side rather indicates that animals actively escaped the stimulated chamber (**Figure 9c**).

In all cohorts of bilateral pIC stimulation, I observed that the breathing frequency was increased during, but also shortly after stimulation. As such an increased breathing rate could either be an immediate consequence of pIC activity or rather an emerging emotional reaction caused by aversive or arousing perceptions, I repeated pIC photostimulation in anesthetized mice and measured their heart- and breathing rates. For this, I used the MouseOx Plus pulse oximeter with a neck-clip under 1,5 % isoflurane anesthesia. Stimulation of the pIC at 5, 10 and 20 Hz increased breathing rate, whereas inhibition of pIC had no effect (**Figure 10a,c**). I could not find any alterations of the heart rate during pIC activation or inhibition (**Figure 10b,d**), which have been reported in electrical stimulation studies of IC in rats and humans^{47,48}.

To summarize, these findings demonstrate that peaks in pIC activity can elicit aversive reactions and avoidance, as well as autonomic changes.

Physiological measurements

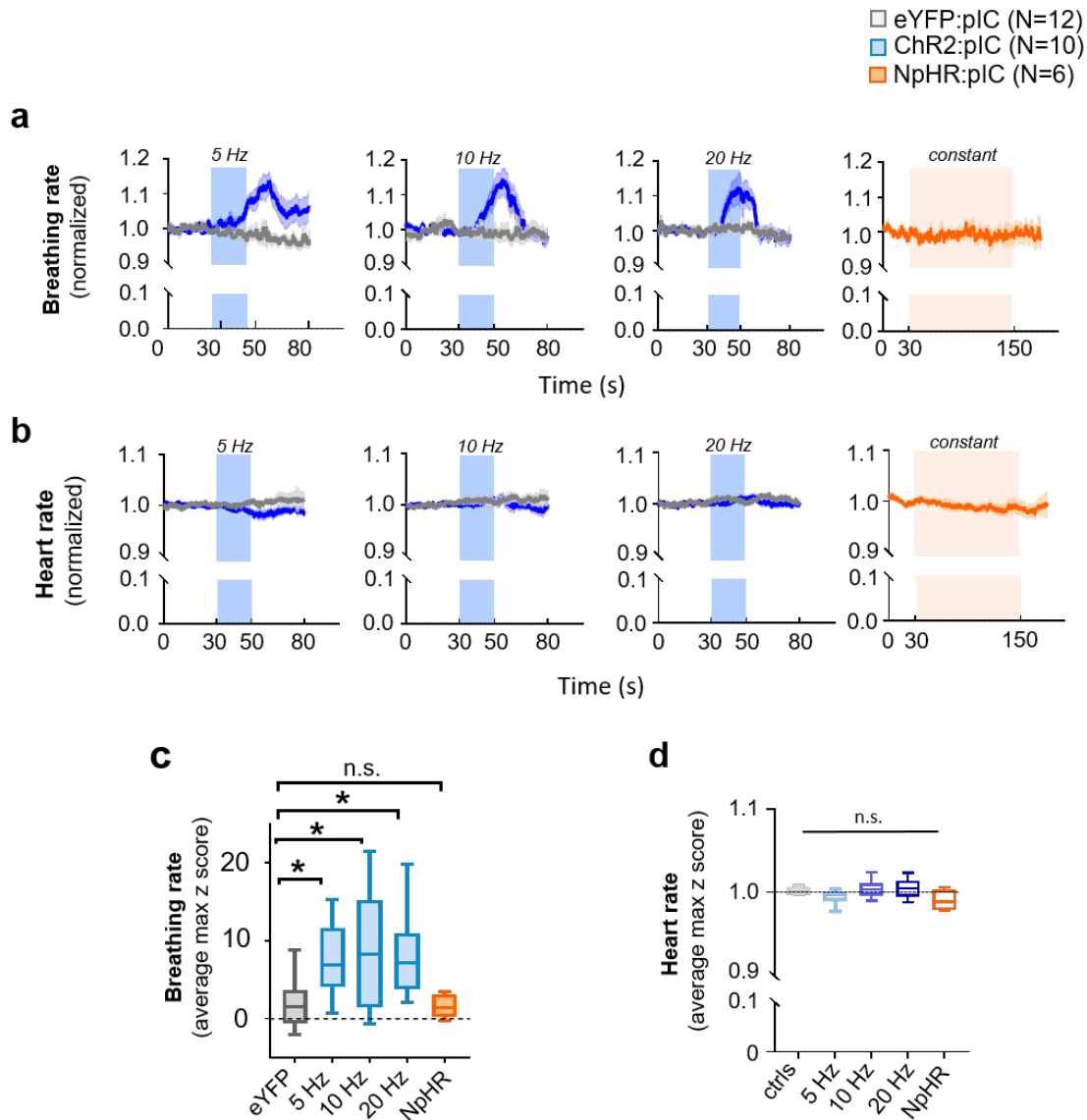


Figure 10. Bilateral optogenetic manipulation of pIC increased breathing- but not heart rate in anaesthetized mice. a) Timeline of respiratory responses upon 5, 10, or 20 Hz stimulations or NpHR mediated inhibition of anesthetized mice ($n = 6$ Chr2, $n = 4$ eYFP, $n = 4$ NpHR mice). Line graphs are mean with shaded areas s.e.m. b) Heart rate measurements upon Chr2-, or NpHR-mediated activity manipulations. Data are normalized to a 20-second baseline period for each individual. Line graphs are mean with shaded areas s.e.m. c) Optogenetic activation increased respiratory rates at all frequencies, while inhibition had no effect (eYFP, $n = 12$ mice (6 mice exposed to blue and 6 mice exposed to yellow light); Chr2 $n = 10$ mice; NpHR $n = 6$ mice; one-way ANOVA, $F(4, 43) = 4.643$, $p = 0.0033$, Bonferroni post hoc analysis, $*p = 0.0412$ for eYFP versus 5 Hz; $*p = 0.0116$ for eYFP versus 10 Hz; $*p = 0.0234$ for eYFP versus 20 Hz; $p > 0.999$ for eYFP versus NpHR. d) Quantitative assessment of the same data as in panel b. No significant difference between groups was detected (one-way ANOVA $F(4, 33) = 2.872$, $p = 0.0381$). Box-whisker plots display median, 25th to 75th percentiles, and min to max values. Panels a)-d) are adapted from my publication¹⁷¹ as permitted by the author reuse rights of Nature Springer.

2.2.2 Bulk Calcium Imaging of IC Activity during Anxiety-Related Behavioral Tests

The findings I described above suggested that increased pIC activity transmits a negative valence signal, which can elicit defensive reactions at 20 Hz. To investigate which naturally occurring situations might evoke pIC activity, aside from the already described response to bitter taste¹⁴⁸, my colleague Ritu Roy Chowdhury measured the bulk activity of pIC neurons with fiber photometry while the mice explored the elevated plus maze (EPM) or elevated zero maze (EZM) (**Figure 11a**). I assisted in the analysis of the calcium traces and we first asked how the bulk activity of the pIC changed with the occupancy of the open or closed arms of the two mazes. For all measured animals, we detected high levels of pIC activity when the mice were in the closed arms of the mazes. In contrast, on the open arms the bulk pIC activity was consistently low (**Figure 11b,c**). These findings suggested that pIC activity is high during periods of high anxiety, i.e. while the animals avoid exploration and wait in the - presumably safer - closed arms. Alternatively, an increased pIC activity could also signify the safety of the closed compartment, as IC has been implicated in safety learning in rats^{86,172}. To clarify this, we correlated the time spent on the open arms, i.e. a measure of their anxiety, with the averaged bulk fluorescence during their closed arm stays (**Figure 11c**). Indeed, the anxiety level was positively correlated with their closed arm pIC activity. In other words, we found that the higher the anxiety level of an animal was the higher was its bulk neuronal activity of pIC. This was complemented by the finding that the anxiety level of the animals correlated with their pIC activity during the open arm visits. In other words, the higher the anxiety, the lower the pIC open arm activity. When I correlated the pIC activity data with the animals' approach or retreat behavior to and from the open arms (**Figure 12a**, see Methods), I found that during retreats from the open arms pIC activity increased, whereas approaches were accompanied by decreases in pIC activity (**Figure 12b**). Overall, I found a significant positive correlation for approach- and retreat behavior with calcium activity (two-sided one sample t test, $t = 4.111$, $df = 10$, $**p = 0.0021$, **Figure 12c**). Further, I analyzed the dynamic changes of the calcium signal during approach or retreat episodes and consistently found that pIC activity increased during retreats and decreased during approaches (**Figure 12d**). Correlating pIC activity with the velocity of the animals suggests that pIC activity is not driven by the speed of locomotion, as Ritu could not find a significant correlation (two-tailed one sample t test revealed no significant difference from zero, $t = 0.8450$, $df = 10$, $p = 0.4179$) (**Figure 12e**).

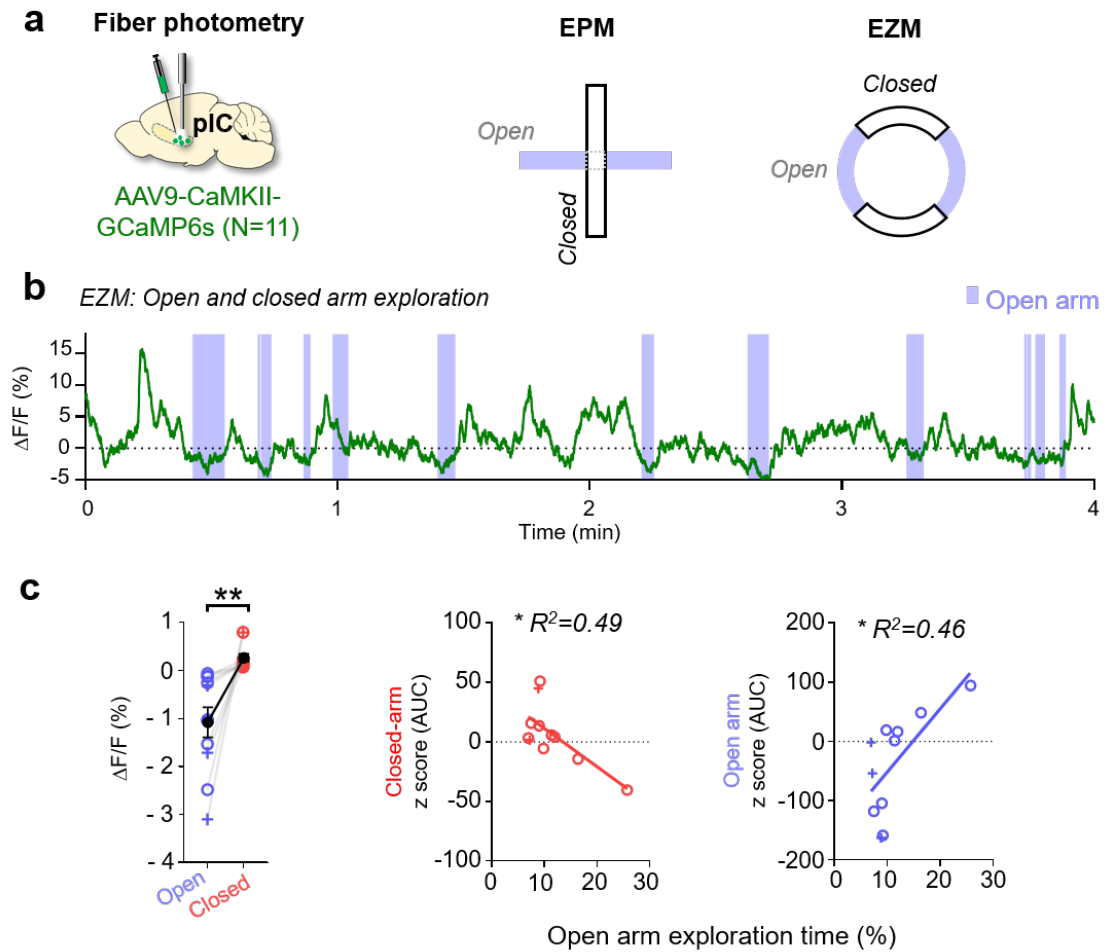


Figure 11. Bulk calcium imaging of pIC during anxiety-related tests revealed increased activity in the closed arms whereas open arm visits showed reduced activity. a) Optic fiber placement and virus used for fiber photometry. b) Example GCaMP6s trace from pIC excitatory neurons during 4 minutes of elevated zero maze (EZM) exploration. Periods in the open arms are shaded in blue. Note, that the pIC activity decreases in the open arms. c) Mean pIC activity is significantly higher in all animals in the closed versus open arms in two similar paradigms, the EZM and elevated plus maze (EPM), ($n = 11$, two-tailed paired t test, $t = 3.510$, $df = 10$, $**p = 0.0056$, data combined from 3 EPM mice (pluses) and 8 EZM mice (circles). The mean \pm s.e.m. is shown in black. Middle: The mean closed arm activity in the pIC in both tests is correlated to the anxiety of the individuals (open arm time). Linear regression, $F(1,9) = 8.574$, $*p = 0.0168$, $R^2 = 0.4879$, Right: The mean open arm activity is inversely correlated to anxiety. Linear regression, $F(1,9) = 7.620$, $*p = 0.0221$, $R^2 = 0.4585$. Total $n = 11$ mice (3 EPM shown as pluses, 8 EZM shown as circles). Panels a)-c) are adapted from my publication¹⁷¹ as permitted by the author reuse rights of Nature Springer.

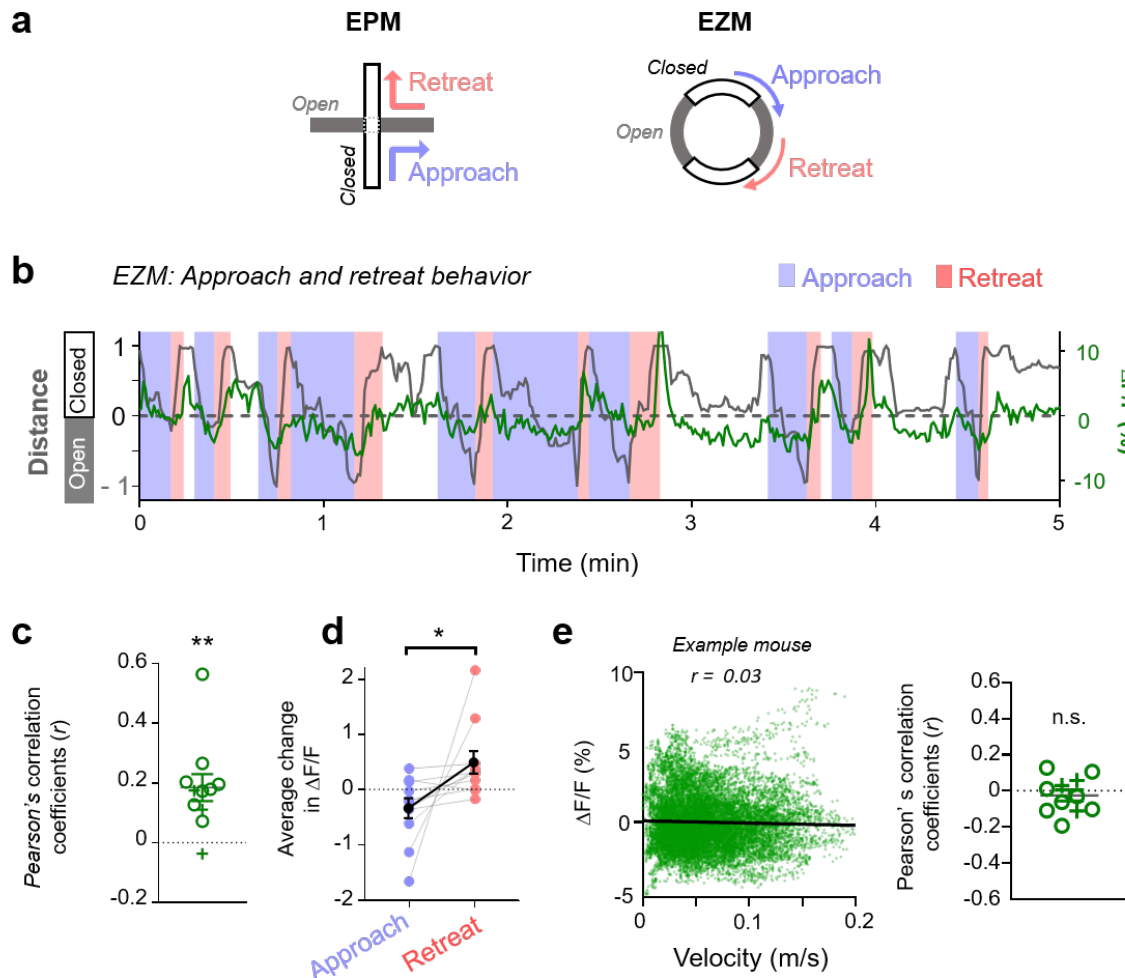


Figure 12. pIC activity is correlated with approaches and retreats to and from the open arm of anxiety-related tests. a) Schematic illustration of approach (movement towards open arms of the mazes) and retreat (movement towards the closed arms of the mazes) behavior. b) Exemplary overlay of pIC activity and distance travelled within the EZM reflecting approach and retreat behavior. c) Correlations between fluorescence and approach/retreat distances were significant for all animals (not shown) and correlation coefficients (r) overall significantly different from zero ($n = 11$ mice including 3 EPM (pluses) and 8 EZM (circles) as above, two-sided one sample t test, $t = 4.111$, $df = 10$, $**p = 0.0021$). Error bars indicate s.e.m. d), For all animals, the average change of fluorescence was negative during approaches and positive during retreats. This resulted in an overall significant difference in the average fluorescent change between approaches and retreats ($n = 11$ mice, two-tailed paired t test, $t = 2.255$, $df = 10$, $*p = 0.0478$). Values from one mouse are connected with a grey line. The mean and s.e.m. are shown in black. e) Left: Pearson's correlations of pIC fluorescence as a function of velocity in one example animal. Velocity is very weakly correlated to pIC activity. Right: There is no correlation of pIC activity and velocity across animals ($n = 11$ mice, circles tested in EZM, pluses tested in EPM, two-tailed one sample t test revealed no significant difference from zero, $t = 0.8450$, $df = 10$, $p = 0.4179$). Panels a)-e) are adapted from my publication¹⁷¹ as permitted by the author reuse rights of Nature Springer.

Taken together, these results suggest that increased pIC activity may inhibit exploration of the open arms, while low pIC activity permits exploration. Furthermore, the data suggests that pIC activity is a proxy for the anxiety-levels of the animals.

2.2.3 Optogenetic Manipulation of pIC during Anxiety-related Tests Enables Bi-directional Modulation of Anxiety-like Behavior

2.2.3.1 Real-time Optogenetic Manipulation on the EPM or EZM

To test the role of the pIC in anxiety-like behavior, I designed an experiment that was guided by the fiber photometry results described above. I performed the test with the same animals used in **Chapter 2.2.1**, which bilaterally expressed opsins in the pIC under the CamKII α promoter (**Figure 13a**). As we previously found that pIC activity was high in the closed arms of the EPM and EZM, I aimed to only inactivate the pIC while the animals were in the closed arms, but not when they were exploring the open arms (**Figure 13b**).

Real-time silencing of the pIC of NpHR-mice increased the time spent on open arms of the EPM in comparison to controls. As it did not affect the total distance travelled, it suggests that inhibition had anxiolytic effects (**Figure 13c**).

Oppositely, I only stimulated the pIC of ChR2-expressing mice when the animals were on the open arms, where pIC activity was shown to be low (**Figure 13b**). If pIC would rather signal safety than anxiety, activating the insula should encourage the animals to explore the open arms longer.

To my surprise, I did not find a significant difference in time spent on open arms between eYFP- and ChR2-expressing mice in the EPM (**Figure 13c**). This might have been due to the anxiogenic environment in which the EPM was performed. I therefore subjected the same mice to an equivalent anxiety test, the EZM, but this time under low-anxiety settings (see Methods). ChR2-mediated pIC stimulation in the open arms reduced the time spent on as well as the entries into the open arms (**Figure 13d**) suggesting an anxiogenic effect. Interestingly, pIC inhibition did not significantly increase open-arm time in this low-anxiety environment.

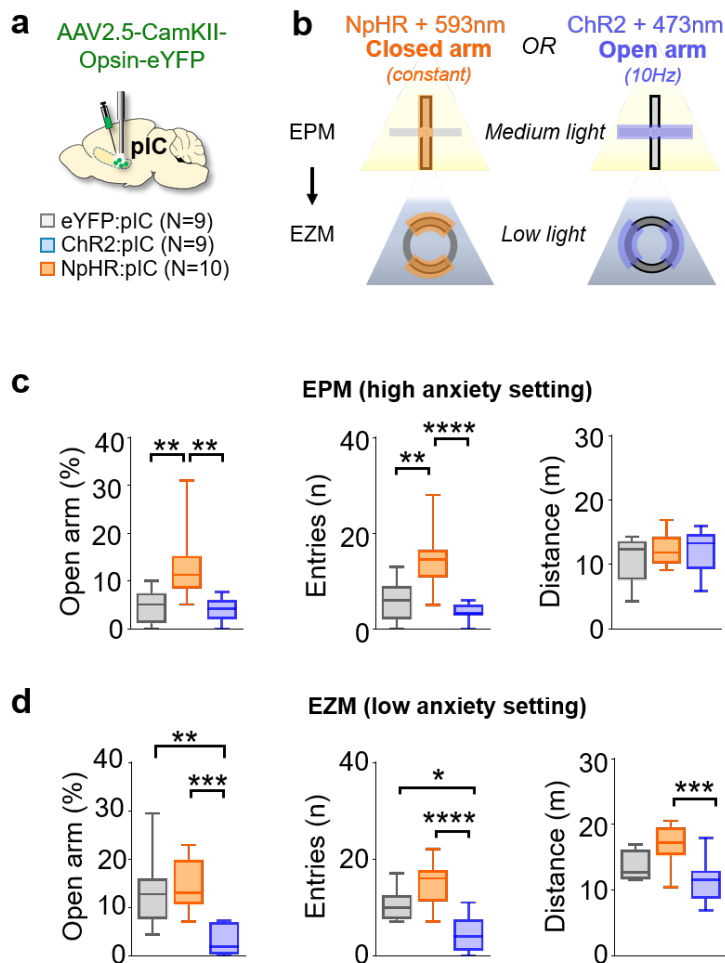


Figure 13. Real-time optogenetic manipulation exerts bi-directional influence on anxiety-like behavior. a) Optogenetic experimental strategy. b) Real-time inhibition (left) and stimulation (right) arrangement in the EPM under high anxiety settings (top) and low anxiety settings in the EZM (bottom); see Methods. c) Data derived from $n = 9$ eYFP, $n = 9$ ChR2 and $n = 10$ NpHR - expressing mice. pIC silencing increased the time spent (one-way ANOVA, $F(2, 25) = 9.267$, $p = 0.0010$, Bonferroni post-hoc analysis, $**p = 0.0049$ eYFP versus NpHR, $**p = 0.0022$ NpHR versus ChR2, $p > 0.999$ eYFP versus ChR2) and the number of entries into the open arms of the EPM (one-way ANOVA, $F(2, 25) = 14.99$, $p < 0.0001$, Bonferroni post-hoc analysis, $**p = 0.0014$ eYFP versus NpHR, $****p < 0.0001$ NpHR versus ChR2, $p = 0.7971$ eYFP versus ChR2), but left the locomotion distance unaltered (one-way ANOVA, $F(2, 25) = 0.6660$, $p = 0.5227$). d) In the same animals as in b), pIC stimulation decreased the time (one-way ANOVA, $F(2, 25) = 11.98$, $p = 0.0002$, Bonferroni post-hoc analysis, $**p = 0.0019$ eYFP versus ChR2, $***p = 0.0004$ NpHR versus ChR2, $p > 0.9999$ eYFP versus NpHR), the number of entries into the open arms of the EZM (one-way ANOVA, $F(2, 25) = 16.29$, $p < 0.0001$, Bonferroni post-hoc analysis, $*p = 0.0143$ eYFP versus ChR2, $****p < 0.0001$ NpHR versus ChR2, $p = 0.0549$ eYFP versus NpHR), and the overall locomotion distance (one-way ANOVA, $F(2, 25) = 8.863$, $p = 0.0012$, Bonferroni post hoc analysis, $***p = 0.0009$ NpHR versus ChR2, eYFP versus NpHR, $p = 0.0694$, $p = 0.2954$ eYFP versus ChR2). Box-whisker plots display median, 25th to 75th percentiles, and min to max values. Panels a)-d) are adapted from my publication¹⁷¹ as permitted by the author reuse rights of Nature Springer.

2.2.3.2 Complementary Anxiety-related Behavioral Tests

Of note is that in previous cohorts, performed by me and Arthur Matthys, we optogenetically inhibited pIC in alternating 2 min ON and OFF periods, as has been frequently used in literature^{173,174} (**Figure 14a**). This was not sufficient to significantly increase the time spent on the open arms (**Figure 14b**). Nevertheless, we found a strong trend towards anxiolysis as indicated by more time spent on the open arms, as well as more entries while travelling the same distance. These results combined with the real-time pIC inhibition described above suggest that pIC inhibition is anxiolytic only when sustained over longer periods and only when the insula would be naturally engaged. In support of this finding are similar observations that I obtained from silencing pIC with inhibitory DREADDs (hM4Di) in an open-field test (**Figure 14c-d**).

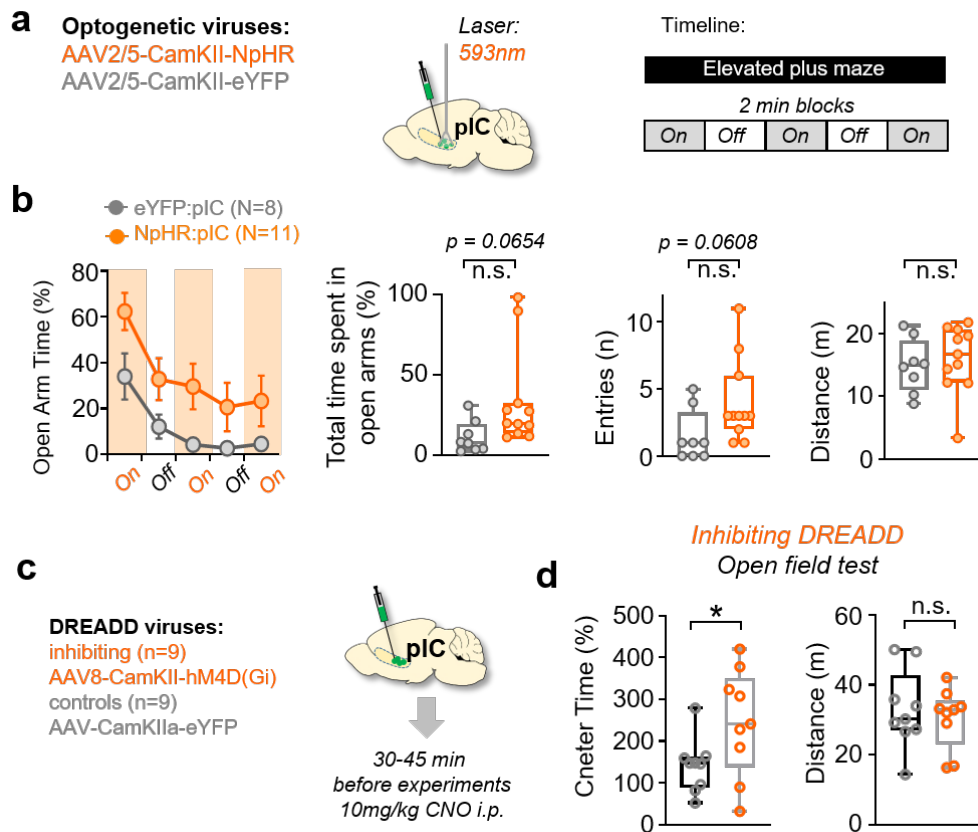


Figure 14. Complementary anxiety-related experiments that support a role of the pIC in anxiety states. a) Experimental strategy and timeline for optogenetic pIC activity manipulations using a fixed regimen of alternating 2-min laser ‘on’ and ‘off’ epochs. b) Data from $n = 8$ eYFP- and $n = 11$ NpHR-expressing mice. Left: Inhibition of pIC activity did not significantly alter the time spent in the open arms, only a trend towards anxiolysis was observed (two-way RM ANOVA, group (opsin) effect, $F(1, 17) = 3.881$, $p = 0.0654$; time effect, $F(1.585, 26.95) = 24.73$, $p < 0.0001$, group x time interaction $F(4, 68) = 0.5624$, $p = 0.6907$). Right: Also the overall time spent in the open arms showed a trend to more exploration upon pIC inhibition (two-tailed unpaired t test: $t = 1.970$, $df = 17$, $p = 0.0654$). Neither the entries into the open arms (two-tailed unpaired t test, $t = 2.008$, $df = 17$, $p = 0.0608$), nor the total distances travelled within the maze (two-tailed unpaired t test, $t = 0.4976$, $df = 17$, $p = 0.6251$) differed between the groups. c) Viruses and strategy used to manipulate pIC activity using DREADDs. d) Constant silencing of the pIC

throughout the exploration of the circular open field using DREADD-hM4D resulted in anxiolytic effects ($n = 9$ mice / group) as revealed by increased time spent in the center (two-tailed unpaired t test, $t = 2.165$, $df = 16$, $*p = 0.0459$), but no difference in the total distance travelled (two-tailed unpaired t test, $t = 0.5524$, $df = 16$, $p = 0.5883$). Panels a)-d) are adapted from my publication¹⁷¹ as permitted by the author reuse rights of Nature Springer.

Taken together, these findings show that the pIC can influence anxiety-related behaviors bi-directionally. Further, our data suggest that the pIC might play a role in creating, monitoring and modulating anxiety states.

2.2.3.3 pIC mediates Persistent Anxiety

To investigate if the pIC is influencing the emergence of anxiety states, I performed manipulations of the pIC and afterwards assessed the anxiety-level of the mouse on an EPM. First, I stimulated the pIC of ChR2- or eYFP-expressing mice ten times in an open field for 1 s at 20 Hz (473 nm, 3-5 mW, 5 ms pulse width). Immediately afterwards, I detached the animals from the optic fiber cables and tested them on an EPM (**Figure 15a**). Strikingly, after stimulation, ChR2-expressing mice strongly reduced the time spent on open arms with less entries compared to eYFP-expressing controls (**Figure 15b-d**). This effect could be repeated by Alexandra Klein in an independent cohort. The sustained anxiety was particularly pronounced during the first 2 min of the test (**Figure 15c,d**). Thus, transient pIC stimulation induced a longer lasting anxiety-like state.

Then, I wondered, whether pIC activity is necessary for the emergence of anxiety-like states. To test this, I subjected mice to five unsignaled foot shocks in a standard conditioning chamber (**Figure 15a**), as it has been shown, that shocks induce a long-lasting anxiety-like behavior¹⁷⁵. During the 20 min period when mice received shocks, I constantly inhibited the pIC with orange laser light (594 nm, 12 mW). My colleague Alexandra Klein has shown in separate animals, that 20 min long inhibition is able to reliably suppress neuronal activity in the pIC (see **Appendix 4**). When I then tested the mice on the EPM, eYFP-expressing control mice that have been shocked significantly decreased their open-arm exploration when compared to non-shocked controls (**Figure 15b-d**). Their explorative behavior resembled that of the ChR2-stimulated mice. In contrast, NpHR-expressing mice displayed a significant rescue of this behavioral phenotype resembling non-shocked eYFP-controls.

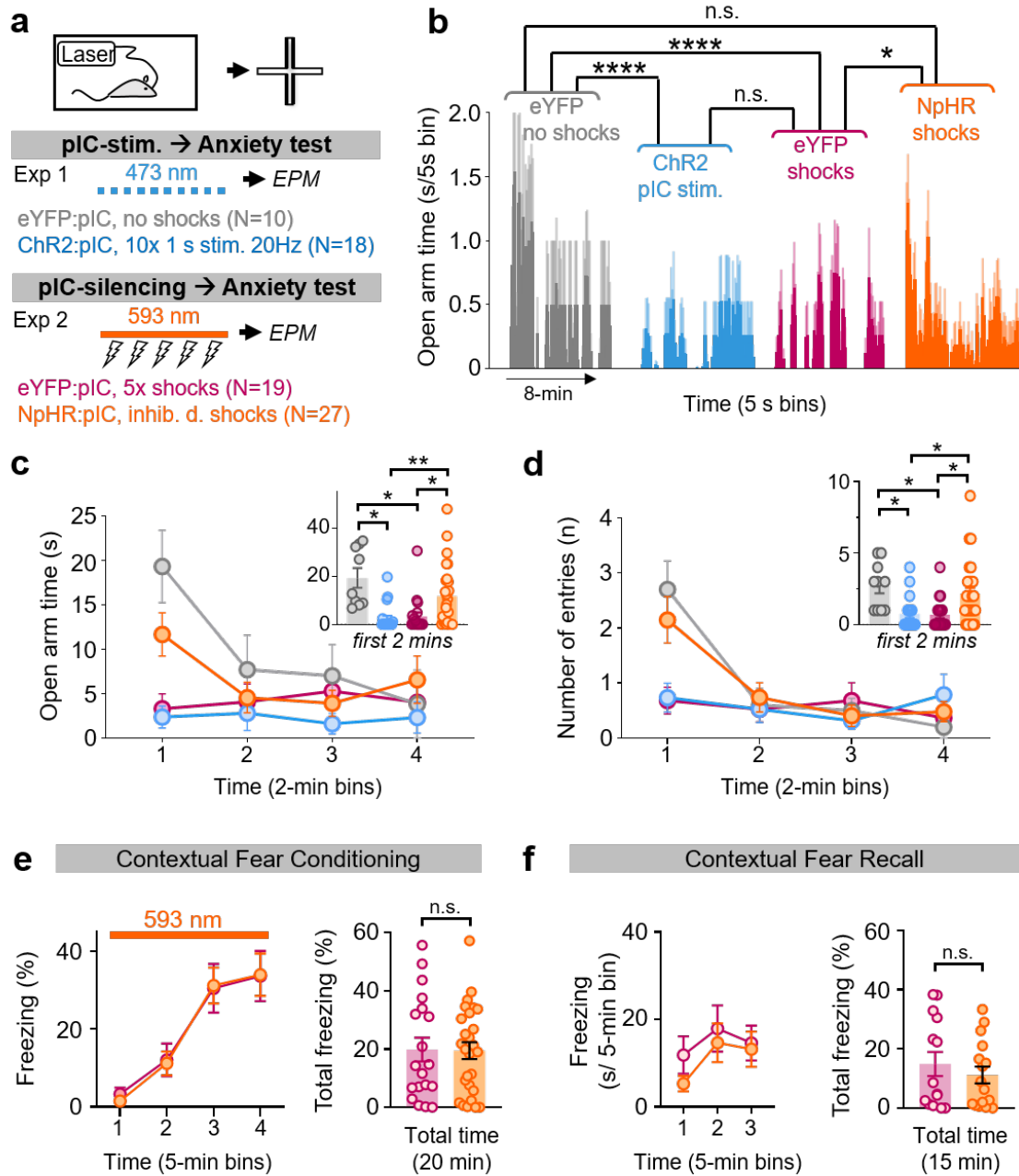


Figure 15. The pIC mediates persistent anxiety. a) Illustration of the experimental protocol. b)-d), $n = 10$ eYFP mice without shocks, $n = 18$ ChR2 mice, $n = 19$ eYFP mice with shocks, $n = 27$ NpHR mice. b) Transient photostimulation of the pIC (blue) decreased open arm time during subsequent testing on an EPM compared to controls (grey). The experience of footshocks resulted in a similar reduction of open-arm exploration in eYFP-expressing animals (magenta) as pIC stimulation (blue). This effect was attenuated by pIC inhibition during the shocks (orange). One-way ANOVA, $F(3,380) = 17.36$, $p < 0.0001$, Bonferroni post hoc analysis, eYFP with shocks vs. NpHR $*p = 0.0399$; eYFP with vs. without shocks $****p < 0.0001$; eYFP with shocks vs. ChR2 $p = 0.3182$; NpHR vs eYFP no shocks $p = 0.2705$; NpHR vs ChR2 $****p < 0.0001$; eYFP no shocks vs. ChR2 $****p < 0.0001$. c) The same data as in b) analyzed in 2-min bins revealed that pIC silenced and no-shock controls explore the open arms significantly more during the first two minutes than shocked or pIC-stimulated animals. Two-way RM ANOVA, group(opsin) effect, $F(3, 70) = 4.340$, $p = 0.0073$, time effect, $F(2.678, 187.5) = 4.502$, $p = 0.0062$, opsin x time interaction, $F(9, 210) = 2.139$, $P = 0.0277$; Bonferroni post-hoc analysis revealed significant differences for the following comparisons during the first two minutes: eYFP with shocks vs NpHR $*p = 0.0415$; eYFP with shocks vs. no shocks $*p = 0.0244$; NpHR vs. ChR2 $**p = 0.0093$;

eYFP no shocks vs ChR2 * $p = 0.0173$. Comparisons between eYFP with shocks and ChR2 ($p > 0.9999$) and NpHR vs. eYFP no shocks ($p = 0.7770$) were not significant. The inset shows individual values for time spent in the open arms during the first two minutes and the significant differences as revealed by the Bonferroni test. d) Analysis of open arm entries over time in 2-min bins. Two-way RM ANOVA, group effect, $F(3, 71) = 1.647$, $p = 0.1863$, time effect, $F(2.451, 174) = 13.9$, $p < 0.0001$, opsin x time interaction, $F(9, 213) = 3.599$, $p = 0.0003$; Bonferroni post-hoc analysis revealed significant differences in the first two minutes for the following comparisons: eYFP with shocks vs NpHR * $p = 0.0262$; eYFP with shocks vs. no shocks * $p = 0.0221$; NpHR vs. ChR2 * $p = 0.0407$; eYFP no shocks vs ChR2 * $p = 0.0273$. eYFP with shocks vs. ChR2 and NpHR vs. eYFP no shocks were not significantly different (both $p > 0.9999$). The inset shows individual values for open arm entries during the first two minutes and the significant differences as determined by the Bonferroni test. e)-f), $n = 16$ NpHR and $n = 15$ eYFP mice. e) Constant pIC inhibition did not affect freezing during the 20-minute footshock period. Left: Analysis in 5-minute bins revealed no difference between groups. Two-way RM ANOVA, group effect, $F(1, 44) = 0.007057$, $p = 0.9334$. Right: Total freezing of all individuals that received footshocks. Two-tailed unpaired t test, $t = 0.4193$, $df = 13$, $p = 0.6818$. f) Left: Analysis in 5-minute bins revealed no difference between groups. Two-way RM ANOVA, group (opsin) effect, $F(1, 28) = 0.6022$, $p = 0.4442$. Right: Total freezing of all individuals that received footshocks. Two-tailed unpaired t test, $t = 0.7586$, $df = 28$, $p = 0.4544$. Bar and line graphs indicate mean \pm s.e.m. Box-whisker plots display median, 25th to 75th percentiles, and min to max values. Panels a)-f) are adapted from my publication¹⁷¹ as permitted by the author reuse rights of Nature Springer.

To rule out that the effects of pIC inhibition were due to a reduced acute fear expressed during the foot shocks, I analyzed freezing behavior, expressed during the foot shocks and again several days later in a conditioning chamber during contextual fear recall. I found that pIC inhibition did not affect acute freezing during the foot shocks (**Figure 15e**). Also, when performing a recall of contextual conditioning (without optogenetic manipulation), the NpHR mice spent a similar time freezing as control mice (**Figure 15f**). To exclude, that pIC inhibition modifies the pain perception of the shock, Tom Gaitanos helped me to show, that pIC inhibition did not affect pain thresholds in a ramping hot-plate test (see **Appendix 5**)

In sum, these results imply that inhibition of the pIC does not interfere with acute reactions to painful stimuli and that it did not prevent acute freezing behavior. Instead, the data point towards an important role of the pIC in the generation of longer lasting anxiety states.

2.2.4 pIC→CeA and pIC→NAcc projector neurons form non-overlapping populations

My anatomy data revealed several interesting projection pathways, which may underlie the heterogeneous behaviors elicited by global pIC stimulation. As described in **Chapter 2.1.4** and **2.1.5**, the pIC projects to both the CeA and NAcc, two brain areas heavily implicated in motivated behaviors^{176,177}.

Recent studies have started to functionally explore the pIC-to-CeA projection (pIC→CeA), which mediated behavioral inhibition in a go-nogo task, and caused cessation of licking^{9,178}. Therefore, I chose to further characterize the functional implications on behavior of pIC→CeA.

As the IC has been shown to also play a role in addiction, feeding and decision-making, I was very keen to characterize the pIC-to-NAcc pathway (pIC→NAcc). The nucleus accumbens core has been extensively characterized in reward-related or appetitive behaviors, with a few studies indicating also mediation of aversive reactions^{168,179}.

However, before performing projection-specific optogenetic experiments with both pathways, I first aimed to better characterize the organization of the circuit from the pIC to the CeA and NAcc. In particular, I analyzed how the CeA- and the NAcc-projectors of the pIC distributed within the pIC. Therefore, I used the well characterized retrograde tracer Cholera toxin subunit B (CTB) conjugated with Alexa488 and Alexa555 dyes. I injected CTB-488 into the NAcc and CTB555 into the CeA of the same animals and performed histology (**Figure 16a-c**). I quantified CeA- and NAcc-projecting neurons across the entire IC, as depicted in **Figure 16f**. CeA-projectors were more abundant in the mIC and pIC, which is complementary to my anterograde AAV tracings from mIC and pIC (**Figure 6**). In contrast, NAcc-projectors were more numerous in the aIC, which is again consistent with my AAV tracings from aIC (**Figure 7**). Within the pIC, most labelled neurons projected to the CeA (66.3%) and around a third to NAcc (27.7%) (**Figure 16d**). The relative distribution within the layers of pIC showed, that most CTB⁺ neurons were found in the AIP, followed by DI and GI, however, there was no difference between CeA or NAcc projectors (**Figure 16e**). Interestingly, the two projecting populations were mostly non-overlapping, with <6% of pIC neurons projecting to both CeA and NAcc (**Figure 16d**). These results encouraged me to continue with the characterization of the CeA and NAcc pathway with projection-specific optogenetics. In order to guide my injection and implantation coordinates, I revisited the innervation density profiles from the pIC to both the CeA and the NAcc. At the rostro-caudal level where pIC innervation of the target regions was densest, I would implant optic fibers (**Figure 16g-j**), while the optogenetic viral constructs would be injected into the pIC.

Segregation of pIC projection neurons

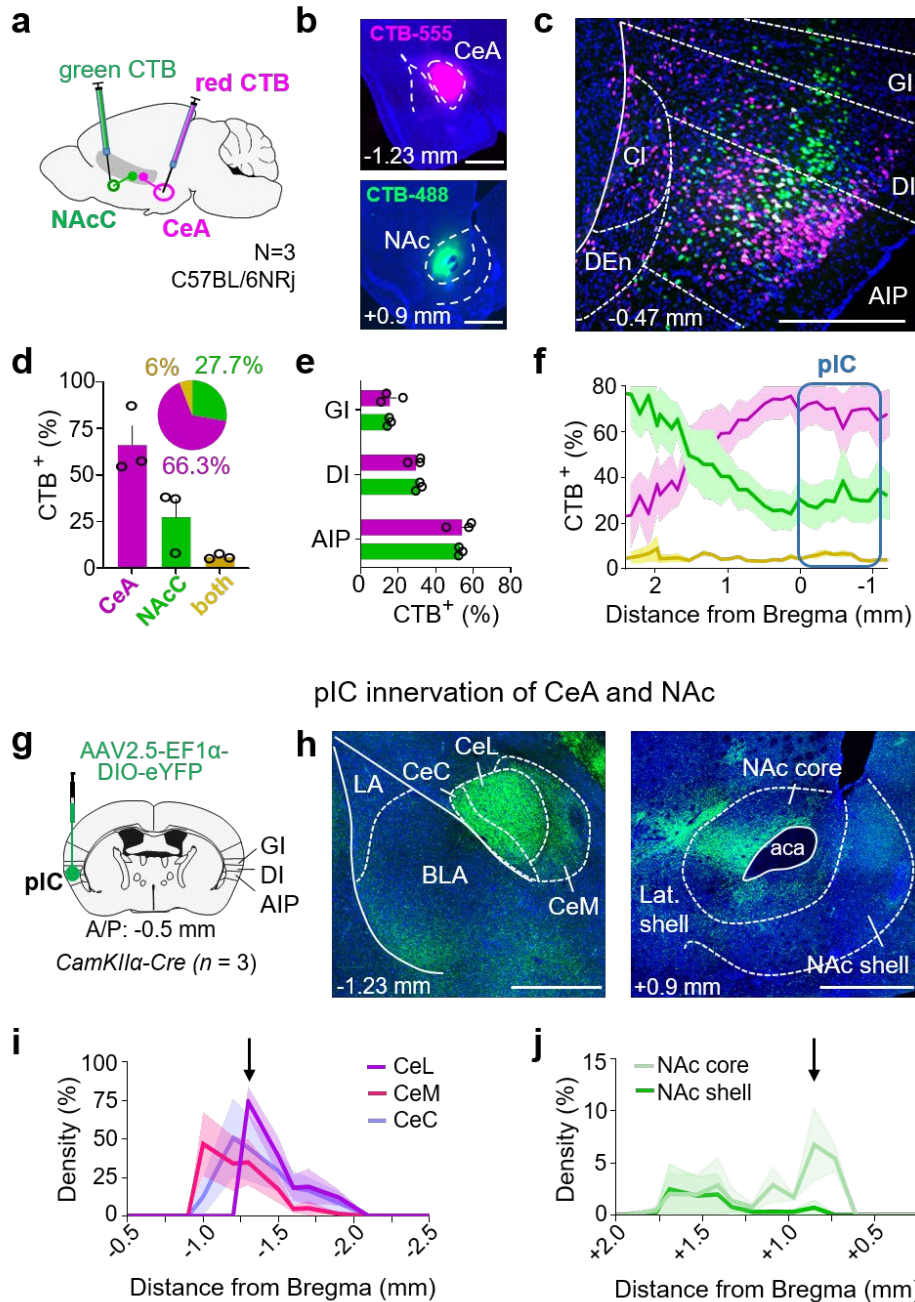


Figure 16. Largely non-overlapping pIC neuronal subpopulations project to the CeA and NAc. a) CTB retrograde labeling of pIC projections to the CeA (CTB-555) and NAc (CTB-488). b) Representative images of CTB injection sites in the CeA (top) and NAc (bottom). Similar results were replicated in three mice. c) Representative image of retrogradely labeled pIC neurons projecting to CeA (magenta), NAc (green), or both (yellow). d-f) data from n = 3 mice. d) Quantification of retrogradely labeled pIC neurons. pIC-CeA (4863 ± 996.7 s.e.m. total retrogradely labelled cells) and pIC-NAc-projectors (2050 ± 642.0 s.e.m. total retrogradely labelled cells) were mostly non-overlapping, with < 6% of cells (405.7 ± 21.46 cells) projecting to both. e) Both populations, when normalized to total cell counts, distributed similarly in the different pIC sub regions. f) Distribution of CeA- and NAc projectors in the anterior-posterior axis of the insular cortex (+2.4 to -1.22 mm from Bregma). In anterior insula we found more NAc-projectors than CeA-projectors. In contrast, in posterior insula (blue box), CeA-projectors were more abundant than NAc-projectors. g) Schematic of anterograde labeling of pIC axons. h) Representative images of eYFP-labelled pIC axons in the Amygdala (left) and Nucleus

Accumbens (right). Note the strong innervation within patches in the NAcc. Similar results were replicated in three mice. i)-j) Quantification of innervation densities of pIC axons in the CeA (i) and NAc (j) in the anterior-posterior axis, revealing sites of highest innervation densities (n = 3 mice). Sites of optic fiber implant for the following projection-specific experiments are marked with arrows. Lines and bar graphs are mean \pm s.e.m. Scale bars represent 500 μ m. Bar and line graphs indicate mean \pm s.e.m. Panels a)-j) are adapted from my publication¹⁷¹ as permitted by the author reuse rights of Nature Springer.

2.3 Functional Characterization of pIC→CeA and pIC→NAcc

To investigate the roles of pIC→CeA as well as pIC→NAcc, I infected pIC projection neurons with opsin-expressing AAV vectors as described above. The implantation of the optic fibers was guided by the innervation densities mentioned in **Chapter 2.2.4**; for the CeA at AP: 1.25 mm, ML: 2.75 mm, DV: -4.3 mm from Bregma and for NAcc at AP: +0.9 mm, ML: 1.3 mm, DV: -4.7 mm from Bregma (**Figure 17a,b**).

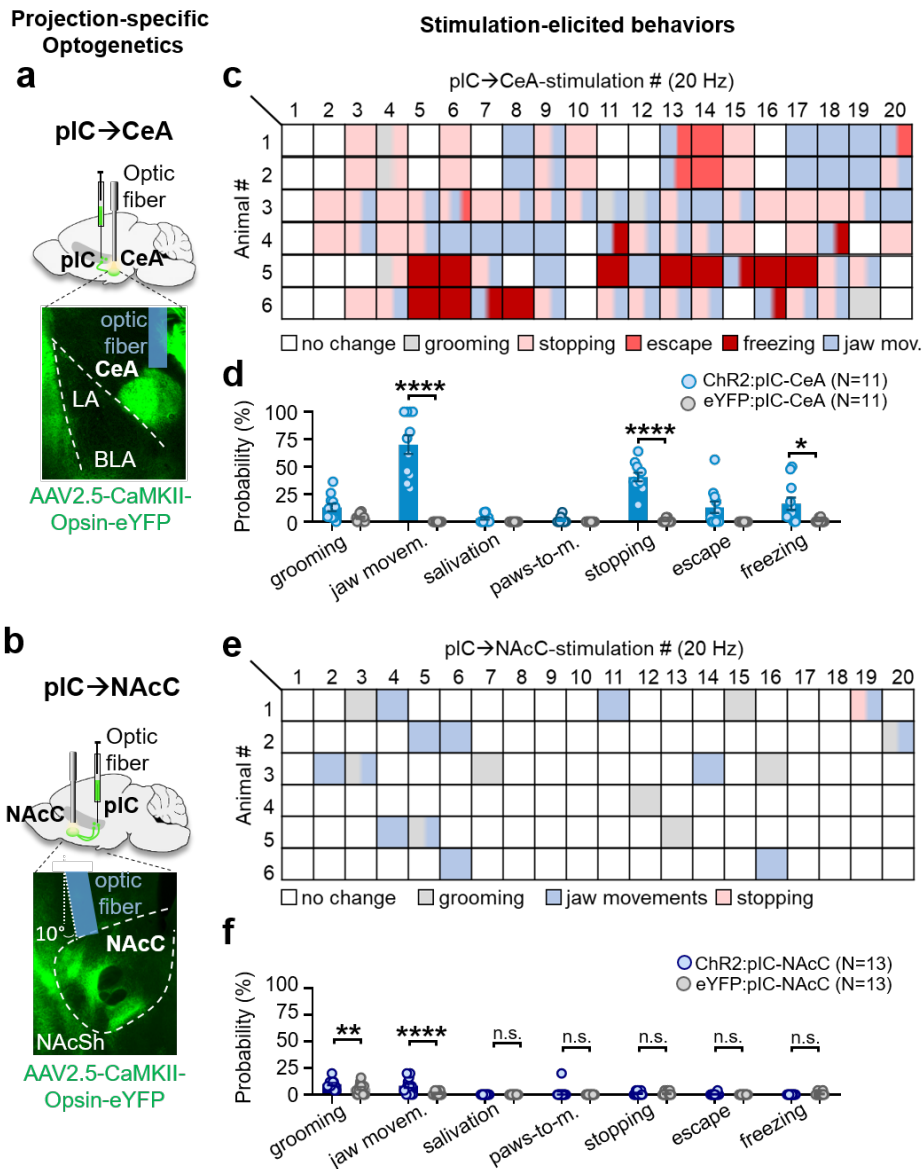


Figure 17. Stimulation-induced behaviors of pIC→CeA or pIC→NAcc. a)-b), Viral injection and optic fiber placement for a, pIC→CeA or b, pIC→NAcc projection-specific optogenetics. c)-f), Stimulation-elicited behavioral reactions upon 20 Hz stimulation of the pIC→CeA or pIC→NAcc. c) and e) show the reactions over time to successive stimulations from 6 representative animals for each pathway. c) Note the prominent reactions in the pIC→CeA pathway stimulated animal, e) while very few stimulations elicited reactions in the pIC→NAcc stimulated animal. d, Quantification of the stimulation-elicited reactions upon pIC→CeA stimulation in n = 11 animals / group, two-way RM ANOVA, group (opsin) effect, $F(1, 20) = 92.41$, $p < 0.0001$; behavior effect, $F(6, 120) = 28.64$, $p < 0.0001$; group x behavior interaction, $F(6, 120) = 29.30$, $p < 0.0001$; Bonferroni post-hoc analysis revealed significant differences between eYFP and ChR2 animals for jaw movements, stopping, both **** $p < 0.0001$, and freezing * $p = 0.0126$. No differences were found for grooming $p = 0.3727$, paws-to-mouth $p > 0.9999$ and salivation while a trend was observed for escapes $p = 0.0503$. f) Quantification of the stimulation-elicited reactions upon pIC→NAcc stimulation in n = 13 animals / group, two-way RM ANOVA, group (opsin) effect, $F(1, 24) = 12.67$, $p = 0.0016$; behavior effect, $F(6, 144) = 24.82$, $p < 0.0001$; group x behavior interaction, $F(6, 144) = 5.282$, $p < 0.0001$; Bonferroni post-hoc analysis revealed significant differences between eYFP- and ChR2-expressing animals for grooming ** $p = 0.0095$ and jaw movements **** $p < 0.0001$. No differences were observed for escapes, paws-to-mouth, salivation freezing or stopping, all $p > 0.9999$. Panels a) and b) are adapted from my publication¹⁷¹ as permitted by the author reuse rights of Nature Springer.

2.3.1 Stimulation-induced Behaviors

First, I analyzed stimulation-induced behaviors at 20 Hz as described above for the global pIC activation (**Figure 8c-f**). Resembling global pIC activation, stimulation of pIC→CeA elicited a subset of the behaviors, namely stopping, freezing and jaw movements (**Figure 17c,d**), however, less severe in their impact on the animals behavior.

Stimulating the pIC→NAcc terminals did not cause any reaction except occasional jaw movements or grooming (**Figure 17e,f**). These results suggest that a subset of the aversive behaviors seen upon pIC activation are transmitted *via* excitatory glutamatergic projections to the CeA. Further, stimulating pIC→CeA decreased locomotion at 20 Hz, but not at 5 Hz or 10 Hz, while activation of the pIC→NAcc projection had no effect on locomotion (**Figure 18**).

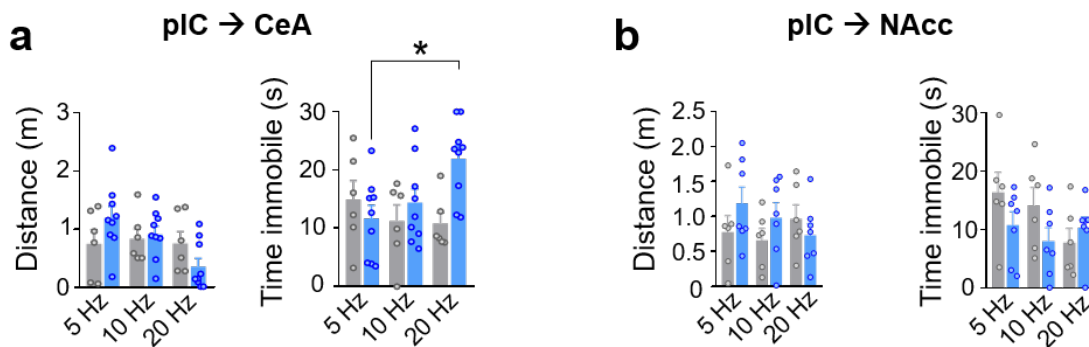


Figure 18. Optogenetic stimulation at 20 Hz causes increased immobility for pIC→CeA, but not for pIC→NAcc. a) Test for frequency-dependent effects on locomotion. Activation of pIC terminals in the CeA ($n = 6$ eYFP mice, $n = 9$ Chr2 mice) did not affect the distance travelled (two-way RM ANOVA $F(1, 13) = 0.07393$, $p = 0.7900$), but activation increased the time spent immobile (two-way RM ANOVA $F(1, 13) = 7.464$, $*p = 0.0171$, Bonferroni post-hoc analysis revealed significant differences between 5 and 20 Hz in the Chr2 group $*p = 0.0266$). b) Activation of the pIC→NAcc did not affect locomotion at any frequency ($n = 6$ eYFP mice, $n = 7$ Chr2 mice, two-way RM ANOVA for frequency: $F(2,48) = 2.306$, $p = 0.1106$; and for opsin ($F(3,24) = 0.4337$, $p = 0.7309$). Panels a) and b) are adapted from my publication¹⁷¹ as permitted by the author reuse rights of Nature Springer.

Because of the strong impairment of locomotion at 20 Hz, I chose 10 Hz for 1 s ON and 4 s OFF for all following pIC→CeA experiments, except where otherwise stated. As I did not observe an effect on locomotion for pIC→NAcc at 20 Hz, I kept this frequency for 1 s ON and 4 s OFF during the subsequent experiments.

2.3.2 Real-time Place Aversion Assay

Next, I wanted to test if activation of the two projections would induce avoidance behavior as observed during global pIC stimulation (Figure 9). While activation of pIC→CeA lead to a robust aversion (Figure 19a), stimulation of pIC → NAcc had no effect on preference (Figure 19b). Interestingly, the inhibition of either pathway did not affect place-preference (Figure 19a,b).

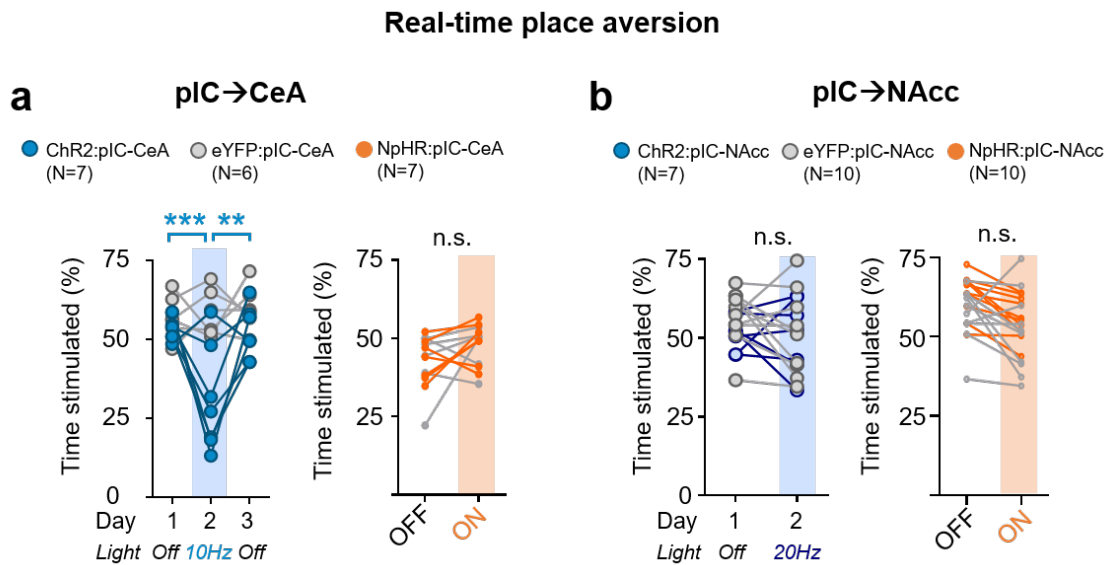


Figure 19. Stimulation of the pIC→CeA pathway elicits avoidance, whereas pIC→NAcc stimulation has no effects. a) Left: pIC→CeA stimulation resulted in real-time place aversion behavior (n = 7 ChR2 and n = 6 eYFP mice, two-way RM ANOVA revealed significant differences for group (opsin) $F(1, 11) = 21.15$, $p = 0.0008$ and light effect $F(2, 22) = 5.531$, $p = 0.0113$ as well as opsin x laser interaction $F(2, 22) = 5.368$, $p = 0.0126$; Bonferroni post-hoc analysis revealed significant differences between the habituation (day 1, laser off) and laser on (day 2) $***p = 0.008$, as well as the laser on (day 2) and memory test (day 3 laser off) $**p = 0.0017$ for the ChR2 group but no difference for the eYFP group, comparisons between light on and off days $p > 0.9999$). The eYFP and ChR2 animals exhibited a different preference only under light stimulation $****p < 0.0001$. Right: Inhibition of pIC terminals over CeA did not affect the animals' preference for the stimulated chamber (n = 7 NpHR mice, n = 6 eYFP mice, two-way RM ANOVA laser ($F(1,11) = 2.959$, $p = 0.1134$), group ($F(1,11) = 0.1724$, $p = 0.6860$). b) Left: Laser stimulation of the pIC→NAcc pathway did not influence place preference (n = 7 ChR2 and n = 10 eYFP mice, two-way RM ANOVA revealed no significant differences for group (opsin) $F(1, 15) = 0.5608$, $p = 0.4655$, light $F(1, 15) = 1.208$, $p = 0.2890$, or opsin x laser interaction, $F(1, 15) = 0.6262$ $p = 0.441$). Right: Inhibition of pIC terminals over NAcc did not affect the animals' preference for the stimulated chamber (n = 10 mice / group, two-way RM ANOVA, laser ($F(1,18) = 9.399$, $p = 0.067$). Panels a) and b) are adapted from my publication¹⁷¹ as permitted by the author reuse rights of Nature Springer

2.3.3 Breathing Rate

Analogous to the experiment in **Chapter 2.2.1**, I measured the breathing rate of lightly anesthetized mice during optogenetic stimulation of the two projections. As I did not find an effect of pIC inhibition on breathing or heart rate, I did not test the effect of inhibition of the two projections.

I found that pIC→CeA stimulation increased the breathing rate (**Figure 20a**), whereas pIC→NAcc stimulation did not modulate breathing (**Figure 20b**).

This result suggests, that the increase of respiratory rate that I observed during global pIC stimulation, was mediated, at least in part, by pIC→CeA.

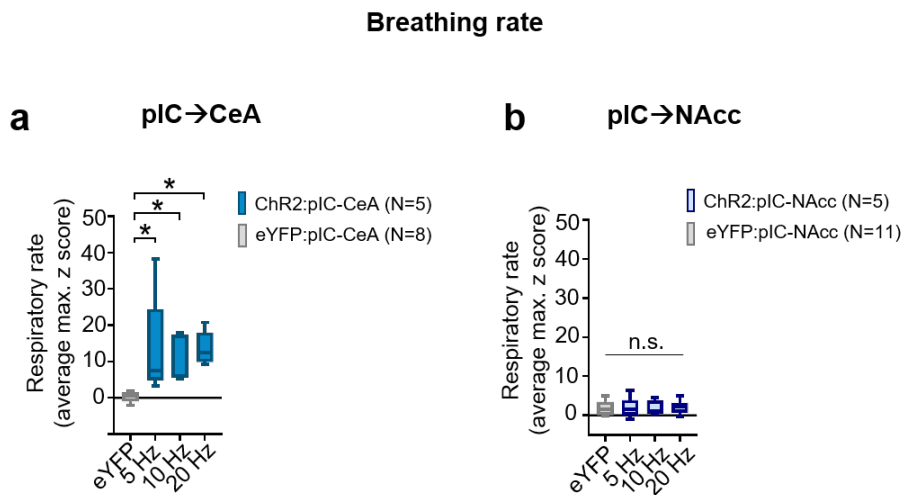


Figure 20. Optogenetic stimulation of pIC→CeA increases the breathing rate of anaesthetized mice. a) pIC→CeA stimulation induced increases in respiratory rates in anesthetized animals (n = 5 ChR2 and n = 8 eYFP mice, one-way ANOVA, $F(3, 19) = 5.098$, $p = 0.0093$; Bonferroni multiple comparisons to eYFP controls: 5 Hz, $*p = 0.0214$; 10 Hz, $*p = 0.0296$, 20 Hz, $*p = 0.0172$). b) pIC→NAcc stimulation did not affect respiratory rates (n = 5 ChR2 and n = 11 eYFP mice, one-way ANOVA, $F(3, 21) = 0.02645$, $p = 0.9940$). Panels a) and b) are adapted from my publication¹⁷¹ as permitted by the author reuse rights of Nature Springer.

2.3.4 Real-time Optogenetic Manipulation during EPM and EZM

Next, I tested the influence of projection-specific manipulations on anxiety-related behavior using the same experimental approach as for the pIC (see Methods, **Figure 13**). Interestingly, activating as well as inhibiting pIC→CeA caused bidirectional effects that were similar to those elicited by pIC manipulation: Inhibition of pIC→CeA had strong anxiolytic effects in a high-anxiety environment in the EPM, but it did not further increase the exploration of the open arms of the EZM under low-anxiety settings (**Figure 21a,b**). Oppositely, activation of pIC→CeA had no effects in the high-anxiety environment on the EPM, but strong anxiogenic effects on the EZM, in in low-anxiety settings (**Figure 21b**).

In contrast, optogenetic manipulation of pIC→NAcc had no influence on any anxiety-related parameter (**Figure 21c,d**). These results suggest that pIC→CeA mediates the influence of pIC on anxiety states, but not pIC→NAcc.

Closed-loop anxiety-tests

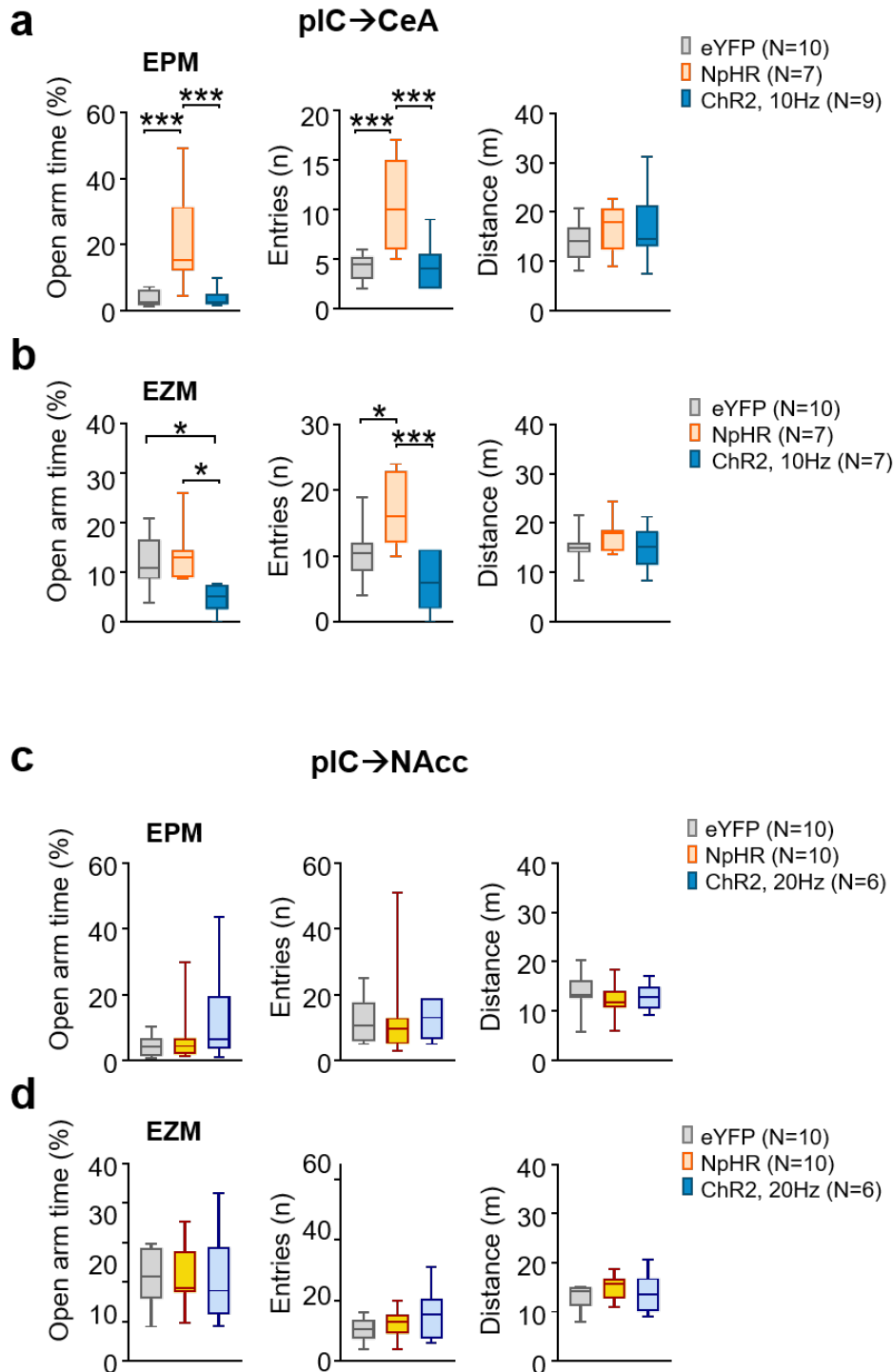


Figure 21. Real-time optogenetic manipulation of pIC→CeA bi-directionally influences anxiety-like behavior. Assessment of pathway-specific optogenetics on anxiety. a) pIC→CeA inhibition had anxiolytic effects in the EPM (n = 10 eYFP, n = 7 NpHR, n = 9 ChR2 mice). Open-arm time: one-way ANOVA, $F(2, 23) = 11.87$, $p = 0.0003$; Bonferroni post-hoc analysis: eYFP vs. NpHR, $***p = 0.0006$; eYFP vs. ChR2, $p > 0.9999$; NpHR vs. ChR2, $***p = 0.0009$. Open-arm entries: One-way ANOVA, $F(2, 23) = 13.48$, $p = 0.0001$; Bonferroni post-hoc: eYFP vs. NpHR, $***p =$

0.0004, eYFP vs. Chr2, $p = 0.9704$, NpHR vs. Chr2, $***p = 0.0003$. Distance travelled in the entire maze was not affected by optogenetic manipulations of pIC→CeA: One-way ANOVA, $F(2, 23) = 0.6430$, $p = 0.5349$. b) Stimulation of pIC→CeA had anxiogenic effects in the EZM, while inhibition only increased entries but not the time spent in the open arms ($n = 10$ eYFP, $n = 7$ NpHR, $n = 7$ Chr2 mice). Open-arm time: One-way ANOVA, $F(2, 21) = 6.343$, $p = 0.0070$; Bonferroni post-hoc analysis: eYFP vs. NpHR, $p > 0.9999$; eYFP vs. Chr2, $*p = 0.0221$; NpHR vs. Chr2, $*p = 0.0111$. Open-arm entries: One-way ANOVA, $F(2, 21) = 9.533$, $p = 0.0011$; Bonferroni post-hoc analysis: eYFP vs. NpHR, $*p = 0.0276$; eYFP vs. Chr2, $p = 0.2498$; NpHR vs. Chr2, $***p = 0.0009$. Distance travelled in the entire maze was not affected by optogenetic manipulations of pIC→CeA: One-way ANOVA, $F(2, 21) = 0.9968$, $p = 0.3859$. c-d) Optogenetic pIC→NAcc manipulations did not affect anxiety related-behaviors in the EPM or EZM ($n = 10$ eYFP, $n = 10$ NpHR, $n = 6$ Chr2 mice). c) EPM Open-arm time: One-way ANOVA, $F(2, 23) = 1.465$, $p = 0.2519$; EPM Open-arm entries: One-way ANOVA, $F(2, 23) = 0.01173$, $p = 0.9883$; Distance travelled in the EPM: One-way ANOVA, $F(2, 23) = 0.5072$, $p = 0.6088$. d) EZM Open-arm time: One-way ANOVA, $F(2, 23) = 0.006972$, $p = 0.9931$; EZM Open-arm entries: One-way ANOVA, $F(2, 23) = 1.544$, $p = 0.2349$; Distance travelled in the EZM: One-way ANOVA, $F(2, 23) = 1.244$, $p = 0.3068$. Box-whisker plots display median, 25th to 75th percentiles, and min to max values. Panels a-d) are adapted from my publication¹⁷¹ as permitted by the author reuse rights of Nature Springer.

2.3.5 Sucrose Preference Test

Given that pIC→NAcc manipulation did not affect autonomic functions, anxiety-related behaviors or avoidance, I was curious to find a behavior that would be influenced by manipulating that pathway. A literature search revealed, that a projection of D1R neurons of the nucleus accumbens to the ventral pallidum is able to interrupt licking of a sucrose solution¹⁸⁰. Further, a recent study identified that both D1R and D2R-expressing neurons of the nucleus accumbens receive IC innervation¹¹¹. Also, IC→NAc has been implicated in aversion-resistant alcohol intake¹⁰⁴.

Recently, the CeA has also been shown to not only mediate fear reactions, but also appetitive behaviors^{176,181,182}. As both the CeA as well as the NAcc are known to be involved in reward and consummatory behaviors^{176,178,183–185}, I performed a series of tests aimed at dissecting their specific roles in the context of appetitive behaviors.

First, I tested if manipulations of both pathways would affect the innate preference for a 10% sucrose solution. I trained water-deprived animals that underwent projection-specific surgeries to establish a stable licking baseline for ca. 5 days. Mice were then placed in a custom-built lick-o-meter chamber (50 cm x 30 cm x 30 cm) where they were presented with two licking spouts which would deliver water or sucrose and stimulated for 20 min with 1 s ON, 4 s OFF 10 Hz (CeA) or 20 Hz (NAcc) (473 nm, 3-5 mW, 5 ms pulse width) (**Figure 22a**). Neither activation nor inhibition of both pathways altered the sucrose preference (**Figure 22b,d**).

Sucrose preference

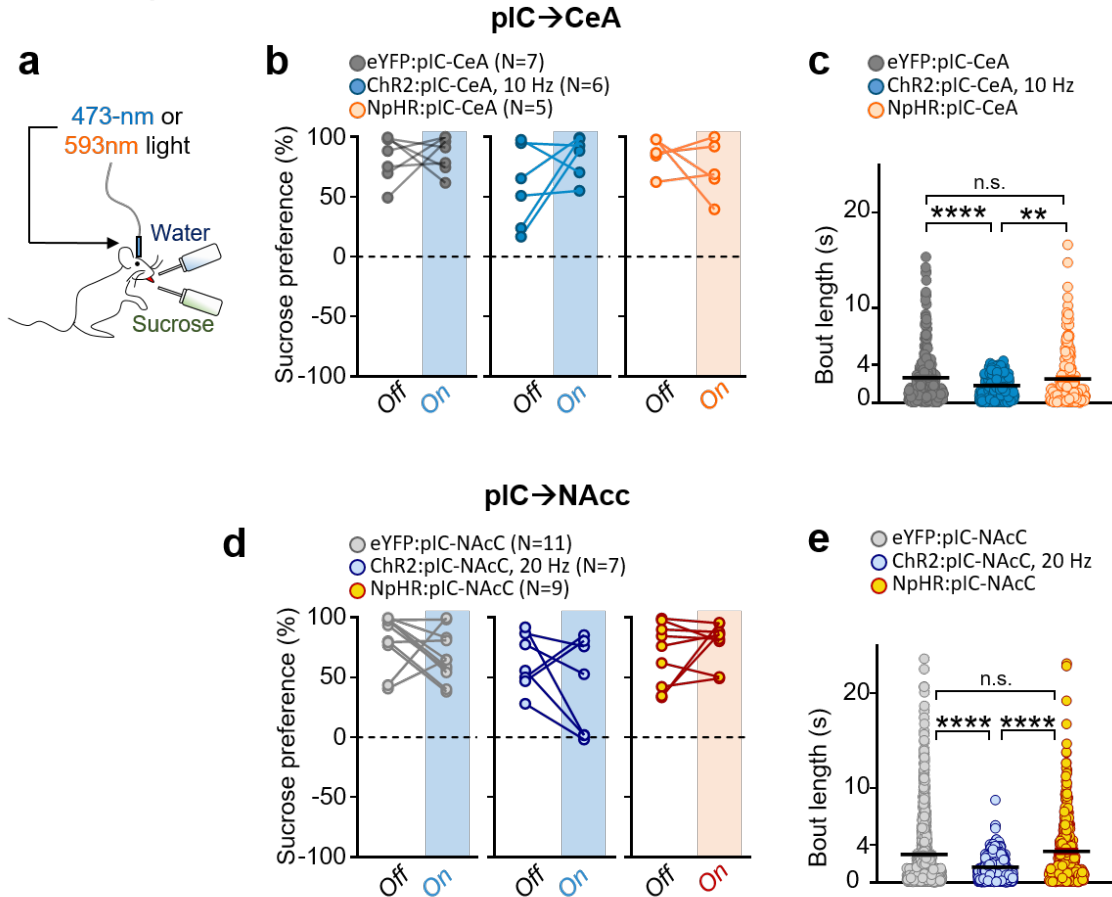


Figure 22. Optogenetic manipulation of both pathways does not influence innate sucrose preference, but laser interrupts ongoing licking. a)-e) Sucrose-preference and drinking behavior upon pathway-specific optogenetic manipulations. a) Illustration of open-loop sucrose preference paradigm. b) Sucrose-preference remains unaffected by pIC→CeA manipulations (n = 7 eYFP, n = 6 ChR2, n = 5 NpHR mice, two-tailed paired t tests comparing light ‘on’ and ‘off’ days: eYFP, $t = 0.2939$, $df = 6$, $p = 0.7788$; ChR2, $t = 1.529$, $df = 5$, $p = 0.1869$; NpHR, $t = 0.8977$, $df = 4$, $p = 0.4201$). c) pIC→CeA stimulation at 10 Hz interrupts ongoing drinking. Drinking bouts are reduced to the 4 s ISI (n = 301 bouts eYFP, 316 bouts ChR2, 248 bouts NpHR, one-way ANOVA, $F(2, 862) = 11.25$, $p < 0.0001$; Bonferroni post-hoc analysis: eYFP vs. ChR2, **** $p < 0.0001$; eYFP vs. NpHR, $p > 0.9999$; ChR2 vs. NpHR, ** $p = 0.0012$). d) Sucrose-preference remains unaffected by pIC→NAcc manipulations (n = 11 eYFP, n = 7 ChR2, n = 9 NpHR mice, two-tailed paired t tests comparing light ‘on’ and ‘off’ days: eYFP, $t = 1.538$, $df = 10$, $p = 0.1550$; ChR2, $t = 1.176$, $df = 6$, $p = 0.2842$; NpHR, $t = 1.106$, $df = 8$, $p = 0.3008$). e) pIC→NAcc stimulation at 20 Hz interrupts ongoing drinking. Drinking bouts are reduced to the 4s ISI (n = 700 bouts eYFP, 780 bouts ChR2, 334 bouts NpHR, one-way ANOVA, $F(2, 1811) = 58.26$, $p < 0.0001$; Bonferroni post-hoc analysis: eYFP vs. NpHR, $p = 0.2974$; ChR2 vs eYFP or NpHR, both **** $p < 0.0001$). Panels a)-e) are adapted from my publication¹⁷¹ as permitted by the author reuse rights of Nature Springer.

However, upon closer observation, I noticed that ongoing licking would be interrupted when it coincided with optogenetic stimulation of both pathways. Mice would either briefly retract their heads and continue to lick shortly after the laser turned off, or the stimulation led to a complete interruption of the session with the animal retreating to a corner of the lick-o-meter. I therefore

analyzed the duration of all licking bouts and noticed that Chr2-expressing CeA or NAcc mice rarely showed any bouts lasting longer than 4 s, whereas control animals were showing much longer bouts (**Figure 22c,e**). These results suggest, that due to the 1 s ON, 4 s OFF stimulation paradigm, the mice could only lick during the 4 s OFF period.

To better understand this effect, I designed a closed-loop licking experiment, where the first lick would lead to a 1 s long optogenetic stimulation of 5, 10 or 20 Hz (**Figure 23a**). I performed this experiment only in a pIC→NAcc Chr2-expressing cohort.

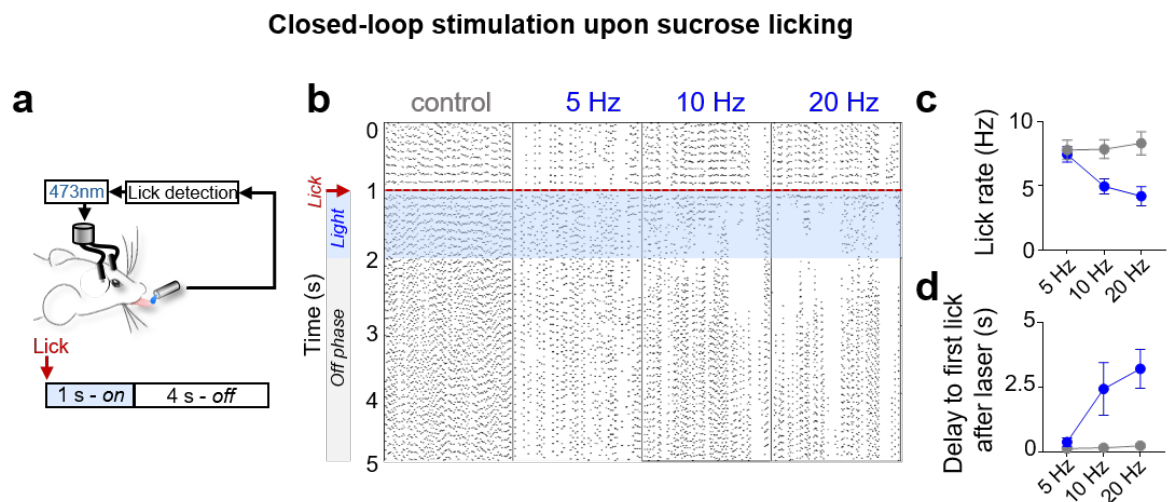


Figure 23. Closed-loop optogenetic stimulation of licking behavior interrupts licking in pIC→NAcc mice in a frequency-dependent manner. a) Experimental strategy to trigger laser stimulation selectively, when mice start to lick from a spout. After the first lick, the laser would pulse for 1s at either 0,5,10 or 20 Hz (473 nm, 3-5 mW, 5 ms pulse width), followed by a timeout of 4 s. b) Lick raster plots show that at 10 Hz the licking started to be interrupted. c) The lick rate within the 1 s laser stimulation period was reduced in a frequency-dependent manner. d) Stimulation caused mice to interrupt their licking for longer than the 1s duration of the laser activation. Panels a)-d) are adapted from my publication¹⁷¹ as permitted by the author reuse rights of Nature Springer.

In control mice, the 1 s laser stimulation did not induce any alterations in lick rate or delay to first lick after laser. In the Chr2 expressing mice, there were minor irregularities apparent in the licking pattern at 5 Hz, which increased in a frequency-dependent manner at 10 and 20 Hz. At 20 Hz, the licking could be interrupted in almost all cases and in some instances the mice would move away entirely from the licking spout (**Figure 23b-d**)

These results confirmed that optogenetic stimulation of pIC→NAcc immediately and powerfully interrupt ongoing licking behavior.

2.3.6 Feeding under Optogenetic Stimulation

Given the ability to completely interrupt licking of a liquid, I immediately wondered, how such a manipulation would affect eating of solid food. Therefore, I acutely food-deprived mice for 24 h and presented the animals with a standard food pellet in an empty home-cage. I would manually trigger the optogenetic stimulation (1 s, at 10 Hz (CeA) or 20 Hz (NAcc), 473 nm, 3-5 mW, 5 ms pulse width) when the mice started to nibble on the food pellet (**Figure 24a**).

Interestingly, stimulation of both projections immediately interrupted feeding attempts. This effect was so powerful, that hungry animals would be almost completely stopped from ingesting food (**Figure 24b,c**).

Notably, inhibition of pIC→NAcc or pIC→CeA in food-deprived mice did not alter the amount of consumed food (data not shown). This suggests that both pathways specifically transmit aversive signals to their subcortical targets and are not necessary for regular food consumption.

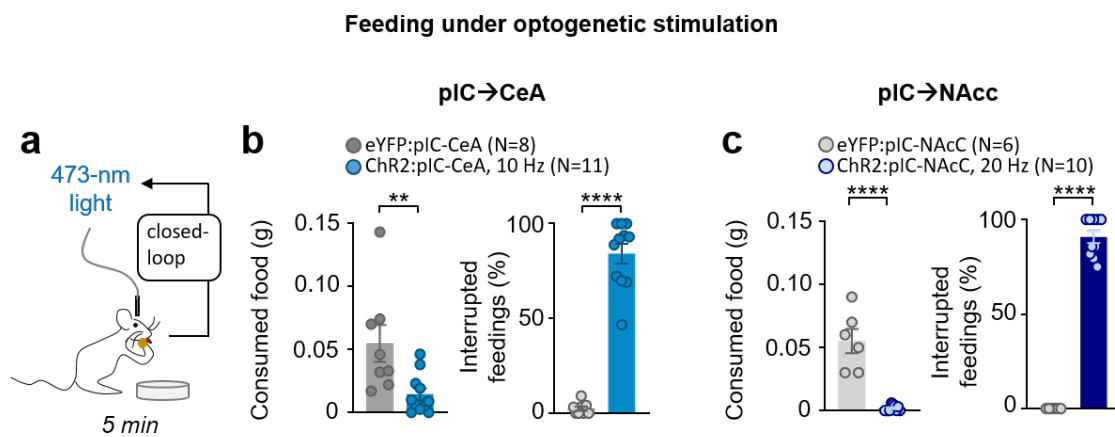


Figure 24. Optogenetic stimulation of both pathways powerfully prevents food-deprived mice from feeding. a) Experimental design for closed-loop manipulations during feeding bouts. b) pIC→CeA stimulation reduced food consumption (left, $n = 8$ eYFP, $n = 11$ ChR2 mice, two-tailed unpaired t test, $t = 2.973$, $df = 17$, $**p = 0.0085$) and reliably interrupted ongoing feeding bouts (right, $n = 8$ eYFP, $n = 11$ ChR2 mice, two-tailed unpaired t test, $t = 13.12$, $df = 17$, $****p < 0.0001$). c) pIC→NAcc stimulation strongly reduced food consumption (left, $n = 6$ eYFP, $n = 10$ ChR2 mice, two-tailed unpaired t test, $t = 7.271$, $df = 14$, $****p < 0.0001$) and reliably interrupted ongoing feeding bouts (right, $n = 6$ eYFP, $n = 10$ ChR2 mice, two-tailed unpaired t test, $t = 21.51$, $df = 14$, $****p < 0.0001$). Panels a)-c) are adapted from my publication¹⁷¹ as permitted by the author reuse rights of Nature Springer

2.3.7 Quinine Avoidance Test

Previous studies from the laboratory of Charles Zuker described the term “bitter cortical field” for a region that is partially overlapping with the subdivision of IC that I classified as mIC and pIC¹⁴⁸. They showed that optogenetic stimulation of this “bitter spot” elicits avoidance and a range of unconditioned aversive behaviors. When they inactivated the bitter cortical field, they could strongly disturb taste discrimination. In this study, I did not try to reproduce this finding, however, I wanted to investigate if one of the two pathways are involved in mediating the aversive reactions to bitter tastes.

To test this, I measured the quinine preference index analogous to the sucrose preference. In brief, mice that have undergone the sucrose preference test have re-established a stable licking response and were offered water or a 0.5 mM quinine solution on the test day during acute optogenetic manipulation.

Manipulations of both pathways in an open-loop fashion with 1 s ON, 4 s OFF, or constant inhibition for 20 min did not affect the strong innate aversion to quinine (**Figure 25a**). As a prolonged projection-specific inhibition of axons might elicit paradoxical effects due to reversal of the chloride reversal potential¹⁸⁶, I analyzed the development of the quinine aversion over time. Animals avoided the quinine already after the first licks and did not reverse their aversion over time (**Figure 25b**).

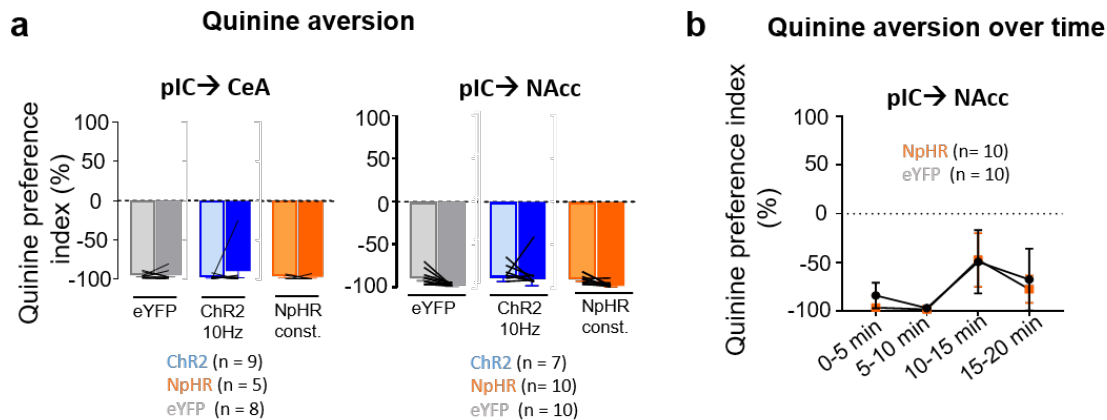


Figure 25. Quinine Aversion is not affected by optogenetic manipulation of pIC→CeA or pIC→NAcc. a) Optogenetic manipulation of neither the pIC-CeA nor the pIC-NAcc pathway impacts quinine aversion. Quinine aversion was not altered upon activation or inhibition of neither the pIC-CeA pathway (light on versus light off, two-tailed paired t tests: eYFP (n = 8), $t = 0.274$, $df = 7$, $p = 0.791$; ChR2 (n = 9), $t = 0.896$, $df = 8$, $p = 0.397$; NpHR (n = 5), $t = 0.358$, $df = 4$, $p = 0.738$) nor the pIC-NAcc pathway (light on versus light off, two-tailed paired t tests: eYFP (n = 10), $t = 0.279$, $df = 14$, $p = 0.784$; ChR2 (n = 7), $t = 0.169$, $df = 12$, $p = 0.868$; NpHR (n = 10), $t = 0.449$, $df = 8$, $p = 0.665$). b) Expression of quinine aversion during the entire trial in 5 min bins. Inhibition of the pIC-NAcc pathway did not alter the course of quinine avoidance in comparison to EYFP controls (n = 10 mice / group, mixed-model ANOVA, opsin effect: $F(1, 18) = 0.1610$,

$p = 0.6930$). Panels a) and b) are adapted from my publication¹⁷¹ as permitted by the author reuse rights of Nature Springer.

2.3.8 Social Interaction

To test if the interruptions in feeding and drinking might generalize to alternative rewards, I manipulated the projections while mice socially interacted with juveniles (**Figure 26a**). This experiment has been inspired by recent findings which implied the IC in approach and avoidance responses to social affective stimuli^{98,99}.

Interestingly, I found that stimulation of pIC→CeA interrupted social interactions which led to a strongly reduced average bout duration, but not pIC→NAcc stimulation (**Figure 26b,c**). As the total time the mice interacted with the juvenile conspecifics was not reduced upon pIC→CeA activation, the motivation to socially interact seemed to not be directly disturbed. Indeed, the number of interactions was slightly increased upon pIC→CeA stimulation (**Figure 26b**, right). Thus, the observed inhibition of behavior seemed to be generalized during pIC→CeA stimulation.

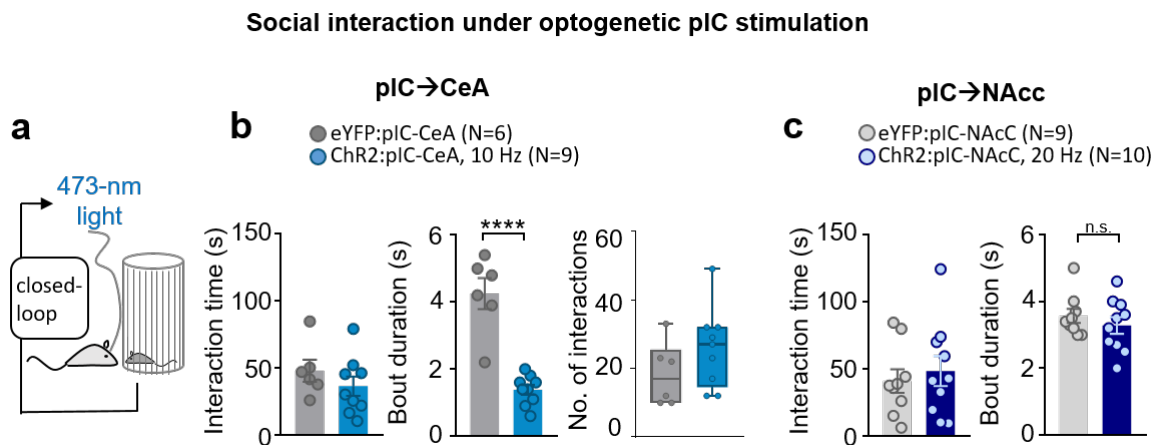


Figure 26. Optogenetic stimulation of pIC→CeA but not pIC→NAcc interrupts ongoing social interaction. a) Experimental design for closed-loop manipulations during social interactions. b) While pIC→CeA stimulation did not affect the overall time the animals interacted (left, $n = 6$ eYFP, $n = 9$ ChR2 mice, two-tailed unpaired t test, $t = 1.048$, $df = 13$, $p = 0.3138$), the stimulation acutely interrupted ongoing social interactions as seen in a significant reduction in the duration of individual interaction bouts (middle, $n = 6$ eYFP, $n = 9$ ChR2 mice, two-tailed unpaired t test, $t = 6.908$, $df = 13$, **** $p < 0.0001$). There was a trend towards increased number of interaction bouts (right). c) pIC→NAcc stimulation did not affect social interactions ($n = 9$ eYFP, $n = 10$ ChR2 mice; left: total interaction time, two-tailed unpaired t test, $t = 0.5167$, $df = 17$, $p = 0.6120$; right: bout length: two-tailed unpaired t test, $t = 0.8693$, $df = 17$, $p = 0.3968$). Panels a)-c) are adapted from my publication¹⁷¹ as permitted by the author reuse rights of Nature Springer.

2.3.9 Lithium Chloride-induced Anorexia

Visceral sickness (malaise) can powerfully inhibit eating, which you might have experienced yourself during a noro-virus infection. Existing literature strongly implies the IC in processing malaise¹⁸⁷ as well as conditioned taste aversion (CTA)^{73,188,189}. As my findings suggest that both CeA and NAcc can powerfully interrupt feeding, I next wanted to test, if these pathways could be mediating an acute anorexic effect of lithium chloride (LiCl)-induced malaise.

For CTA, a novel taste is paired with the injection of LiCl, which leads to robust aversion of this taste in a recall test. However, acute anorexic effects on feeding are less well established. In a pilot experiment, I tested the effect of acute LiCl (50, 100 and 150 mg/KG BW) on sucrose consumption in water-deprived mice, but surprisingly this did not affect sucrose consumption (see **Appendix 6**). This indicated that thirst and/or the reward of a sucrose solution can overcome the acute effects of visceral malaise. However, in another pilot experiment, I observed that mice would strongly reduce their feeding during acute LiCl (150 mg/kg) (data not shown).

After having established this anorexic effect on food consumption with LiCl in wild-type animals, I next tested in projection-specific cohorts if the two pathways are involved in suppressing feeding under malaise (**Figure 27a**).

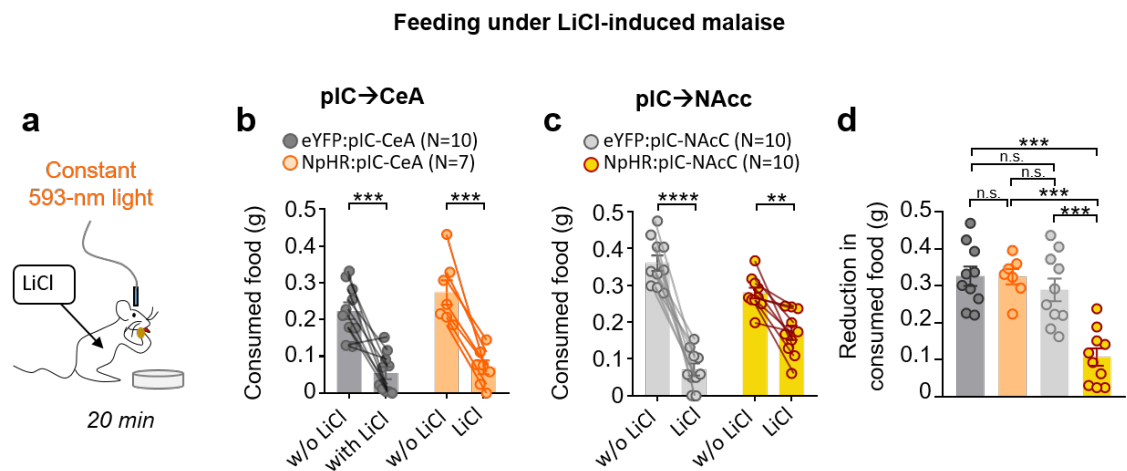


Figure 27. Inhibition of pIC→NAcc partially rescues LiCl-induced anorexia. a) Experimental design for constant pathway inhibition during feeding under visceral malaise (LiCl, lithium chloride). a)-d) Food consumption in hungry animals was reduced under the influence of LiCl whether or not the pIC→NAcc or pIC→CeA were inhibited. b) pIC→CeA groups: food consumption was reduced by LiCl under constant orange light in both, eYFP- (left: n = 10 mice, two-tailed paired t test, $t = 5.143$, $df = 9$, $***p = 0.0006$) and NpHR-expressing animals (right: n = 7 mice, two-tailed paired t test, $t = 6.844$, $df = 6$, $***p = 0.0005$). c) Food consumption was also reduced under the same conditions when the pIC→NAcc pathway was manipulated (left: n = 10 eYFP mice, two-tailed paired t test, $t = 9.517$, $df = 9$, $****p < 0.0001$; right: n = 10 NpHR mice, two-tailed paired t test, $t = 4.629$, $df = 9$, $**p = 0.0012$). d) However, pIC→NAcc inhibition reduced the anorexigenic effects of LiCl on food consumption (for pIC→CeA n = 10 eYFP and n = 7 NpHR mice, for pIC→NAcc n = 10 eYFP and 10 NpHR mice, one-way ANOVA, $F(3, 33) = 16.36$, $p < 0.0001$, Bonferroni post-hoc analysis revealed significant differences ($****p <$

0.0001) for NpHR:pIC→NAcc vs. NpHR: pIC→CeA, NpHR:pIC→NAcc vs. eYFP:pIC→CeA and NpHR:pIC→NAcc vs. eYFP:pIC→NAcc; no differences ($p > 0.999$) were detected for NpHR:pIC-CeA vs. eYFP:pIC-CeA, NpHR:pIC-CeA vs. eYFP:pIC-NAcc, or eYFP:pIC-NAcc vs eYFP:pIC-CeA). Panels a)-d) are adapted from my publication¹⁷¹ as permitted by the author reuse rights of Nature Springer.

Again, all mice significantly reduced feeding in comparison to a baseline measurement when LiCl was administered shortly before feeding (**Figure 27b-d**). However, animals in which I silenced pIC→NAcc displayed a partial rescue, consuming more food than control animals or pIC→CeA mice (**Figure 27d**). Control experiments showed that inhibition of both projections had no effect on food intake in food-deprived mice (see **Appendix 7**).

These results suggest, that pIC→NAcc, but not pIC→CeA, contributes to the anorexic effects mediated by LiCl-induced malaise.

2.3.10 Fear-induced Anorexia

As pIC→CeA was not implicated in malaise-induced anorexia, I wanted to find a natural stimulus through which this pathway could mediate its anorexic effects. The CeA has been shown to mediate acute fear behavior such as freezing or flight¹⁷⁶. A commonly used olfactory stimulus to induce fear in mice is a predator odor, e.g. synthetic fox urine Trimethylthiazoline (TMT)¹⁹⁰.

Analogous to the malaise-induced anorexia, I designed a feeding task, where food-deprived mice were exposed to TMT and presented with a food pellet in an empty home cage (**Figure 28a**). I would constantly inhibit both pathways for 10 min (593 nm, 10 mW) and quantify the consumed food and the number of feeding bouts.

The presence of TMT reduced the total amount of food consumed in comparison to baseline conditions and all animals strongly reduced their number of feeding bouts (see **Appendix 7**). Interestingly, mice in which I inhibited the pIC→CeA had an increased number of feeding bouts compared to the controls (**Figure 28b**). Inhibition of pIC→NAcc did neither affect the amount of food consumed nor the number of feeding bouts (**Figure 28c**).

Although not being able to rescue the quantity of consumed food in the presence of TMT, the effect on the approach of food could be partially rescued by pIC→CeA silencing.

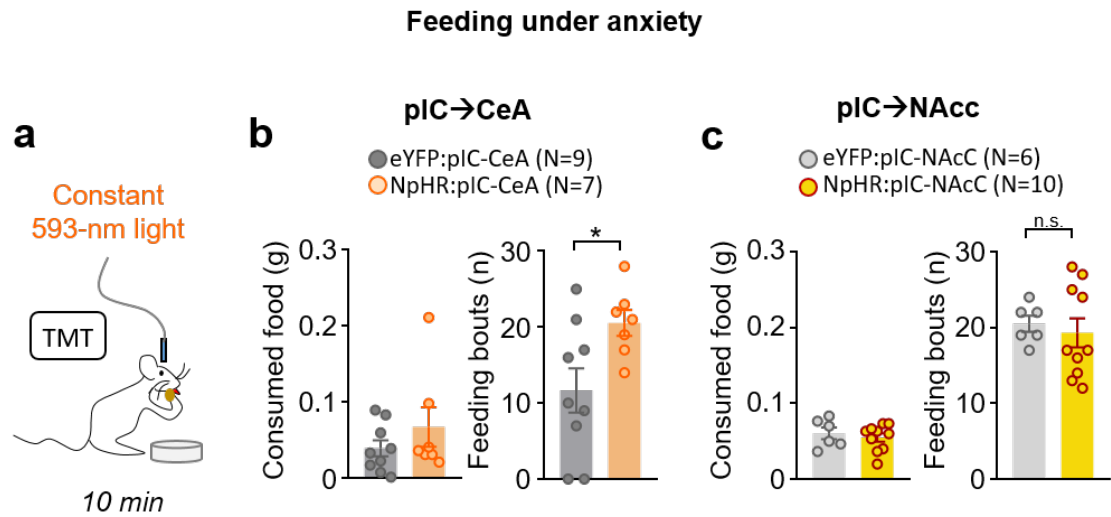


Figure 28. Anxiety-mediated anorexia is slightly ameliorated by pIC→CeA inhibition. a) Experimental design for constant pathway inhibition during feeding under predator threat (synthetic fox odor, TMT). b) The overall food consumed under pIC→CeA inhibition (n = 9 eYFP mice, n = 7 NpHR mice) in the presence of TMT was unaltered (two-tailed unpaired t test, $t = 1.089$, $df = 14$, $p = 0.2944$), however animals performed more feeding bouts than controls in the presence of TMT (two-tailed unpaired t test, $t = 2.434$, $df = 14$, $*p = 0.0289$). c) pIC→NAcc inhibition (n = 6 eYFP mice, n = 10 NpHR mice) had no effect on the amount of consumed food (left, two-tailed unpaired t test, $t = 0.5998$, $df = 14$, $P = 0.5582$), or on the number of feeding bouts in the presence of TMT (right, two-tailed unpaired t test, $t = 0.4547$, $df = 14$, $p = 0.6563$). Bar graphs indicate mean \pm s.e.m. Panels a)-c) are adapted from my publication¹⁷¹ as permitted by the author reuse rights of Nature Springer.

2.3.11 Controlling for Back-propagating Action Potentials induced by Projection-specific Stimulations

One caveat of optogenetic activation of axon terminals is the potential to elicit back-propagating action potentials (APs)^{191,192}. These APs travel “backwards” along the axon, eventually reaching the soma of the neuron. There, these APs could stimulate the axon initial segment and thereby elicit new APs, or lead to dendritic release of BDNF¹⁹³. As neurons can heavily collateralize their axon, this would lead to neurotransmitter release at other synapses than the intended one. Thus, there is the danger to falsely attribute a behavioral effect to a specific synapse when performing projection-specific optogenetic experiments.

Another caveat of projection-specific manipulations is the potential to influence opsin-expressing fibers that merely travel through the illuminated area under the optic fiber, but do not actually synapse in that target region. Ultimately, it could be the manipulation of these passing fibers that elicit the observed behaviors, and not the targeted synapses.

In order to control for both of these issues, I modified previously reported control experiments^{174,184}. In brief, the idea is to first pharmacologically block local glutamatergic signaling at the target site and subsequently perform projection-specific optogenetic experiments. This is only possible in GABAergic target regions, such as the CeA or the NAcc, as for example in cortex, such a strategy would certainly lead to a very strong modification of local processing.

Thus, I implanted opto-fluid cannulas, which allow the sequential insertion of a liquid-injector followed by insertion of an optic fiber (see Methods). First, I bilaterally infused the CeA or the NAcc with NBQX (5 mg/ml, 150 μ l per side), then inserted the optic fibers and after an hour tested the animals in the feeding task described in **Chapter 2.3.6**.

I could confirm that back-propagation of terminal stimulation as well as activation of fibers of passage was limited since behavioral effects were potently disrupted upon blocking glutamatergic transmission within the target region (**Figure 29a,b**).

This important control experiment, together with the fact that pIC→CeA and pIC→NAcc manipulations were markedly different, suggests that the projection-specific experiments indeed measured the influence of the targeted synapses.

Back propagation assessment in projection-specific optogenetics

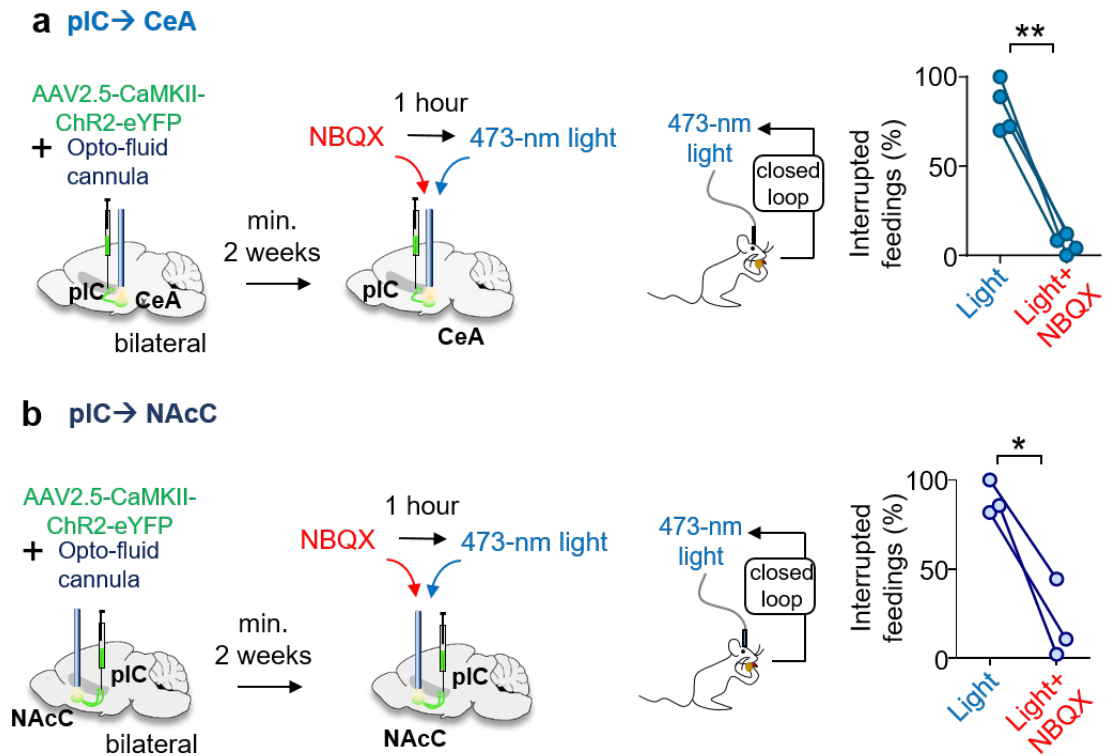


Figure 29. Control experiment shows that back-propagating action-potentials do not cause feeding interruption. a) Opto-fluid cannulas were bilaterally implanted over the CeA to test if feeding interruption is caused by glutamate release of insular terminals. Indeed, blocking glutamate signalling within the CeA with the AMPA-Antagonist NBQX (5 mg/ml) abolished the effect mediated by optogenetic stimulation ($n = 4$ mice, two-tailed paired t test, $t = 9.162$, $df = 3$, $**p = 0.0027$). b) I applied the same strategy for the pIC → NAcC pathway and bilaterally infused NBQX 1 h prior to optogenetic stimulation during feeding. Again, blocking AMPA-Receptors was sufficient to abolish the feeding interruption ($n = 3$ mice, two-tailed paired t test, $t = 8.668$, $df = 2$, $*p = 0.0131$). This suggests that interruption of feeding is not mediated by passing fibers expressing ChR2 or by back propagation of action potentials, but by monosynaptic glutamate release from pIC terminals in the CeA and NAcC. Panels a) and b) are adapted from my publication¹⁷¹ as permitted by the author reuse rights of Nature Springer.

3 DISCUSSION

By performing comprehensive anatomical and physiological circuit analyses in mice, I here provided a whole-brain connectivity map for the entire IC and defined a role for the pIC in influencing aversive states and regulating behavior via top-down projections to subcortical brain regions.

3.1 Connectivity of the Mouse Insular Cortex

In this study, I mapped the inputs and outputs of the anterior, medial and posterior IC of the mouse to generate a whole-brain IC connectome. All IC subdivisions are broadly connected to many functionally diverse parts of the brain, with a substantial degree of intra-insular cross talk. Each subdivision is a multi-modal hub and might process multiple aspects of bodily information and internal state.

Big picture maps for IC subdivisions

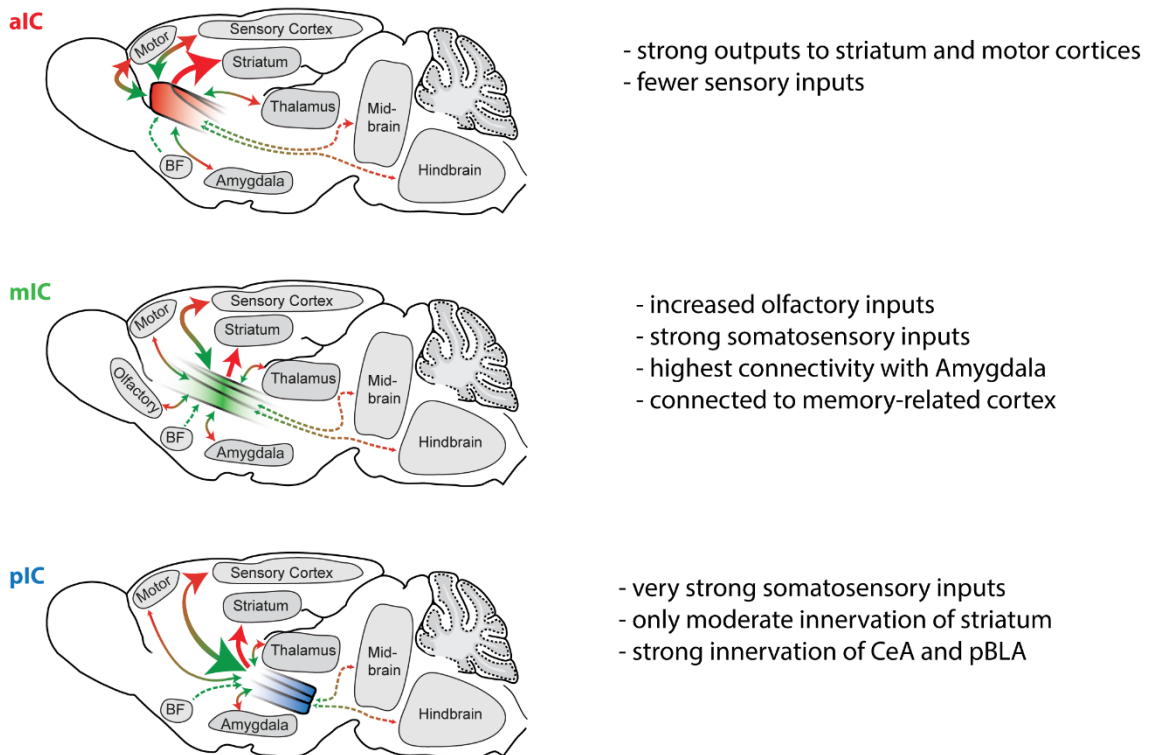


Figure 30. Cartoon of the broad connectivity scheme of aIC, mIC and pIC with key brain structures. Red arrows indicate projections from IC; green arrows indicate inputs to IC. The weight of the arrows is proportional to % of total input/output.

In **Figure 30**, the major input and output pathways are summarized for the aIC, mIC and pIC. The most striking feature of the aIC was its strong projection to the ventro-lateral striatum including NAc and CPu. In addition, it connected reciprocally with motor cortex and received less sensory information compared to mIC and pIC. Its thalamic connectivity is dominated by MD, a higher-order polymodal association nucleus of the thalamus and by CM, the main motor-output of the thalamus. Regarding the connectivity with the amygdala, it is clearly BLA biased. This aIC→BLA projection has been functionally investigated and shown to elicit appetitive behaviors⁹. The mouse – and presumably every other mammalian - brain is hard-wired in such a way, that sweet taste is represented in the territory of aIC, and thus elicits appetitive responses. There is evidence that upon changing the valence of a stimulus, e.g. after conditioned taste aversion, the representation of a previously appetitive taste shifts towards more caudal parts of the IC, closer to the “bitter spot”^{73,194} and is avoided. As the primary gustatory cortex is embedded within the insular cortex, it is hard to disentangle taste and hedonic value coding. My tracing data suggests a more general role of the aIC than a reduction to a simple “sweet cortical field”¹⁴⁸, as intra-insular projections from the mIC and pIC, which represent diverse bodily but also gustatory and olfactory information, provide a major input source. I therefore hypothesize that positively

valenced stimuli, including those that are innately appetitive, are mapped to the aIC, which is then providing a “go” signal through its down-stream projections. An open question is how aversive information routed from the pIC *via* the mIC to the aIC is processed. One possibility is that once an aversive stimulus has been detected in the pIC it prevents an appetitive response in the aIC – i.e. an antagonizing mechanism.

In contrast, the mIC received strong olfactory and facial somatosensory inputs, displayed a strong bilateral connectivity with the amygdala and showed the strongest connection to memory-related cortex (ENT, PRh, ECT). The gustatory cortex is fully embedded within what I defined as mIC and comprised of the dysgranular subdivision of my mIC definition. Indeed, recent studies demonstrated a crucial role of the mIC in conditioned taste aversion (CTA)⁷³. These findings indicate that the mIC could represent a learning hub of multiple aspects of consummatory behavior, such as taste- and texture processing of food, palatability, taste aversion or preference. Potentially, this could extend past consummatory behaviors, into social interaction, social hierarchy or mating behavior.

The connectivity of the pIC is dominated by sensory cortical regions providing somatosensory, olfactory and auditory information. Regarding subcortical connectivity, the pIC is heavily connected to the thalamus, the amygdala and the ventro-lateral striatum. Regarding thalamic innervation of the pIC, it is reciprocally connected to the ventral-posterolateral complex, including the VPM, VPMpc and the VPL. These nuclei process somatosensory information of the face and oral cavity as well as gustatory and visceral information¹⁹⁵ and project topographically organized to the mIC and pIC, specifically to the granular- and dysgranular layers of the IC¹⁵⁷. Further, the pIC is connected to the medio-dorsal nucleus of the thalamus, a higher-order nucleus that is involved in memory and cognitive tasks¹¹². Clearly, the pIC is well equipped to assess the quality and valence of tastes, but its projections to limbic structures, combined with the results of my optogenetic manipulations suggests a broader role in general aversive processing.

Interestingly, my correlation and clustering analysis indicates that the connectivity of mIC is more similar to the connectivity patterns of pIC than of those of the aIC. There are some interesting differences between mIC and pIC, however, for example, the innervation of the pBLA as discussed below.

Inhibitory interneurons across IC displayed very similar connectivity compared to excitatory pyramidal neurons. This is complemented by my correlation and hierarchical cluster analysis and is in agreement with rabies tracings performed in excitatory and inhibitory neurons of different brain regions^{113,196–198}. This high similarity of input quantities between excitatory and inhibitory neurons is not sufficient to conclude that those populations receive the same information from the same neurons. For this, one would need to perform dual monosynaptic rabies tracings from excitatory and inhibitory neurons within the same animal. Due to the leakiness of current rabies

helper-constructs and the intrinsic connectivity between excitatory and inhibitory neurons of the cortex, this would make a validation of the starter neurons impossible and the results difficult to interpret. Alternatively, one possibility would be to identify the molecular identities of input neurons, e.g. by *in-situ* hybridization or immunohistochemistry performed on input neurons, to dissect the possibility of both feed-forward inhibition and disinhibition which could arise from parallel but antagonistic circuits.

IC-amygdala Connectivity

All three subdivisions of the IC are reciprocally connected to the amygdala. While the inputs from amygdala are more uniform and seem to broadcast information, the projections from IC to the amygdala differ strongly. For example, aIC receives similar inputs compared to mIC and pIC, but it only projects to the LA and aBLA. The connectivity profiles of mIC and pIC with the amygdala shows strong similarities, however, the pIC is exclusively projecting to the pBLA and APir. A more detailed functional dissection of the IC-amygdala circuitry is required in order to better understand both, the amygdala and the insular cortex.

The pIC innervates the aBLA in a very similar manner to the mIC, however, it is also uniquely innervating the pBLA. This posterior part of the BLA has been shown to preferentially harbor neurons expressing the genetic marker *Ppp1r1b+*, which have been investigated in negative valence processing¹⁹⁹. In this study, I characterized the pIC→CeA pathway, however, an interesting target to understand pIC's role in aversive state processing might lie in the pIC→pBLA pathway.

IC-striatum Connectivity

The IC-striatum circuitry separates the IC into two parts, the aIC, which very strongly projects to the striatum, and the mIC and pIC, which innervate the striatum much weaker. As the ventral striatum is implicated in monitoring, executing and learning goal-oriented behaviors¹⁶⁸, the aIC has a prime position to modulate and drive this system. This could indicate that the aIC is indeed the major output region of the insular cortex^{40,77}.

For the mIC and pIC, I could observe the innervation of distinct striatal patches in the nucleus accumbens by IC axons (see **Figure 7b**, mIC). It would be interesting to characterize which dopamine-receptor expressing medium-spiny neurons receive insular glutamatergic innervation and where these neurons in turn project to.

Another interesting target of the insular cortex is the IPAC, which stands for interstitial nucleus of the posterior arm of the anterior commissure. All three subregions of IC densely innervate the IPAC, whose function is not well understood to date. Regarding that the IPAC shares many

connections with regions the IC also connects to, such as the CeA, BNST, LH, VPMpc, APir, it is speculated that this region is involved in autonomous control and consummatory behaviors^{200,201}.

Taken together, I here comprehensively mapped the brain-wide connectivity of three IC subdivisions spanning the entire mouse insular cortex. In this study, I confirmed that the insular meso-scale connectome of the mouse did not differ from findings obtained from rats. However, for the first time, the strength of the connections were quantitatively assessed and provided as a comprehensive resource for future studies.

3.2 Functional Characterization of pIC

3.2.1 Global pIC Manipulation

In this study, my co-workers and I revealed how the posterior part of the IC mediates aversive emotional and bodily states and exerts top-down regulation of ongoing behavior via subcortical target regions. While human imaging studies have suggested a role for the IC in processing negative emotions, such as anxiety or low mood in depression^{202,203} my study is the first, to provide a comprehensive description of neuronal circuit mechanisms that underlie diverse aversive states within the pIC using mice as a model organism. My findings underline the extent to which the pIC should be regarded as a multimodal hub.

A previous study has already shown that optogenetically stimulating pIC is avoided by mice¹⁴⁸, but the authors interpreted this as avoidance of a bitter taste sensation that has been artificially created. With the present results, I extended these findings beyond gustation. Taste is an extremely important and evolutionarily old sense that guides animals to consume non-toxic food²⁰⁴. Especially the bitter taste is a potent and innate warning signal to mammals. However, in my recent publication, my colleague Nejc Dolensek has shown with 2-photon imaging that single neurons of the pIC track not only bitter, but also other acute aversive stimuli and more importantly aversive states¹⁷¹. Thus, a bitter taste is recognized by pIC as a salient aversive stimulus that mediates a hard-wired avoidance. In addition, our findings suggest that the insula monitors visceral and facial information and pIC neurons fire upon detection of a deviant signal. How these thresholds are dynamically tuned and which roles brain-wide oscillations and brain states play are exciting open questions.

At least experimentally with optogenetics, stimulating the pIC has the capacity to entrain behavioral states, as shown with my sustained anxiety experiment (see **Figure 15**), or when I

optogenetically inhibited the insula in the closed arms of the elevated-plus maze, where it increased exploratory behavior. Already in pilot experiments, I observed an increased breathing rate and a tense body posture upon optogenetic stimulation of the pIC, which I confirmed by anaesthetized measurements (**Figure 10**). As the pIC has been implicated in sensing and modulating cardiac function^{46,49}, I was surprised to not find effects on the heart rate in anesthetized mice. A study, that could elicit tachycardia, electrically stimulated the rat pIC in a closed-loop fashion synchronized with the R wave⁴⁸. Thus, the reason why I could not measure an effect on heart rate could be due to the lack of synchronization of the optogenetic stimulation with the R wave. As derangements of insular functions, e.g. by stroke, seizure or stress, can induce cardiac arrest⁴⁶, this could explain, why an animal died after optogenetic stimulation of the pIC.

The fiber photometry measurements in the anxiety-like tasks revealed, that the pIC increases its bulk activity when the mice are in the corner of the closed arms. As reported in **Figure 11** and **Figure 12**, pIC activity increases while the animal is retreating from the open arms and then reaches its peak in the corner of the maze. In contrast, when already in the closed arm, the bulk activity would start to decrease if the animal was about to start an exploration and would reach a local minimum when finally reaching the end of an open arm. Together with the optogenetic manipulation of pIC, I conclude that the insula is a key structure in the creation and modulation of a brain-wide anxiety state.

Of note is, that some of the above mentioned conclusions dwell on a bilateral artificial activation or inhibition of hundreds or thousands of pIC pyramidal neurons via optogenetics. Obviously, this approach is crude and needs to be interpreted accordingly. It is highly likely, that we find an organized topographical representation of maybe even antagonistic processes within the pIC. Nevertheless, driving the entire pIC produces a net outcome that results in aversive reactions. As some pIC neurons still respond to sucrose, it is not solely processing negatively valenced stimuli^{30,171,205}. Yet, this was a first step to characterize the global function of the posterior insular cortex and the mixed behavioral effects I observed suggest that there are multiple different circuits and regionalized specializations within the pIC.

3.2.2 pIC-to-Central Amygdala Pathway

The aversive behaviors observed upon optogenetic stimulation of the pIC were almost fully captured by selectively activating pIC→CeA. In addition, inhibiting this projection was sufficient to reproduce the anxiolytic effects of global pIC inhibition in the real-time EPM experiment. Overall, optogenetic activation of this pathway could interrupt any ongoing behavior. It remains unclear, if this interruption is a stimulation artefact or the bona fide role of this projection. *In-vitro* electrophysiological studies have shown that IC innervates PKC- δ -, 5ht2a- and SOM-positive interneurons of the CeL^{181,182,206}, which are known to have antagonistic effects¹⁷⁶.

This suggests that there exists a further segregation of the CeA-projecting population within the IC (see **Figure 31**).

In this study, I optogenetically activated all CeL as well as CeM projecting terminals - artificially driving antagonistic circuits. The net outcome of this manipulation resulted in a general behavioural inhibition, but in order to better understand the circuit we need to be more specific in future studies, e.g. targeting only those insular neurons projecting to PKC- δ -positive neurons, which in turn project to the BNST. In addition, it would be very interesting to investigate when these CeA-projecting pIC neurons are naturally engaged, for example with projection-specific fiber photometry or 2P imaging.

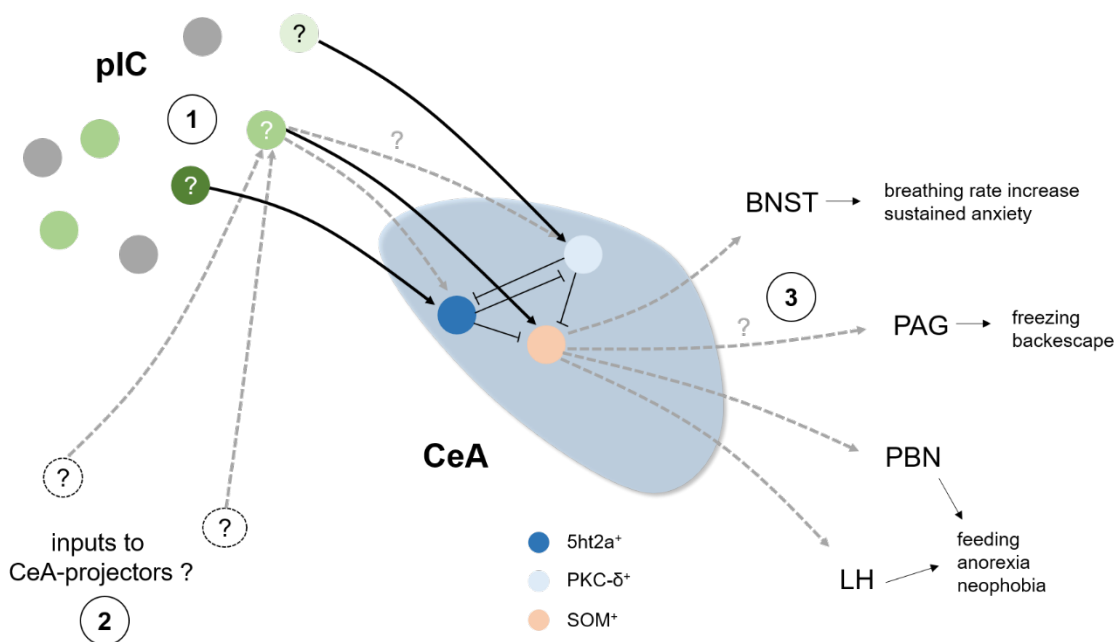


Figure 31. Open questions remaining about the IC-CeA connectivity. 1) Are there segregated IC subpopulations projecting to the distinct CeA subpopulations? 2) If so, how do these IC neurons differ in their input patterns and how does this input compare to the entire IC? 3) Is there a preferential innervation from IC to BNST, PAG, PBN or LH-projectors of the CeA?

During the course of my project, three studies were published which also investigated the pIC→CeA pathway using optogenetic manipulations. Schiff et al. investigated the role of pIC→CeA in the establishment of behavioural responding to cues, which predict appetitive or aversive tastes in a go/no-go head-fixed task. They showed that the IC–CeL pathway is necessary for establishing the learned and anticipatory responses reinforced by tastants and that activation of this pathway suppresses licking behavior²⁰⁶. However, the authors acknowledge the same challenge, namely, that there are multiple antagonistic cell-types within the CeA that are innervated by the IC. Thus, it is unclear, if the activation experiments recruit multiple functions

of this pathway. Nevertheless, this study and my findings complement each other and are in agreement, that this pathway mediates aversive information.

Two months later, Wang et al. investigated the role of two projections from the “sweet” and “bitter” cortical fields, i.e. roughly corresponding to my aIC and pIC definition, to the BLA or the CeA, respectively⁹. There, they confirmed my RTPA findings, where activation of the pIC→CeA is avoided by the mice. Further, they could show that the coupling of drinking a neutral liquid (water) with the stimulation of pIC→CeA strongly suppressed the licking responses. Then, they activated the pathway when providing the mouse with sucrose, which equally reduced the licking response of the mice. This goes hand in hand with my results and those of Schiff et al., which show that optogenetic stimulation of the entirety of pIC→CeA fibers strongly suppresses ongoing behaviors.

Shortly before we published my results in August 2019, Berret et al. investigated pIC→CeA in the context of threat learning²⁰⁷. They found a reduction of acute freezing responses upon optogenetically inhibiting pIC→CeA, but no effect on memory retrieval. Interestingly, they also describe and quantify stimulation-induced behaviors of this pathway, but at 40 Hz stimulation frequency for 10 s. In my hands, this would have certainly led to seizure-like behavior. Shockingly, shortly before I printed this thesis, it turned out, that the first author falsified the freezing data, which is very unfortunate and caused us some headache, as we were not seeing the same results. Nevertheless, all three studies are in agreement with my findings, that the posterior insular cortex plays a crucial role in evaluating aversive events. Again, all three studies including my own data face the same problem of missing specificity, that the pIC innervates multiple types of antagonistic CeA neurons. Future studies need to carefully dissect this pathway and characterize with greater specificity what the functional role of each sub population could be. This will probably uncover appetitive reactions as well, as pIC connects to the 5ht2a-positive neurons of the CeA¹⁸².

3.2.3 pIC-to-Nucleus Accumbens Core Pathway

In this study, I functionally analyzed the projection from the posterior insula to the core region of the nucleus accumbens. Optogenetic manipulation of this projection implied a role in consummatory behaviors, namely the interruption of drinking and feeding, without affecting hunger. Manipulation of this pathway did not induce avoidance in the RTPA, affect social interaction, and had no effect on breathing- or heart rate. Interestingly, inhibition of this projection could partially reverse the anorexic effects of LiCl-induced malaise. These findings provide evidence, that there is a specialized population of neurons that modify consummatory behaviors upon detection of an aversive bodily state, like visceral sickness. As the rescue from malaise-induced anorexia was not complete, it suggests that this pathway is complemented by other

circuits, which I hypothesize to be subcortical structures like the NTS, PBN, CeA, BLA and the LH— all structures, the pIC is connected to as well. Here, it would be interesting to elucidate the degree of collateralization of the NAcc-projectors with viral tracing techniques. Then, inhibition of the cell bodies of NAcc-projectors instead of the axons terminating in the NAcc, could clarify to which extent the anorexic function is mediated via these neurons. Further, better insights could be gained by measuring the physiological activity of this population, either with photo-tagged electrophysiological recordings, or with fiber photometry of retrogradely expressed GCaMP within the pIC. This would yield important information of further physiological and naturally occurring stimuli that engage this pathway.

In this study, I chose to target my optic fibers to the posterior part of the nucleus accumbens core. There is evidence that there exists a positive-to-negative valence gradient within the nucleus accumbens from anterior-to-posterior, respectively¹⁷⁹. Infusion of opioid agonists (μ -, δ -, or κ -opioid receptor antagonists) into the posterior part of the nucleus accumbens shell reduced food intake, which points to the same direction as my current findings. Therefore, it would be interesting to repeat the projection-specific experiment, but targeting a more anterior region of the nucleus accumbens and comparing the effects.

The nucleus accumbens is mainly comprised of medium-spiny GABAergic neurons (MSNs) which express either the D1- or D2-dopamine receptors. O'Connor et al. showed that activating D1-expressing MSNs of the accumbens projecting to the lateral hypothalamus can interrupt licking of sucrose¹⁸⁰, which suggests, that the effects I observed are mainly mediated through the pIC→D1R-MSN→LH circuit. Nevertheless, a rabies tracing study, that analyzed brain-wide monosynaptic inputs to D1- and D2-receptor expressing MSNs of the accumbens, showed, that D2-MSNs are also innervated by the insular cortex¹¹¹. This leads to the possibility that there exists a further separation of the NAcc-projectors in the pIC, with different functional roles.

From human imaging studies, we know that anorexic patients display an increased grey matter volume of the right pIC²⁰⁸. This could point to chronic over-activation of the pIC, including the NAcc-projector population described in this thesis. Therefore, an interesting experiment would be to chronically stimulate these neurons, e.g. by expressing the stimulating DREADD hM3q¹²⁴ and chronically supplying CNO with the drinking water. This could result in plastic changes throughout the feeding circuits and create a novel animal model of anorexia.

The IC-NAc pathway has also been studied in the context of drug addiction, focusing on the anterior insula and anterior nucleus accumbens^{37,209–212}. These studies concluded that the aIC→NAcc pathway is positively associated with drug seeking. To my knowledge, there is no study investigating the role of pIC→NAcc in addiction, but extrapolating from my findings, this pathway should have opposite function to aIC→NAcc. I speculate that the pIC→NAcc pathway is engaged when high doses of drugs start lose their pleasantness, i.e. during stimulant-induced

tachycardia and vasoconstriction. Therefore, this pathway could harbor the therapeutic potential to reduce drug-use, but also overeating.

Taken together, my results show that pIC→NAcc lacks the anxiety and aversion-related effects that I observed for pIC→CeA and can powerfully interrupt ongoing feeding and sucrose consumption without affecting the motivation to eat or drink.

3.3 Limitations of the study

Anatomy study

Although this investigation sought to systematically compare brain-wide IC connectivity, there are limitations we need to consider. Firstly, despite there being good separation between the bulk of the starter cell populations into my defined zones, there is a small proportion of overlap that may influence the connectivity. This only affects the results when comparing with mIC results, as aIC and pIC starter populations were entirely separated. Contamination into non-IC regions may also influence the results we observed, however I did not find a correlation between the amount of non-IC starter cells in a specific brain region and an increase in connectivity to its known targets (data not shown). Displaying data as percentage of total comes with the caveat that smaller regions are underrepresented, for example the dorsal raphe nucleus only provided below 0.5% of the total inputs, but consistently projected to the IC, as I confirmed *post-hoc*. Thus, functional implications cannot solely be drawn from the number of input cells. The alternative, using density analysis, underrepresents larger areas, such as cortical areas. Finally, counting labelled fiber presence after AAV infection to detect the output strength does not directly represent synaptic connectivity. Recent viral constructs coding for a fluorescent protein tagged to a synaptic marker (e.g. AAV-DIO-mRuby-T2A-synaptophysin-eGFP²¹³), or exploiting the trans-synaptic infection of AAV1-Cre²¹⁴ would overcome this limitation.

In addition, given my approach to trace from all layers of IC, I could not further differentiate finer differences of connectivity patterns of the granular, dysgranular and agranular parts of the IC. For instance, studies performed in hamsters and rats showed a further distinction of projections when comparing the dorsal and ventral division of aIC^{215–218}.

Functional study

Optogenetic excitation might engage circuits in an artificial manner, eliciting behaviors that lie outside of the naturally occurring repertoire¹²³. The 1 s ON and 4 s OFF pattern that I used for optogenetic stimulation was needed to prevent overstimulation, but it does not necessarily reflect a physiological firing pattern of pyramidal IC neurons. Different populations of the pIC might favor different modes of firing and entraining an entire brain region is poised to cause a mix of effects. In addition, one has to consider that cumulative plastic effects could be induced by subsequent stimulations. This is certainly the case for acute states lasting few minutes, but might also long-lastingly change synaptic properties (such as LTP and LTD), thus potentially modifying baseline behavior of the animals.

For the projection-specific experiments, there are two main challenges. First, it has been shown that optogenetic stimulation of axon terminals can elicit back-propagating action potentials. These then stimulate the axon-initial segment of the cell body, which in turn causes an action-potential down the axons. If the neuron sends collateral fibers to other regions, the synapse specificity of projection-specific activation might be lost or contaminated. Second, the laser light leaving the optic fiber might activate passing ChR2-positive fibers from the pIC that target thalamic or mid- and hindbrain nuclei. Thus, the observed behavioral effects could actually stem from activating those fibers rather than those terminating in CeA or NAcc.

By performing a control experiment (see 2.3.11, **Figure 29**), I could exclude that back-propagating action potentials or fibers of passage cause the observed effects of feeding interruption. It would have been interesting to also test if other behavioral effects, such as RTPP, breathing rate increases or anxiogenic effects hold true in such a control experiment, but this was out of the scope of this study.

4 MATERIALS AND METHODS

4.1 Animals

Mice between the age of 2–6 months were used in accordance with the regulations from the government of Upper Bavaria. CamKII α -Cre (B6.Cg-Tg(Camk2a-cre)T29-1Stl/J) mice were employed for both retrograde rabies tracings and anterograde axonal tracings. Retrograde rabies tracings were also performed in GAD2-Cre (Gad2tm2(cre)Zjh/J) mice. Both male and female mice were used (**Table 1**). As controls for tracings, I employed male C57Bl6\NRj mice. Male C57BL/6NRj mice were used for all optogenetic experiments. Mice that underwent behavioral testing were housed in pairs of two. All mice were kept on an inverted 12 h light/dark cycle (lights off at 11:00 am). Mice were provided with *ad libitum* access to standard chow and water except for the sucrose preference test and quinine aversion test, where mice were water-deprived for 24 h. For the feeding interruption test, the TMT test and the feeding under malaise test, mice were acutely food-swpeicws for 24 h prior to the feeding tests.

Chapter 4: Materials and Methods

CamKIIa-Cre		Distance from Bregma			Starter cell no.	Total input cells	Ratio	Gender	Hemisphere
Target site	ID	Most anterior	Median	Most posterior					
aIC	872	2.77	1.77	0.8	2278	12440	5.46	f	right
	461	2.4	2.2	1.6	1444	18080	12.50	f	right
	557	2.45	2.09	0.73	15464	31916	2.06	f	left
mIC	1323	1.7	1.21	0.85	3896	47019	12.07	m	right
	460	1.3	0.7	0.2	2921	45345	15.50	f	left
	16	1.2	0.7	0.13	2564	40514	15.80	f	right
pIC	1114	1.25	-0.6	-2.15	2591	10981	4.24	f	right
	175	0.37	-0.11	-1.43	1140	20464	17.90	f	right
	972	0.3	-0.2	-0.7	5379	10943	2.03	f	left

Gad2-Cre		Distance from Bregma [mm]			Starter cells [no.]	Total input cells [no.]	Ratio	Gender	Hemisphere
Target site	Mouse ID	Most anterior	Median	Most posterior					
aIC	1146	2.33	1.93	1.09	1672	5157	3.08	m	right
	1147	2.65	2.2	1.53	1807	14390	7.96	m	right
	1225	2.65	2.2	1.41	1847	5206	2.82	m	right
mIC	1163	1.53	0.13	-0.83	2292	18498	8.07	f	right
	1164	1	0.4	-0.35	1190	10951	9.20	f	right
	1161	1.2	0.25	-0.95	1584	25240	15.93	m	right
pIC	1162	-0.1	-0.8	-1.34	2020	16166	8.00	f	right
	1221	0.13	-0.59	-1.43	912	13316	14.60	f	right
	1224	-0.11	-0.7	-1.2	1027	6075	5.92	f	left

Table 1. Subjects of the anatomy study.

4.2 Viral constructs

For retrograde rabies and axonal AAV tracings as well as for in-vivo optogenetic experiments, the following viral constructs were obtained from the UNC Vector Core (Gene Therapy Center, University of North Carolina at Chapel Hill, USA): helper viruses for retrograde rabies tracings: AAV2/8-EF1a-FLEX-TVAmCherry (4.2x10¹² vg/ml) and AAV2/8-CA-FLEX-RG (2.5x10¹² vg/ml). For axonal AAV tracings: AAV2/5-EF1a-DIO-EYFP (5.6x10¹² vg/ml). For optogenetic experiments: AAV2/5-CaMKIIa-hChR2(H134R)-EYFP (6.2x10¹² particles/ml), AAV2/5-CaMKIIa-eNpHR3.0-EYFP (5.2x10¹² particles/ml), with AAV2/5-CaMKIIa-EYFP (4.3 x10¹² vg/ml) as control virus. For fiber photometry, AAV9.CamKII.GCaMP6s.WPRE.SV40 ($\geq 1 \times 10^{13}$ vg/mL) was obtained from Addgene (viral prep # 107790-AAV9). For DREADD experiments I used AAV8-hSyn-DIO-hM3D(Gq)-mCherry (4x10¹² GC/ml, Addgene 44361), AAV8-CaMKIIa-hM4D(Gi)-mCherry (2.64x10¹² GC/ml, Addgene 50477), and AAV2/5-CaMKIIa-EYFP (4.3 x10¹² vg/ml, UNC Vector core). For retrograde rabies tracings, I used G-deleted EnvA-pseudotyped rabies-GFP (RABV Δ G-GFP(EnvA), 3x10⁸ ffu/ml) that was kindly provided by K.K. Conzelmann (Max von Pettenkofer-Institute & Gene Center, Ludwig-Maximilians-University, Munich).

4.3 Stereotaxic surgeries

I applied metamizol (200 mg/kg, s.c.) for peri-operative analgesia and carprofen (s.c., 5 mg/kg, once daily for 3 days) for post-operative pain care. Anaesthesia was initiated with 5% isoflurane and maintained at 1-2.5% throughout the surgical procedure. Mice were firmly secured in a stereotaxic frame (Stoelting), placed on a heating pad (37 °C) and I applied eye ointment (Bepanthen, Bayer). For viral injections, I pulled glass-pipettes and attached them to a microliter syringe (5 μ L Model 75 RN, Hamilton) using a glass needle compression fitting (#55750-01, Hamilton). The syringe was then mounted onto a syringe pump, which was held by the stereotaxic frame, controlled by a microcontroller (UMP3 + micro4, WPI).

For monosynaptic retrograde rabies tracings, I first unilaterally injected 100 – 150 nl of a 6:1 (RG:TVA) mixture of helper-viruses (see viral constructs) into the aIC, mIC or pIC.

The following coordinates (given in mm from Bregma) were targeted: for anterior IC (aIC): AP: +1.9 mm, ML: + or - 2.7 mm, DV: -3.0 mm. For medial IC (mIC): AP: 0.7 mm, ML: + or - 3.7 mm, DV: -4.0 mm. For posterior IC (pIC): AP: -0.5 mm, ML: + or - 4.05 mm, DV: -4.0 mm.

I sealed the trepanation with bone wax and sutured the skin. After 3-4 weeks, 350 nl of SAD Δ G-eGFP(EnvA) were injected into the same coordinates as described above. Mice were sacrificed 7 days after infusion of the rabies virus.

For axonal AAV tracings in CamKIIa-Cre mice, AAV2/5-EF1a-DIO-eYFP (80-100 nl) was unilaterally injected into either the aIC, mIC or pIC coordinates. Mice were sacrificed four weeks after the AAV injections.

For in-vivo optogenetic experiments, I bilaterally injected 150 nl of virus at 80 nl/min into the pIC of C57BL/6NRj mice (distances from Bregma: AP: -0.45 mm, ML: \pm 4.05 mm, DV: - 4.05 mm). Then, custom made optic fibers (200 μ m core, 0.22 NA, 1.25 mm zirconia ferrule from Thorlabs) were secured with acrylic glue and dental cement 0.5 mm above the injection site.

For fiber photometry, 200 nl of AAV9-CamKIIa-GCaMP6s virus was unilaterally injected into the pIC (coordinates: AP: -0.45 mm, ML: \pm 4 mm, DV: - 4 mm) and a optic fiber (custom-made, 200 μ m, 0.48 N, glued to zirconia ferrules (2.5mm) was secured 0.2 mm above the injection site. The optic fibers were secured using acrylic glue.

For CTB double labelling within the same animals, three C57BL/6NRj mice were unilaterally injected with 150 nl of a 0.5% CTB-555 solution (in PBS) into the Central Amygdala (AP: -1.3 mm, ML: \pm 2.8 mm, DV: -4.7 mm) and 300 nl of a 0.5% CTB-488 solution into the Nucleus Accumbens core (AP: +0.9 mm, ML: 1.35 mm, DV: -4.7 mm). Mice were sacrificed 7 days after CTB injections.

For projection-specific optogenetic experiments, I bilaterally injected C57BL/6NRj mice with 150 nl of virus into the pIC as described above, but optic fibers were bilaterally implanted over the Central Amygdala (CeA) (AP: -1.3 mm, ML: \pm 2.8 mm, DV: -4.3 mm) or above the Nucleus Accumbens core (NAcc) (AP: +0.9 mm, ML: \pm 2.05, DV: -3.9 mm, 10° outward angle in the coronal plane).

For backpropagation experiments, I bilaterally injected 150 nl AAV-CamKIIa-hChR2(H134R)-EYFP into the pIC as described above and implanted opto-fluid cannulas (iOFC_M3_320/430 and DiOFC_L_ZF_2.8_320/430, Doric lenses) over the CeA (AP: -1.3 mm, ML: \pm 2.8 mm, DV: -4.0 mm, with optic insert at DV: -4.3 mm or infusion insert at DV: -4.7 mm) or NAcc (AP: +0.9 mm, ML: \pm 1.4 mm, DV: - 4.0 mm, with optic insert at DV: -4.2 mm or infusion insert at DV: - 4.6 mm).

For DREADD experiments. Mice were bilaterally injected with 200 nl of virus per hemisphere into the pIC as described above.

4.4 Histology

Animals were anesthetized with ketamine/xylazine (100 mg/kg and 20 mg/kg BW, respectively, Serumwerk Bernburg) and perfused intra-cardially with 1x PBS followed by 4% paraformaldehyde (PFA) in PBS. Brains were post-fixed for an additional 24 h in 4% PFA at 4 °C. Then, brains were embedded in agarose (3% in Water) and 70 µm coronal sections were cut with a VT1000S vibratome (Leica Biosystems). We collected all sections sequentially in single wells in 96-well plates. Every second section, ranging between approximately +2.8 to -6.2 mm from Bregma, was mounted on glass slides using a custom-made mounting medium containing Mowiol 4-88 (Roth, Germany) as described elsewhere²¹⁹ with 0.2 mg/mL DAPI (Sigma-Aldrich, MO). Images of the coronal sections were acquired with a modified epifluorescent microscope equipped with a controllable stage (Ludl) orchestrated by µManager 2.0 beta and stitched with the Grid/StitchCollection Plugin in Fiji (ImageJ). I determined the placement of the optic fibers as well as the spread of the viral infection by referencing a mouse brain atlas (Franklin & Paxinos, 4th edition⁵⁶). For the tracing studies, only animals with highly specific injections targeted at IC were included in the anatomy analysis. For optogenetics, only animals with a correct fiber placement and a viral spread confined to pIC were included in the study.

4.5 Image Processing and Data Analysis of Tracings

Starter volume detection

Both RV and AAV starter cell volumes were determined semi-automatically using CellProfiler 3.0.0²²⁰. For each image, a set of ROIs were defined for the insular cortex and adjacent regions. For RV images, rabies positive cells were detected in the eGFP image, and the corresponding cell objects masked over the mCherry (TVA) image. mCherry signal was then detected and back-related to the eGFP+ cell. The individual double-positive cells were traced through the z-stacks and related to their corresponding ROI. For AAV images, eYFP+ cells bodies were segmented and related to their corresponding ROI.

Rabies analysis

Images of coronal sections were pre-processed with the trainable Weka segmentation plugin for Fiji. The segmented GFP+ cells were quantified with a custom-written Fiji macro script. I created a collection of regions-of-interest (ROIs) for every coronal section guided by a mouse reference atlas. Rabies-positive neurons between +2.8 mm and -6.2 mm from Bregma (anterior-posterior) were counted and anatomically annotated (Figure 32). The data is reported as cell counts normalized to the total cell counts (% of total input). TVA expression can be leaky (see Do et al.,

201657; Watabe-Uchida et al., 201258), so starter cells might be confused with input cells. In control experiments that I performed (injection of AAV-FLEX-TVAmcherry and AAV-FLEX-RG followed by RABV Δ G-GFP(EnvA) into C57BL6/NRj animals and injection of AAV-FLEX-TVAmCherry followed by RABV Δ G-GFP(EnvA) into CamKII α -Cre mice), I observed a few dozen to hundred GFP⁺ cells around the injection site. No long-range inputs have been observed. As we were only interested in long-range connectivity and not in local microcircuitry of the insula, we excluded all input cells of IC and claustrum between -0.11 to -1.22 from analysis.

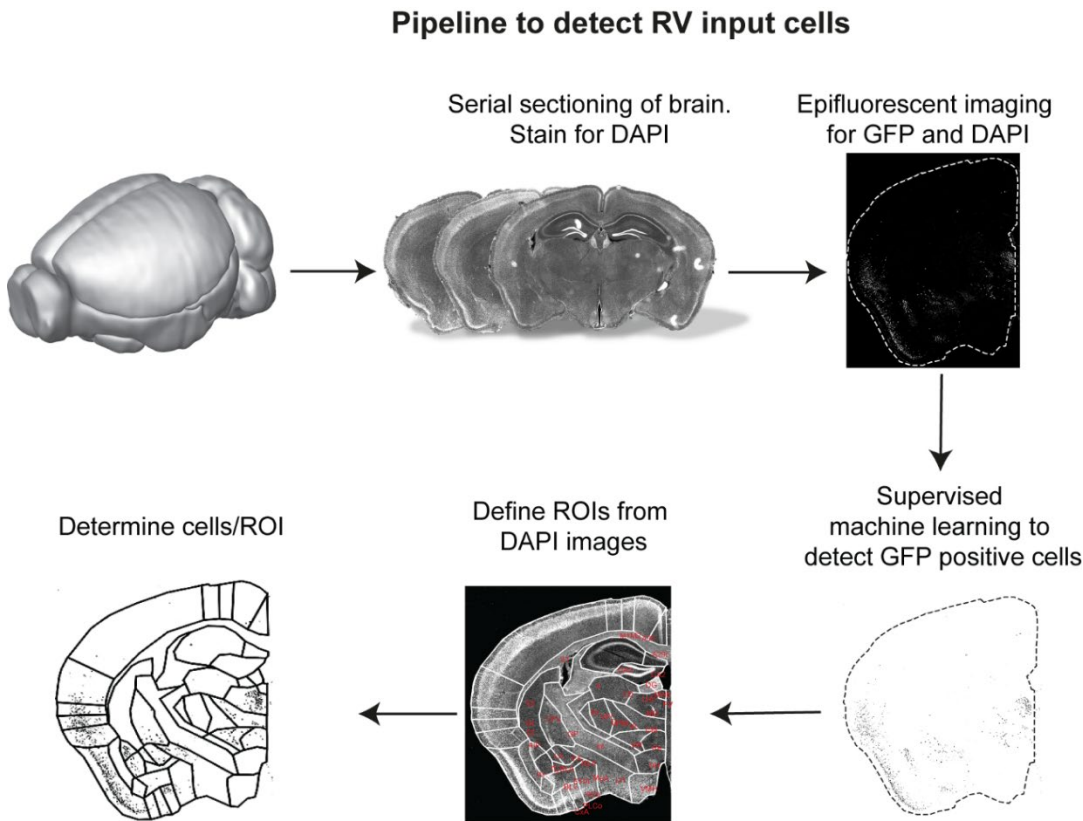


Figure 32 Whole-brain analysis pipeline to detect and register rabies⁺ input neurons. First, the perfused brain was coronally sectioned and stained with DAPI. Next, epifluorescent images were acquired in the DAPI and GFP channel. The resulting images of single coronal sections were pre-processed and binarized with a supervised machine learning algorithm. This binarized image was quantified, based on regions of interest (ROIs) that were manually drawn on the DAPI channel to match the Paxinos mouse brain atlas.

Axonal AAV tracing analysis

Coronal sections of axonal AAV tracings were acquired on a Leica SP5 confocal microscope. For each brain, I first visually determined the densest efferents outside insular cortex (usually VPMpc or Fundus of Striatum (IPAC)), and adjusted the acquisition settings to obtain a nearly saturated signal for this region. I acquired a single optical z-section of 10 μ m thickness and positioned it in the middle of the coronal slice (z-axis). Every second brain section from +2.8 to -6.2 mm from

Bregma was acquired. Images were pre-processed with a hessian ridge detection as described elsewhere²²¹. Briefly, this results in binarized images of the eYFP+ axons while eliminating background fluorescence. These binarized images were quantified with Fiji Macro script that I produced. Similar to the rabies quantification, I used my custom-made ROI atlas synthesized from a mouse brain reference atlas and manually adjusted the ROIs for every coronal section (**Figure 33**). I obtained area of the ROIs and the total pixel count per ROI. The Data is reported as “percent of total output”, which is the pixel count of a ROI normalized to the sum of all pixels identified to belong to axons. Additionally, I calculated the “percent innervation density”, which is the proportion of pixels covering the total area of a ROI, averaged across all sections, on which this ROI is present. I excluded passing fiber bundles (striatum, cerebral peduncles, anterior commissure, internal- and external capsules, pyramidal tract) from the analysis.

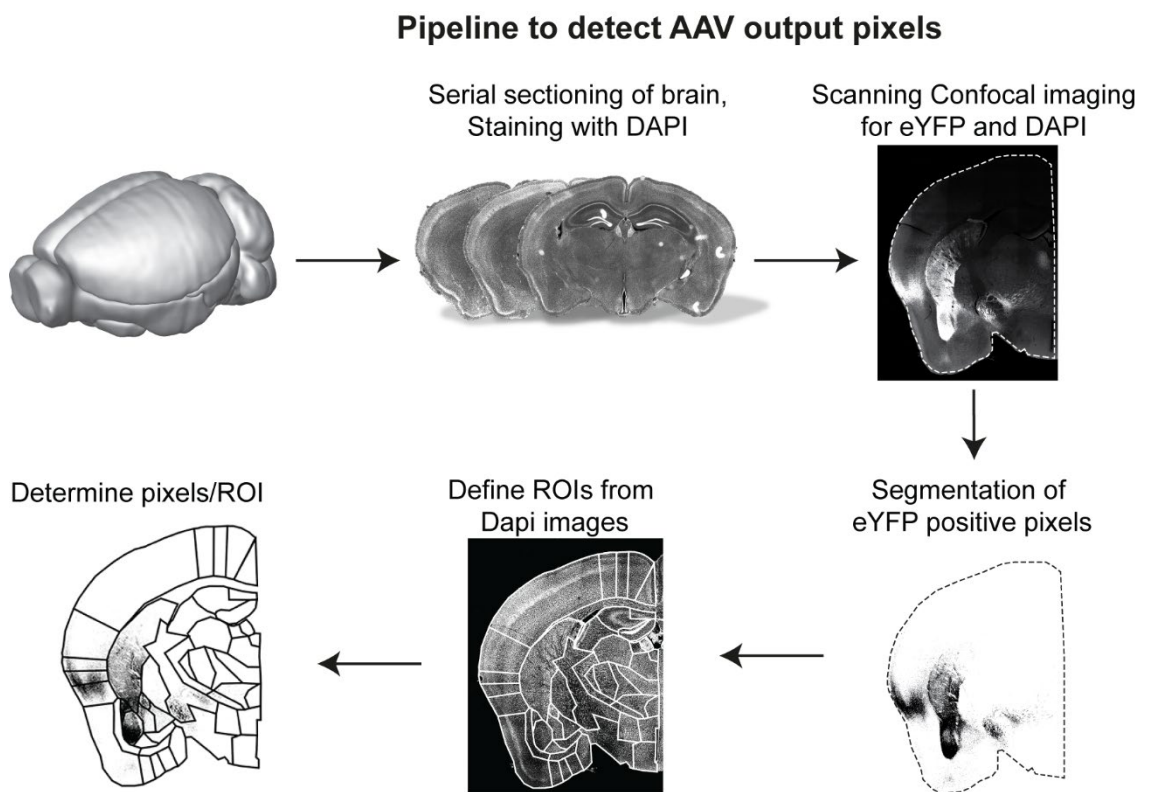


Figure 33. Whole-brain analysis pipeline for AAV axonal tracings. First, the perfused brain was coronally sectioned (50 μm) and stained with DAPI. Next, a single 10 μm thick (z-axis) confocal image was acquired from the middle of the section (z-axis). Then, eYFP positive pixels were segmented with a hessian ridge-detection algorithm. These pixels were quantified in the same way as the rabies tracings.

CTB double labelling analysis

Images of coronal sections were acquired with an epifluorescent slide scanner, as described above. CTB positive cells were segmented using the trainable WEKA plugin as described for the rabies analysis, with separate classifiers for the 488 nm and 555 nm signal. I quantified the cell counts within the rostro-caudal extent of the insular cortex (AP: +2.45 mm to - 1.22 mm) using the same custom-written Fiji script as for the rabies analysis. Double-labelled cells were manually quantified with the Fiji cell counter plugin.

4.6 Heart- and Breathing Rate Measurements in Anaesthetized Mice

Anesthesia was initiated with 5% isoflurane and maintained at 1-1.5% during experiments. Mice were placed in a stereotaxic frame and heart rate and breathing rate were recorded with a MouseOx Plus oximeter (s-collar clip, shaved neck, Starr life sciences) while delivering bilateral optogenetic manipulations. For ChR2 expressing animals, this consisted of a 30 s baseline, followed by a 20 s stimulation epoch of 5, 10 or 20 Hz, 473 nm, 3-5 mW, 5 ms pulse width. Different frequencies were tested within the same animal after a 2 min break. For NpHR animals, we recorded a 30 s baseline, followed by a 2 min constant delivery of 593 nm light (12 mW). Z-scores were calculated using the mean and SD from the first 20 s of the baseline recording.

4.7 Behavioral Tests

All mice were handled by the experimenters and habituated to tethering of the fiber optic patch cords for at least three days. All behavioral experiments were performed during the dark phase of the light cycle between 12:00 and 20:30.

Stimulation-evoked behaviors

Optogenetics: Animals were tethered to optic patch cords and placed in a behavioral arena (20x50x30 cm) with transparent plexiglas walls and recorded with a CMOS camera at 100 fps (DMK 33UP1300, Imaging Source). Laser stimulation was manually triggered by the experimenter at random intervals or when behavioral reactions had subsided during the 5 min test (473nm, 1 s, 20 Hz, 5 ms pulse width, 3-5 mW, minimum ISI = 4 s). The experiment was terminated prematurely if we observed severe reactions like jumping or crouching. Stimulation-evoked behaviors were manually scored. DREADDs: Mice bilaterally expressing the excitatory DREADD-receptor hM3Dq or eYFP in the pIC were injected with clozapine-N-oxide (CNO, 10 mg/kg, i.p.) and after 40 min they were placed into a circular open field arena. The mice were

video recorded for 15 min. Stimulation induced behaviors were scored manually by a human observer inspecting the videos post-hoc and blinded to the underlying condition.

Real-time place avoidance (RTPA)

The RTPA assay was performed on three consecutive days in custom-built chambers (50x40x25 cm, transparent plexiglas, distinct metal floor grids, distinct visual patterns presented in chambers). We tracked the mice with a webcam (c930e, Logitech) that was interfaced with custom-written MATLAB software. The first day, mice were tracked for 20 min to establish their preferred chamber. The following day, the preferred chamber became the “stimulated chamber”. The trial started in the non-stimulated chamber and lasted 20 min. Crossing into the stimulated chamber resulted in delivery of light of 473 nm (at either 10 Hz, 3-5mW (pIC-ChR2 and pIC-CeA), or 20 Hz, 7-10mW (pIC-NAcc); all with a 5 ms pulse width, 1 s Laser on followed by 4 s ISI). For NpHR animals we applied 594 nm constant illumination at 12 mW. Exiting the stimulated chamber immediately switched off the laser. On day 3, we tested if the mice displayed an association with the stimulated chamber (no laser).

Real-time control of pIC activity during Elevated-Plus Maze (EPM) exploration in a high anxiety setting

The custom-build EPM had the following dimensions: 5 cm wide arms, each arm was 35 cm long, 5 mm ridge on open arms to prevent falls, closed walls 15 cm high, maze was elevated 60 cm from the floor. The EPM was performed for 10 min in a room the animals had never been exposed to. The mice were minimally handled (3 days with tethering to optic fibers). We illuminated the center of the EPM with 450 lux. The environment was noisy due to a cooling fan. We used ANYmaze to track mice in real-time and subsequently trigger optogenetic manipulation based on the location of the animals. Guided by our fiber photometry data (Fig 2 a and b), we inhibited the pIC or its projections to CeA and NAcc when the animal was located in the closed arms of the EPM, but not on the open arms. In contrast, we optogenetically stimulated the pIC or its projections to CeA and NAcc in the open arms of the EPM, but not in the closed arms. The stimulation parameters were set to 10 Hz, 3-5 mW (pIC-ChR2 and pIC-CeA), or 20 Hz and 7-10 mW (pIC-NAcc), all with a 5 ms pulse width, 1 s laser on, 4 s ISI). NpHR animals were subjected to 594 nm constant illumination at 12 mW.

Real-time control of pIC activity during Elevated-Zero Maze (EZM) exploration in a low anxiety environment

The custom-build EZM had the following dimensions: diameter of 55 cm, 5 cm wide, 5 mm ridge on the open arms to prevent falls, 20 cm high closed walls, maze elevated 60 cm from the floor. To create low anxiety settings, we performed the task on well-handled mice (~ 6-7 days) in a quiet and dimly lit room (6 lux on the open arms) that the animals were habituated to. We used

ANYmaze to track mice in real-time and subsequently trigger optogenetic manipulation based on the location of the animals, as described above for the real-time optogenetic control in the EPM.

Optogenetic stimulation followed by EPM

pIC-ChR2 or -eYFP controls were optogenetically stimulated for 50 s in an open field arena with 20 Hz, 5 ms pulse width, 3-5 mW. After 1 min recovery, animals were disconnected from the optical patch cord and subsequently tested for 8 min on the EPM. We placed mice in the center zone of the EPM facing a closed arm.

Attenuation of sustained anxiety

To induce an anxiety state, animals were placed in behavior boxes (Ugo Basile, Italy) consisting of a metal grid floor and plexiglas walls with distinct visual cues. The floor and walls were cleaned with 80% ethanol before and after each session. Freezing behavior was scored using ANYmaze. The animals were considered to be freezing if no movement except for breathing was detected for at least 2 s. Animals were tethered to optic patch cords, placed in the fear conditioning box and we administered five unsignaled shocks (1 s, 0.4 mA) through a metal grid floor over a 20 min time period with an ISI of 160 - 290 sec. Optogenetic inhibition (594 nm, 12 mW) was delivered during the entire 20 min. Then, mice were detached from the optic patch cords and placed in the center zone of the EPM facing the closed arms and tested for 8 min. For testing contextual fear memory recall, animals were placed in the same behavior boxes for 15 min 7 days after fear conditioning and freezing behavior was analyzed during the whole session.

Ramping Hot Plate Test

The temperature of the plate started at 32 °C and was ramped up by 1 °C per 4 s. The test was stopped and the temperature recorded, as soon as the mice licked their paws. pIC-NpHR mice were tethered to optic patch cords and habituated to the hot plate apparatus (Hot Cold Plate Analgesia Meter for Mice and Rats, Campden Instruments) for a maximum of 5 min. Each animal was tested a total of twelve times (6x light ON, 6x light OFF) on two separate days. Values are presented as the average of these twelve repeats.

Sucrose preference test / quinine avoidance test

24 h-water-deprived mice were trained for 30 min daily over 5 days to consume either a sucrose-solution, or water only, from two sipper tubes presented in a custom-built chamber (30x50x30 cm) until they reached a stable preference for sucrose. Since comparable sucrose preference assays used sucrose concentrations of 1-10% (Tye et al., 201351; Labouèbe et al., 201652), we chose a medium sucrose concentration range of 5%. The sucrose preference index was calculated as: (sucrose licks - water licks) / (sucrose licks + water licks). The location of the sucrose solution and water alternated daily and licks were recorded via a custom-built lickometer that was

interfaced with MATLAB. On test days, we delivered an open-loop stimulation pattern of 1 s laser-on with a 4 s ISI for 20 min. pIC-CeA animals were tested with 10 Hz on separate days, pIC-NAcc animals were tested with 20 Hz. For NpHR expressing mice, we delivered constant illumination (12 mW) for 20 min. For the quinine avoidance test, we first established a stable avoidance of quinine (0.5 mM in water) for three consecutive days. Then, on test days, we performed optogenetic manipulations as described above. Quinine preference index was calculated as (quinine licks - water licks) / (quinine licks + water licks). For analysis of the bout length, we grouped licks into a bout if the next inter-lick-interval was larger than 0.3 s.

Closed-loop sucrose licking test

ChR2-expressing pIC→NAcc mice that have undergone the ‘open-loop’ sucrose preference test (see above) were subjected to a closed-loop licking assay. The experiment was performed in the same chambers as described above; however, the setup was modified in such a way, that a detected lick would trigger optogenetic stimulation. The stimulation lasted a second and was followed by a four-second time-out period in which further licks would not elicit optogenetic stimulation. Three different frequencies were subsequently tested for three rounds with each lasting 5 min, starting with a no stimulation control, followed by 5, 10 and 20 Hz. The laserpower was set to 3-5 mW (473 nm)

Feeding under closed-loop optogenetic stimulation

We habituated acutely food-deprived (24 h) mice to the behavioral chamber (20x50x30 cm) for 5 min. Then, a standard chow pellet was secured to the floor with double-sided tape. We observed the behavior and manually triggered laser stimulation once the mouse started nibbling on the food pellet. This led to a laser stimulation of 1 s, 473 nm, 10 or 20 Hz, 5 ms pulse width, 7-10 mW measured at the tip of the fiber. The experimenter stimulated every attempt to feed (no 4 s ISI). The trial was recorded for 5 min at 100 fps and manually scored with ANYmaze. A successful interruption was scored if laser stimulation could stop chewing/eating for at least 1 s. Food intake was measured by weighing the food pellets and crumbles with precision fine scales before and after the trial.

Feeding under malaise

First, we tested if inhibition of the pIC-CeA or pIC-NAcc pathways for 20 min (594 nm, 10-12 mW) influenced feeding in acutely food-deprived mice. After a day of refeeding, mice were again food deprived for 24 h and i.p. injected with a lithium chloride solution (0.3M in 0.9 % saline, 1.2 % body weight = e.g. 350 μ l / 30 g mouse) 30 min prior to the test. Terminals of the pIC-CeA or pIC-NAcc pathway were inhibited for 20 min (594 nm, 10-12 mW at the tip of the fiber) in the

presence of a standard chow pellet. The weights of the pellet before and after the test were measured with precision fine scales.

Social approach test

Mice were habituated for 5 min to a custom-built chamber (30x50x30 cm) containing an empty cylindrical cage. After habituation, male juvenile C57BL/6NRj mice were placed inside the cylinder cage for 5 min. Every social interaction resulted in a 1 s laser stimulation (parameters as above, no ISI) manually triggered by an experimenter. Close-up videos of the interactions were manually scored with ANYmaze.

Feeding under anxiety

First, we tested whether inhibition of pIC without the presence of TMT would affect feeding in food-deprived mice. Animals were tethered to optic patch cords and habituated to an empty cage for 5 min, after which we placed a standard food pellet and a 2.5 cm plastic petri-dish with saline soaked filter paper into one side of the cage. We constantly illuminated the pIC with 594 nm light (12 mW) for 10 min and recorded the behavior from the top and from the side. Following this control experiment, we repeated the test, but this time, we soaked the filter paper with 7 μ l of a 90 % 2,3,5-Trimethyl-3-thiazoline (TMT) solution (BioSRQ). Again, pIC was inhibited by delivering 594 nm laser light as described above. After each test run, we ventilated the behavioral room for 5-10 min with a rotating fan and opened lab doors. Videos from the side manually scored for flat-back approaches, rearing and grooming events by an observer blind to the experimental conditions.

Frequency dependent locomotion response

We connected the animals to the optic patch cords and placed them in an open arena (50x25x25 cm). After a 1 min acclimatization, mice received 5, 10 or 20 Hz optogenetic stimulation (473 nm, 1 s ON, 4 s OFF, 3-5 mW) for 30 s with a 2 min break when switching the stimulation frequency. Locomotion parameters were analyzed with ANYmaze.

Backpropagation control experiments

To test if the behavioral effects induced by stimulation of pIC terminals over the CeA and NAcc were indeed mediated by monosynaptic, glutamatergic inputs from the pIC to the CeA or NAcc rather than axons of passage or antidromic activation of pIC somata, we performed the following control experiment adapted from a previous report (Felix-Ortiz et al., 201353).

We bilaterally implanted opto-fluid cannulas (see section, ‘Surgeries’) over either CeA or NAcc in mice, which expressed Chr2 for 6 weeks in their pICs (for coordinates and cannulas see

section, ‘Surgeries’). First, we tested if interruption of ongoing feeding upon stimulation of the CeA or NAcc pathway could be reproduced. We guided the optic inserts (supplier DORIC lenses; for CeA: OI_iOFC-M3_200/240_0.22_FLT_4.3, for NAcc: OI_DiOFC-L-ZF_200/240_0.22_FLT_4.2) through the opto-fluid cannulae, connected mice to optic patch cords and performed the feeding under closed-loop optogenetic stimulation experiment, as described above. Every attempt to feed led to a 1 s laser stimulation (473 nm, 5 ms, 3-5 mW, 10 Hz (CeA) or 20 Hz (NAcc), no ISI). To assess effects within the same individuals, after 24 h of refeeding, we again food deprived the mice for 24 h. We then repeated the feeding under closed-loop optogenetic stimulation. This time, 1-1.5 h before testing, animals were briefly anaesthetized and 300 nl of the AMPA receptor antagonist NBQX (NBQX disodium salt, Enzo Life Sciences GmbH, Germany; 5 mg/ml in sterile 0.9 % Saline) were infused through the fluid inserts (supplier Doric lenses; for CeA: FI_iOFC-M3_100/170_4.7; for NAcc: FI_DiOFC-L-ZF_100/170_4.6). For infusions, we connected the fluid inserts to a 5 μ l microsyringe (Model 75 RN, Hamilton, USA) using PE tubing and inserted them into the implanted guide cannulae. The flow rate (150 nl/min) was controlled by a syringe pump (UMP3 pump with a sys-micro4 controller, WPI, USA).

Anxiety-like behavior under DREADD-mediated pIC manipulations

Six weeks after bilateral injection of virus (hM4Di or EYFP control) into the pIC, mice were habituated to being injected i.p. for 3 consecutive days with 300 μ l 0.9 % saline solution. On the day of the experiment, 10 mg/kg Clozapine-N-oxide solution (CNO, in sterile saline with a final DMSO concentration of 2.5%, Sigma, #C0832) was injected intraperitoneally 30-40 min before testing. Mice were then placed onto the center of a circular open field maze and observed for 15 min. Behavior in the maze was recorded for 15 min and anxiety-like behavioral parameters were quantified afterwards using ANYmaze 6.0 (Stoelting) software.

4.8 Fiber photometry

Fiber photometry during elevated-plus maze (EPM) and elevated zero maze (EZM). Animals were handled for at least three days and habituated to being tethered. On the day of the experiments, mice were tethered to optic patch cords (low auto fluorescence fibers, NA 0.48, Doric) and connected to the fiber photometry setup via a rotary-joint. After 3 min of acclimatization in their home cage, the animals were tested for 15 min on the EZM or EPM. Videos of the behaving animals were acquired and analyzed using ANYmaze 6.0 (Stoelting) and synchronized to photometry data using TTL pulses.

Photometric signal acquisition and analysis. As described previously (Lerner et al. 201554), we used GCaMP6s bulk fluorescence measurements through a single optical fiber (custom made, 200 μm diameter, 0.48 NA) for both delivery of excitation light and collection of emitted fluorescence. For both, excitation and emission measurements, we used a commercial fiber photometry system (1-site 2-color, Doric Lenses Inc., Canada) with two excitation wavelengths, 405 nm (isobestic point of the GCaMP signal, calcium-independent) and 465 nm (GCaMP signal, calcium-dependent). The two excitation LEDs were fiber coupled into patch cords. Excitation light intensity was measured at the end of these patch cords as $\sim 20 \mu\text{W}$ for 465 nm and $\sim 7 \mu\text{W}$ for 405 nm light. Patch cords were coupled to the implanted optic fibers before the behavior experiments. Implanted fibers were tested before implantation to transmit $\geq 80\%$ of the incoming light.

Photometry signals were recorded at 12 kHz, demodulated, and down sampled to 30 Hz for analysis. All photometry data were analyzed using custom-written MATLAB (Mathworks) programs. In order to remove the strongest photobleaching artifacts, we excluded the first 30 seconds of each recording. To remove bleaching and motion artefacts, a least-squares linear fit was applied to the 405 nm control signal and aligned to the 465 nm signal, using a procedure developed by Lerner et al.: <https://github.com/talialerner/Photometry-Analysis-Shared/blob/master/Dropbox/MATLAB/Shared%20photometry%20code/controlFit.m>

The fluorescent change ($\Delta F/F$) was calculated as:

$$\Delta F/F = (465 \text{ nm signal} - \text{fitted } 405 \text{ nm signal}) / \text{fitted } 405 \text{ nm signal}$$

For the correlation analysis, we built z scores using the mean and standard deviation calculated across the entire behavioral session to make comparisons between animals feasible. We then computed the AUC of the z scores for times spent either in the open or closed arms and plotted them on the y-axes.

Approach / Retreat analysis

For the EPM, we defined an approach as movement from the corner of a closed arm towards the open arm. Conversely, a retreat was defined as movement from the open arms towards the corner of a closed arm (Figure 34). Additionally, we also considered movement from the corner of a closed arm towards the center as an approach, even when the mouse did not enter an open arm. In order to define approach and avoidance on the EZM, the position of the animal was transformed from Cartesian coordinates to angular displacement ($-\sin 2\theta$). The position of the animal (θ) was computed from the dot product of the two vectors, namely, the vector between center of EZM to the starting point which was defined as one closed and open arm transition (0a in Figure 3b), and the vector between the center of EZM to the position of the animal on EZM. The position(θ) was

then converted to $-\sin 2\theta$, so that when the animal was at the borders between open and closed arms, it's angular displacement is 0, negative when in the open arms, and positive when in the closed arms. The angular displacement was at its maximum of 1 when the animal was at the extremes of the closed arm and (-1) when it was most exposed on the open arm. Approaches and retreats were in both cases manually annotated.

To calculate the change of $\Delta F/F$ as plotted in **Figure 11**, we first annotated approaches and retreats manually. Approaches were only considered if they started at the end of the closed arm. Retreats were any movements leaving the open arm. We first calculated the mean derivative of $\Delta F/F$ for each approach and retreat for each animal. We then averaged all approaches and retreats made by a single animal to plot them as shown in **Figure 11**.

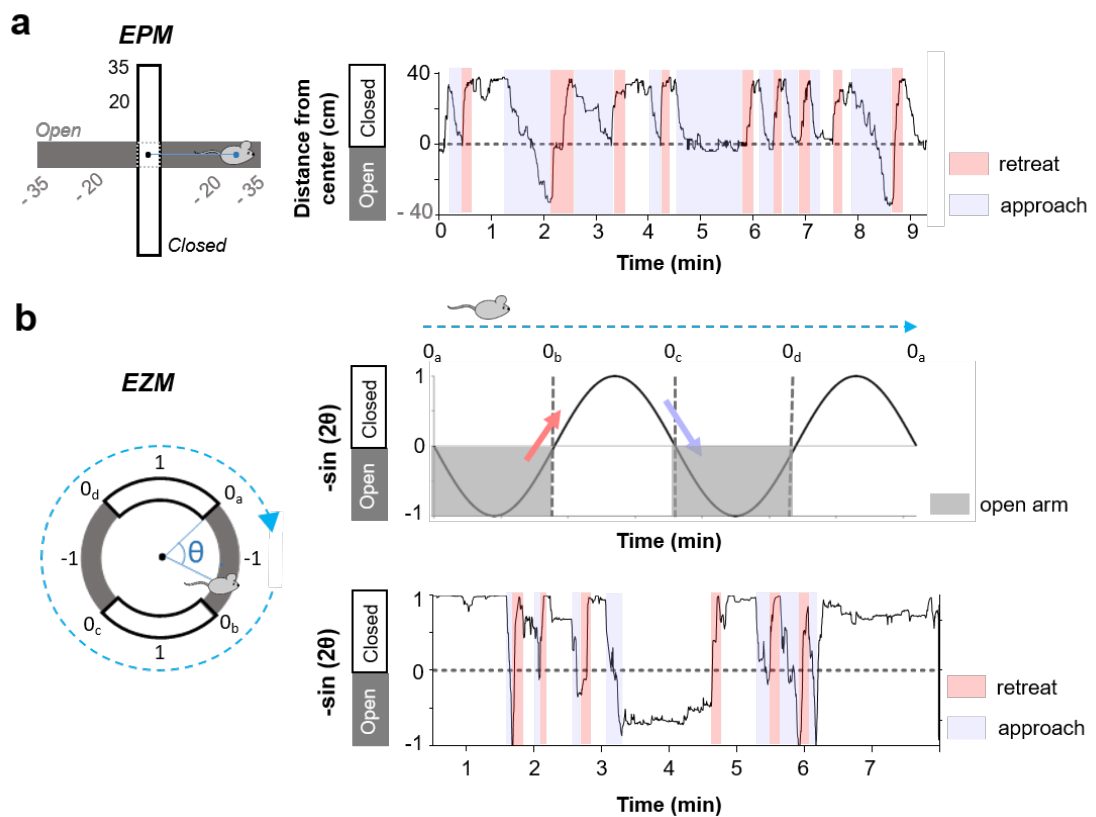


Figure 34. Definition of Approach or Retreat behavior of mice on the EPM or EZM. Panels a) and b) are adapted from my publication¹⁷¹ as permitted by the author reuse rights of Nature Springer.

4.9 Statistical analysis

Analyses were performed using either Gaphpad Prism (GraphPad Software, Inc., La Jolla, CA, USA, Version 8), MATLAB (Mathworks, Natick, MA, USA) or Python. Group comparisons were made using either one-way or two-way analysis of variance (ANOVA) followed by Bonferroni post hoc tests if a significant main effect or interaction was observed ($p < 0.05$). Single variable comparisons were made with two-tailed unpaired or paired t tests. Correlation analyses were made using linear regression. All animal numbers are reported in Figures and their legends. No statistical methods were used to predetermine sample size.

LIST OF FIGURES

FIGURE 1. SCHEMATIC OF CELL-TYPE SPECIFIC MONOSYNAPTIC RABIES TRACING	9
FIGURE 2. CHARACTERIZATION OF STARTER NEURONS FOR RV OR AAV TRACINGS.	18
FIGURE 3. WHOLE-BRAIN INPUT AND OUTPUT MAP OF THE MOUSE INSULAR CORTEX.	19
FIGURE 4. HIERARCHICAL CLUSTERING SEPARATES AIC FROM MIC AND PIC FOR INPUTS AS WELL AS OUTPUTS	21
FIGURE 5. INSULA-AMYGDALA CONNECTIVITY	23
FIGURE 6. QUANTIFICATION OF INSULA-AMYGDALA CONNECTIVITY	24
FIGURE 7. INSULA-STRIATUM CONNECTIVITY	26
FIGURE 8. BILATERAL OPTOGENETIC STIMULATION OF PIC ELICITS VARIOUS STIMULATION-INDUCED BEHAVIORS	28
FIGURE 9: REAL-TIME PLACE PREFERENCE TEST REVEALED THAT BILATERAL OPTOGENETIC PIC-ACTIVATION IS AVERSIVE..	29
FIGURE 10. BILATERAL OPTOGENETIC MANIPULATION OF PIC INCREASED BREATHING- BUT NOT HEART RATE IN ANAESTHETIZED MICE	31
FIGURE 11. BULK CALCIUM IMAGING OF PIC DURING ANXIETY-RELATED TESTS REVEALED INCREASED ACTIVITY IN THE CLOSED ARMS WHEREAS OPEN ARM VISITS SHOWED REDUCED ACTIVITY	33
FIGURE 12. PIC ACTIVITY IS CORRELATED WITH APPROACHES AND RETREATS TO AND FROM THE OPEN ARM OF ANXIETY-RELATED TESTS	34
FIGURE 13. REAL-TIME OPTOGENETIC MANIPULATION EXERTS BI-DIRECTIONAL INFLUENCE ON ANXIETY-LIKE BEHAVIOR	36
FIGURE 14. COMPLEMENTARY ANXIETY-RELATED EXPERIMENTS THAT SUPPORT A ROLE OF THE PIC IN ANXIETY STATES	37
FIGURE 15 THE PIC MEDIATES PERSISTENT ANXIETY	39
FIGURE 16 LARGELY NON-OVERLAPPING PIC NEURONAL SUBPOPULATIONS PROJECT TO THE CEA AND NACC	42
FIGURE 17 STIMULATION-INDUCED BEHAVIORS OF PIC→CEA OR PIC→NACC.	45
FIGURE 18. OPTOGENETIC STIMULATION AT 20 HZ CAUSES INCREASED IMMOBILITY FOR PIC→CEA, BUT NOT FOR PIC→NACC	46

FIGURE 19. STIMULATION OF THE PIC→CEA PATHWAY ELICITS AVOIDANCE, WHEREAS PIC→NACC STIMULATION HAS NO EFFECTS	47
FIGURE 20. OPTOGENETIC STIMULATION OF PIC→CEA INCREASES THE BREATHING RATE OF ANAESTHETIZED MICE	48
FIGURE 21. REAL-TIME OPTOGENETIC MANIPULATION OF PIC→CEA BI-DIRECTIONALLY INFLUENCES ANXIETY-LIKE BEHAVIOR. ASSESSMENT OF PATHWAY-SPECIFIC OPTOGENETICS ON ANXIETY	50
FIGURE 22. OPTOGENETIC MANIPULATION OF BOTH PATHWAYS DOES NOT INFLUENCE INNATE SUCROSE PREFERENCE, BUT LASER INTERRUPTS ONGOING LICKING	52
FIGURE 23. CLOSED-LOOP OPTOGENETIC STIMULATION OF LICKING BEHAVIOR INTERRUPTS LICKING IN PIC→NACC MICE IN A FREQUENCY-DEPENDENT MANNER	53
FIGURE 24. OPTOGENETIC STIMULATION OF BOTH PATHWAYS POWERFULLY PREVENTS FOOD-DEPRIVED MICE FROM FEEDING	54
FIGURE 25. QUININE AVERSION IS NOT AFFECTED BY OPTOGENETIC MANIPULATION OF PIC→CEA OR PIC→NACC	55
FIGURE 26. OPTOGENETIC STIMULATION OF PIC→CEA BUT NOT PIC→NACC INTERRUPTS ONGOING SOCIAL INTERACTION	56
FIGURE 27. INHIBITION OF PIC→NACC PARTIALLY RESCUES LiCl-INDUCED ANOREXIA	57
FIGURE 28. ANXIETY-MEDIATED ANOREXIA IS SLIGHTLY AMELIORATED BY PIC→CEA INHIBITION.	59
FIGURE 29. CONTROL EXPERIMENT SHOWS THAT BACK-PROPAGATING ACTION-POTENTIALS DO NOT CAUSE FEEDING INTERRUPTION	61
FIGURE 30. BIG PICTURE CONNECTIVITY MAP OF AIC, MIC AND PIC WITH KEY BRAIN STRUCTURES.	63
FIGURE 31. OPEN QUESTIONS REMAINING ABOUT THE IC-CEA CONNECTIVITY	68
FIGURE 32. WHOLE-BRAIN ANALYSIS PIPELINE TO DETECT AND REGISTER RABIES ⁺ INPUT NEURONS	78
FIGURE 33. WHOLE-BRAIN ANALYSIS PIPELINE FOR AAV AXONAL TRACINGS	79
FIGURE 34. DEFINITION OF APPROACH OR RETREAT BEHAVIOR OF MICE ON THE EPM OR EZM.	87

5 REFERENCES

1. Lovett-Barron, M. *et al.* Ancestral Circuits for the Coordinated Modulation of Brain State. *Cell* **171**, 1411-1423.e17 (2017).
2. Zelikowsky, M. *et al.* The Neuropeptide Tac2 Controls a Distributed Brain State Induced by Chronic Social Isolation Stress. *Cell* **173**, 1265-1279.e19 (2018).
3. Baliki, M. N. & Apkarian, A. V. Nociception, Pain, Negative Moods, and Behavior Selection. *Neuron* **87**, 474–491 (2015).
4. Contreras, M., Ceric, F. & Torrealba, F. Inactivation of the interoceptive insula disrupts drug craving and malaise induced by lithium. *Science* **318**, 655–8 (2007).
5. Kurth, F., Zilles, K., Fox, P. T., Laird, A. R. & Eickhoff, S. B. A link between the systems: functional differentiation and integration within the human insula revealed by meta-analysis. *Brain Struct. Funct.* **214**, 519–34 (2010).
6. Critchley, H. D., Wiens, S., Rotshtein, P., Öhman, A. & Dolan, R. J. Neural systems supporting interoceptive awareness. *Nat. Neurosci.* **7**, 189–195 (2004).
7. Craig, A. D. Interoception: The sense of the physiological condition of the body. *Curr. Opin. Neurobiol.* **13**, 500–505 (2003).
8. Simmons, W. K. *et al.* Keeping the body in mind: Insula functional organization and functional connectivity integrate interoceptive, exteroceptive, and emotional awareness. *Hum. Brain Mapp.* **34**, 2944–2958 (2013).
9. Wang, L. *et al.* The coding of valence and identity in the mammalian taste system. *Nature* **558**, 127–131 (2018).
10. Singer, T., Critchley, H. D. & Preuschoff, K. A common role of insula in feelings, empathy and uncertainty. *Trends Cogn. Sci.* **13**, 334–340 (2009).

11. Shi, C. J. & Cassell, M. D. Cortical, thalamic, and amygdaloid connections of the anterior and posterior insular cortices. *J. Comp. Neurol.* **399**, 440–68 (1998).
12. Van De Werd, H. J. J. M., Rajkowska, G., Evers, P. & Uylings, H. B. M. Cytoarchitectonic and chemoarchitectonic characterization of the prefrontal cortical areas in the mouse. *Brain Struct. Funct.* **214**, 339–53 (2010).
13. Allen, G. V., Saper, C. B., Hurley, K. M. & Cechetto, D. F. Organization of visceral and limbic connections in the insular cortex of the rat. *J. Comp. Neurol.* **311**, 1–16 (1991).
14. Cechetto, D. F. & Saper, C. B. Evidence for a viscerotopic sensory representation in the cortex and thalamus in the rat. *J. Comp. Neurol.* **262**, 27–45 (1987).
15. Mikula, S., Trotts, I., Stone, J. M. & Jones, E. G. Internet-enabled high-resolution brain mapping and virtual microscopy. *Neuroimage* **35**, 9–15 (2007).
16. Kutlu, M. G. *et al.* Role of insular cortex D₁ and D₂ dopamine receptors in nicotine self-administration in rats. *Behav. Brain Res.* **256**, 273–8 (2013).
17. Miranda, M. I., Sabath, E., Nuñez-Jaramillo, L. & Purón-Sierra, L. β -Adrenergic receptors in the insular cortex are differentially involved in aversive vs. incidental context memory formation. *Learn. Mem.* **18**, 502–507 (2011).
18. Heng, L., Beverley, J. A., Steiner, H. & Tseng, K. Y. Differential developmental trajectories for CB1 cannabinoid receptor expression in limbic/associative and sensorimotor cortical areas. *Synapse* **65**, 278–286 (2011).
19. Santana, N., Bortolozzi, A., Serrats, J., Mengod, G. & Artigas, F. Expression of Serotonin 1A and Serotonin 2A Receptors in Pyramidal and GABAergic Neurons of the Rat Prefrontal Cortex. *Cortex Oct.* **14**, 1100–1109 (2004).
20. Santana, N. & Artigas, F. Expression of Serotonin 2C Receptors in Pyramidal and GABAergic Neurons of Rat Prefrontal Cortex: A Comparison with Striatum. *Cereb. Cortex* **27**, 3125–3139 (2017).
21. Tuerke, K. J., Limebeer, C. L., Fletcher, P. J. & Parker, L. A. Double dissociation between regulation of conditioned disgust and taste avoidance by serotonin availability at the 5-HT(3) receptor in the posterior and anterior insular cortex. *J. Neurosci.* **32**, 13709–17 (2012).
22. Leiser, S. C. *et al.* Serotonergic Regulation of Prefrontal Cortical Circuitries Involved in Cognitive Processing: A Review of Individual 5-HT Receptor Mechanisms and Concerted Effects of 5-HT Receptors Exemplified by the Multimodal Antidepressant Vortioxetine. (2015). doi:10.1021/cn500340j
23. Mansour, A., Fox, C. A., Akil, H. & Watson, S. J. Opioid-receptor mRNA expression in

- the rat CNS: anatomical and functional implications. *Trends in Neurosciences* **18**, 22–29 (1995).
24. Toyoda, H. Role of nicotinic acetylcholine receptors for modulation of microcircuits in the agranular insular cortex. *Journal of Oral Biosciences* **61**, 5–11 (2019).
 25. Takemoto, M., Hasegawa, K., Nishimura, M. & Song, W.-J. The insular auditory field receives input from the lemniscal subdivision of the auditory thalamus in mice. *J. Comp. Neurol.* **522**, 1373–89 (2014).
 26. Barnett, E. M., Evans, G. D., Suq3, N., Perlman, S. & Cassew4, M. D. *Anterograde Tracing of Trigeminal Afferent Pathways from the Murine Tooth Pulp to Cortex Using Herpes Simplex Virus Type 1*. *The Journal of Neuroscience* **15**, (1995).
 27. Oh, S. W. *et al.* A mesoscale connectome of the mouse brain. *Nature* **508**, 207–14 (2014).
 28. Sawatari, H. *et al.* Identification and characterization of an insular auditory field in mice. *Eur. J. Neurosci.* **34**, 1944–1952 (2011).
 29. Rodgers, K. M., Benison, A. M., Klein, A. & Barth, D. S. Auditory, somatosensory, and multisensory insular cortex in the rat. *Cereb. Cortex* **18**, 2941–2951 (2008).
 30. Chen, X., Gabitto, M., Peng, Y., Ryba, N. J. P. & Zuker, C. S. A gustotopic map of taste qualities in the mammalian brain. *Science* **333**, 1262–6 (2011).
 31. Hanamori, T., Kunitake, T., Kato, K. & Kannan, H. Responses of neurons in the insular cortex to gustatory, visceral, and nociceptive stimuli in rats. *J. Neurophysiol.* **79**, 2535–2545 (1998).
 32. Gogolla, N. The insular cortex. *Current Biology* **27**, R580–R586 (2017).
 33. Dixon, M. L., Thiruchselvam, R., Todd, R. & Christoff, K. Emotion and the prefrontal cortex: An integrative review. *Psychol. Bull.* **143**, 1033–1081 (2017).
 34. Ghaziri, J. *et al.* Subcortical structural connectivity of insular subregions. *Sci. Rep.* **8**, (2018).
 35. Mesulam, M.-M. & Mufson, E. J. The Insula of Reil in Man and Monkey. in 179–226 (1985). doi:10.1007/978-1-4757-9619-3_5
 36. Reynolds, S. M. & Zahm, D. S. Specificity in the projections of prefrontal and insular cortex to ventral striatopallidum and the extended amygdala. *J. Neurosci.* **25**, 11757–67 (2005).
 37. Jaramillo, A. A. *et al.* Functional role for suppression of the insular-striatal circuit in modulating interoceptive effects of alcohol. *Addict. Biol.* **23**, 1020–1031 (2018).
 38. Naqvi, N. H. & Bechara, A. The insula and drug addiction: an interoceptive view of

- pleasure, urges, and decision-making. *Brain Struct. Funct.* **214**, 435–50 (2010).
39. Nieuwenhuys, R. The insular cortex: a review. *Prog. Brain Res.* **195**, 123–63 (2012).
 40. (Bud) Craig, A. D. How do you feel — now? The anterior insula and human awareness. *Nat. Rev. Neurosci.* **10**, 59–70 (2009).
 41. Lazar, S. W. *et al.* Meditation experience is associated with increased cortical thickness. *Neuroreport* **16**, 1893–7 (2005).
 42. Laneri, D. *et al.* Mindfulness meditation regulates anterior insula activity during empathy for social pain. *Hum. Brain Mapp.* **38**, 4034–4046 (2017).
 43. Tagliazucchi, E. *et al.* Increased Global Functional Connectivity Correlates with LSD-Induced Ego Dissolution. *Curr. Biol.* **26**, 1043–1050 (2016).
 44. Riba, J. *et al.* Increased frontal and paralimbic activation following ayahuasca, the pan-Amazonian inebriant. *Psychopharmacology (Berl)*. **186**, 93–8 (2006).
 45. Sanches, R. F. *et al.* Antidepressant effects of a single dose of ayahuasca in patients with recurrent depression a SPECT study. *J. Clin. Psychopharmacol.* **36**, 77–81 (2016).
 46. Oppenheimer, S. & Cechetto, D. The Insular Cortex and the Regulation of Cardiac Function. in *Comprehensive Physiology* **6**, 1081–1133 (John Wiley & Sons, Inc., 2016).
 47. Oppenheimer, S. M., Gelb, A., Girvin, J. P. & Hachinski, V. C. Cardiovascular effects of human insular cortex stimulation. *Neurology* **42**, 1727–1727 (1992).
 48. Oppenheimer, S. M. & Cechetto, D. F. Cardiac chronotropic organization of the rat insular cortex. *Brain Res.* **533**, 66–72 (1990).
 49. Marins, F. R. *et al.* Functional topography of cardiovascular regulation along the rostrocaudal axis of the rat posterior insular cortex. *Clin. Exp. Pharmacol. Physiol.* **43**, 484–493 (2016).
 50. Yasui, Y., Breder, C. D., Safer, C. B. & Cechetto, D. F. Autonomic responses and efferent pathways from the insular cortex in the rat. *J. Comp. Neurol.* **303**, 355–374 (1991).
 51. Zhang, Z. & Oppenheimer, S. M. Characterization, distribution and lateralization of baroreceptor-related neurons in the rat insular cortex. *Brain Res.* **760**, 243–250 (1997).
 52. Small, D. M. *et al.* Dissociation of neural representation of intensity and affective valuation in human gustation. *Neuron* **39**, 701–711 (2003).
 53. Veldhuizen, M. G. *et al.* Identification of human gustatory cortex by activation likelihood estimation. *Hum. Brain Mapp.* **32**, 2256–2266 (2011).
 54. Porubská, K., Veit, R., Preissl, H., Fritsche, A. & Birbaumer, N. Subjective feeling of appetite modulates brain activity. An fMRI study. *Neuroimage* **32**, 1273–1280 (2006).

55. Frank, S. *et al.* Processing of food pictures: Influence of hunger, gender and calorie content. *Brain Res.* **1350**, 159–166 (2010).
56. De Araujo, I. E. T., Rolls, E. T., Kringelbach, M. L., McGlone, F. & Phillips, N. Taste-olfactory convergence, and the representation of the pleasantness of flavour, in the human brain. *Eur. J. Neurosci.* **18**, 2059–2068 (2003).
57. Pelchat, M. L., Johnson, A., Chan, R., Valdez, J. & Ragland, J. D. Images of desire: Food-craving activation during fMRI. *Neuroimage* **23**, 1486–1493 (2004).
58. De Araujo, I. E. & Simon, S. A. The gustatory cortex and multisensory integration. *Int. J. Obes.* **33**, S34–S43 (2009).
59. Small, D. M. Flavor is in the brain. *Physiol. Behav.* **107**, 540–552 (2012).
60. Small, D. M. & Prescott, J. Odor/taste integration and the perception of flavor. in *Experimental Brain Research* **166**, 345–357 (2005).
61. De Araujo, I. E. & Rolls, E. T. Representation in the Human Brain of Food Texture and Oral Fat. *J. Neurosci.* **24**, 3086–3093 (2004).
62. DE CELIS ALONSO, B. *et al.* FUNCTIONAL MAGNETIC RESONANCE IMAGING ASSESSMENT OF THE CORTICAL REPRESENTATION OF ORAL VISCOSITY. *J. Texture Stud.* **38**, 725–737 (2007).
63. Brooks, S. J., Cedernaes, J. & Schiöth, H. B. Increased Prefrontal and Parahippocampal Activation with Reduced Dorsolateral Prefrontal and Insular Cortex Activation to Food Images in Obesity: A Meta-Analysis of fMRI Studies. *PLoS One* **8**, (2013).
64. Scott, T. R. Learning through the taste system. *Front. Syst. Neurosci.* (2011). doi:10.3389/fnsys.2011.00087
65. GARCIA, J., KIMELDORF, D. J. & KOELLING, R. A. Conditioned aversion to saccharin resulting from exposure to gamma radiation. *Science* **122**, 157–8 (1955).
66. Welzl, H., D’Adamo, P. & Lipp, H. P. Conditioned taste aversion as a learning and memory paradigm. *Behav. Brain Res.* **125**, 205–213 (2001).
67. Berman, D. E. & Dudai, Y. Memory extinction, learning anew, and learning the new: Dissociations in the molecular machinery of learning in cortex. *Science (80-.)*. **291**, 2417–2419 (2001).
68. Berman, D. E., Hazvi, S., Neduva, V. & Dudai, Y. The role of identified neurotransmitter systems in the response of insular cortex to unfamiliar taste: activation of ERK1-2 and formation of a memory trace. *J. Neurosci.* **20**, 7017–23 (2000).
69. Rosenblum, K., Meiri, N. & Dudai, Y. Taste memory: The role of protein synthesis in

- gustatory cortex. *Behav. Neural Biol.* **59**, 49–56 (1993).
70. Rosenblum, K., Berman, D. E., Hazvi, S., Lamprecht, R. & Dudai, Y. NMDA receptor and the tyrosine phosphorylation of its 2B subunit in taste learning in the rat insular cortex. *J. Neurosci.* **17**, 5129–5135 (1997).
 71. Neseliler, S., Narayanan, D., Fortis-Santiago, Y., Katz, D. B. & Birren, S. J. Genetically induced cholinergic hyper-innervation enhances taste learning. *Front. Syst. Neurosci.* **5**, 97 (2011).
 72. Osorio-Gómez, D., Guzmán-Ramos, K. & Bermúdez-Rattoni, F. Memory trace reactivation and behavioral response during retrieval are differentially modulated by amygdalar glutamate receptors activity: Interaction between amygdala and insular cortex. *Learn. Mem.* **24**, 14–23 (2017).
 73. Lavi, K., Jacobson, G. A., Rosenblum, K. & Lüthi, A. Encoding of Conditioned Taste Aversion in Cortico-Amygdala Circuits. *Cell Rep.* **24**, 278–283 (2018).
 74. Coghill, R. C. *et al.* Distributed processing of pain and vibration by the human brain. *J. Neurosci.* **14**, 4095–4108 (1994).
 75. Coghill, R. C., Sang, C. N., Maisog, J. M. & Iadarola, M. J. Pain intensity processing within the human brain: A bilateral, distributed mechanism. *J. Neurophysiol.* **82**, 1934–1943 (1999).
 76. Lu, C. *et al.* Insular Cortex is Critical for the Perception, Modulation, and Chronification of Pain. *Neuroscience Bulletin* **32**, 191–201 (2016).
 77. Craig, A. D. How do you feel? Interoception: the sense of the physiological condition of the body. *Nat. Rev. Neurosci.* **3**, 655–666 (2002).
 78. Moriarty, O., McGuire, B. E. & Finn, D. P. The effect of pain on cognitive function: A review of clinical and preclinical research. *Progress in Neurobiology* **93**, 385–404 (2011).
 79. De Souza, D. D., Davis, K. D. & Hodaie, M. Reversal of insular and microstructural nerve abnormalities following effective surgical treatment for trigeminal neuralgia. *Pain* **156**, 1112–1123 (2015).
 80. Gogolla, N. The insular cortex. *Current Biology* **27**, R580–R586 (2017).
 81. Paulus, M. P. & Stein, M. B. An Insular View of Anxiety. *Biol. Psychiatry* **60**, 383–387 (2006).
 82. Paulus, M. P. & Stein, M. B. Interoception in anxiety and depression. *Brain Struct. Funct.* 1–13 (2010). doi:10.1007/s00429-010-0258-9
 83. Casanova, J. P., Aguilar-Rivera, M., Rodríguez, M. de los Á., Coleman, T. P. & Torrealba,

- F. The activity of discrete sets of neurons in the posterior insula correlates with the behavioral expression and extinction of conditioned fear. *J. Neurophysiol.* **120**, 1906–1913 (2018).
84. Casanova, J. P. *et al.* A role for the interoceptive insular cortex in the consolidation of learned fear. *Behav. Brain Res.* **296**, 70–77 (2016).
85. Alves, F. H. F. *et al.* Involvement of the insular cortex in the consolidation and expression of contextual fear conditioning. *Eur. J. Neurosci.* **38**, 2300–2307 (2013).
86. Christianson, J. P. *et al.* The sensory insular cortex mediates the stress-buffering effects of safety signals but not behavioral control. *J. Neurosci.* **28**, 13703–13711 (2008).
87. Christianson, J. P. *et al.* Safety Signals Mitigate the Consequences of Uncontrollable Stress Via a Circuit Involving the Sensory Insular Cortex and Bed Nucleus of the Stria Terminalis. *Biol. Psychiatry* **70**, 458–464 (2011).
88. The Expression of the Emotions in Man and Animals - Charles Darwin, Phillip Prodger - Google Books. Available at: https://books.google.de/books?hl=de&lr=&id=TFRtLZSHMcYC&oi=fnd&pg=PR9&ots=Y3lviq_xQ9&sig=-AS-g2bMjsZtndAbuB4CpynIoww&redir_esc=y#v=onepage&q&f=false. (Accessed: 11th November 2019)
89. O’Connell, L. A. & Hofmann, H. A. The Vertebrate mesolimbic reward system and social behavior network: A comparative synthesis. *Journal of Comparative Neurology* **519**, 3599–3639 (2011).
90. Leigh, R. *et al.* Acute lesions that impair affective empathy. *Brain* **136**, 2539–2549 (2013).
91. Ibañez, A., Gleichgerricht, E. & Manes, F. Clinical effects of insular damage in humans. *Brain Struct. Funct.* **214**, 397–410 (2010).
92. Gu, X. *et al.* Anterior insular cortex is necessary for empathetic pain perception. *Brain* **135**, 2726–2735 (2012).
93. Rogers-Carter, M. M. & Christianson, J. P. An insular view of the social decision-making network. *Neurosci. Biobehav. Rev.* **103**, 119–132 (2019).
94. Caria, A. & de Falco, S. Anterior insular cortex regulation in autism spectrum disorders. *Front. Behav. Neurosci.* **9**, 38 (2015).
95. Di Martino, A. *et al.* Relationship between cingulo-insular functional connectivity and autistic traits in neurotypical adults. *Am. J. Psychiatry* **166**, 891–899 (2009).
96. Odriozola, P. *et al.* Insula response and connectivity during social and non-social attention

- in children with autism. *Soc. Cogn. Affect. Neurosci.* **11**, 433–444 (2016).
97. Dumais, K. M., Bredewold, R., Mayer, T. E. & Veenema, A. H. Sex differences in oxytocin receptor binding in forebrain regions: Correlations with social interest in brain region- and sex- specific ways. *Horm. Behav.* **64**, 693–701 (2013).
98. Rogers-Carter, M. M. *et al.* Insular cortex mediates approach and avoidance responses to social affective stimuli. *Nat. Neurosci.* **21**, 404–414 (2018).
99. Rogers-Carter, M. M., Djerdjaj, A., Gribbons, K. B., Varela, J. A. & Christianson, J. P. Insular cortex projections to nucleus accumbens core mediate social approach to stressed juvenile rats. *J. Neurosci.* 0316–19 (2019). doi:10.1523/jneurosci.0316-19.2019
100. Diagnostic and Statistical Manual of Mental Disorders (DSM-5®) - American Psychiatric Association - Google Books. Available at: https://books.google.de/books?hl=de&lr=&id=-JivBAAAQBAJ&oi=fnd&pg=PT18&dq=American+Psychiatric+Association++Diagnostic+and+Statistical+Manual+of+Mental+Disorders+,+American+Psychiatric+Association&ots=ceUN_3KEAc&sig=hMHImXiVZYbQCn3zpU8Iqiz4NrK&redir_esc=y#v=onepage&q=American+Psychiatric+Association+Diagnostic+and+Statistical+Manual+of+Mental+Disorders+%2C+American+Psychiatric+Association&f=false. (Accessed: 5th November 2019)
101. Naqvi, N. H. & Bechara, A. The hidden island of addiction: the insula. *Trends Neurosci.* **32**, 56–67 (2009).
102. Franklin, T. R. *et al.* Decreased gray matter concentration in the insular, orbitofrontal, cingulate, and temporal cortices of cocaine patients. *Biol. Psychiatry* **51**, 134–142 (2002).
103. Naqvi, N. H., Rudrauf, D., Damasio, H. & Bechara, A. Damage to the insula disrupts addiction to cigarette smoking. *Science* **315**, 531–4 (2007).
104. Seif, T. *et al.* Cortical activation of accumbens hyperpolarization-active NMDARs mediates aversion-resistant alcohol intake. *Nat. Neurosci.* **16**, 1094–100 (2013).
105. Kutlu, M. G. *et al.* Role of insular cortex D1 and D2 dopamine receptors in nicotine self-administration in rats. *Behav. Brain Res.* **256**, 273–278 (2013).
106. Etessami, R. *et al.* Spread and pathogenic characteristics of a G-deficient rabies virus recombinant: an in vitro and in vivo study. *J. Gen. Virol.* **81**, 2147–53 (2000).
107. Wickersham, I. R., Finke, S., Conzelmann, K.-K. & Callaway, E. M. Retrograde neuronal tracing with a deletion-mutant rabies virus. *Nat. Methods* **4**, 47–9 (2007).
108. Vélez-Fort, M. *et al.* The stimulus selectivity and connectivity of layer six principal cells reveals cortical microcircuits underlying visual processing. *Neuron* **83**, 1431–43 (2014).

109. Stepien, A. E., Tripodi, M. & Arber, S. Monosynaptic rabies virus reveals premotor network organization and synaptic specificity of cholinergic partition cells. *Neuron* **68**, 456–72 (2010).
110. Vivar, C. *et al.* Monosynaptic inputs to new neurons in the dentate gyrus. *Nat. Commun.* **3**, 1107 (2012).
111. Li, Z. *et al.* Cell-Type-Specific Afferent Innervation of the Nucleus Accumbens Core and Shell. *Front. Neuroanat.* **12**, 84 (2018).
112. Ährlund-Richter, S. *et al.* A whole-brain atlas of monosynaptic input targeting four different cell types in the medial prefrontal cortex of the mouse. *Nat. Neurosci.* **22**, 657–668 (2019).
113. Luo, P. *et al.* Whole brain mapping of long-range direct input to glutamatergic and GABAergic neurons in motor cortex. *Front. Neuroanat.* **13**, 44 (2019).
114. Pollak Dorocic, I. *et al.* A Whole-Brain Atlas of Inputs to Serotonergic Neurons of the Dorsal and Median Raphe Nuclei. *Neuron* **83**, 663–678 (2014).
115. Watabe-Uchida, M., Zhu, L., Ogawa, S. K., Vamanrao, A. & Uchida, N. Whole-brain mapping of direct inputs to midbrain dopamine neurons. *Neuron* **74**, 858–73 (2012).
116. Ogawa, S. K., Cohen, J. Y., Hwang, D., Uchida, N. & Watabe-Uchida, M. Organization of monosynaptic inputs to the serotonin and dopamine neuromodulatory systems. *Cell Rep.* **8**, 1105–1118 (2014).
117. Chamberlin, N. L., Du, B., de Lacalle, S. & Saper, C. B. Recombinant adeno-associated virus vector: use for transgene expression and anterograde tract tracing in the CNS. *Brain Res.* **793**, 169–75 (1998).
118. Xiao, X., Li, J., McCown, T. J. & Samulski, R. J. Gene transfer by adeno-associated virus vectors into the central nervous system. *Exp. Neurol.* **144**, 113–124 (1997).
119. Fenno, L., Yizhar, O. & Deisseroth, K. The development and application of optogenetics. *Annu. Rev. Neurosci.* **34**, 389–412 (2011).
120. Boyden, E. S., Zhang, F., Bamberg, E., Nagel, G. & Deisseroth, K. Millisecond-timescale, genetically targeted optical control of neural activity. *Nat. Neurosci.* **8**, 1263–1268 (2005).
121. Yizhar, O., Fenno, L. E., Davidson, T. J., Mogri, M. & Deisseroth, K. Optogenetics in neural systems. *Neuron* **71**, 9–34 (2011).
122. Zhang, F. *et al.* Optogenetic interrogation of neural circuits: technology for probing mammalian brain structures. *Nat. Protoc.* **5**, 439–56 (2010).
123. Krakauer, J. W., Ghazanfar, A. A., Gomez-Marin, A., MacIver, M. A. & Poeppel, D.

- Neuroscience Needs Behavior: Correcting a Reductionist Bias. *Neuron* **93**, 480–490 (2017).
124. Armbruster, B. N., Li, X., Pausch, M. H., Herlitze, S. & Roth, B. L. Evolving the lock to fit the key to create a family of G protein-coupled receptors potently activated by an inert ligand. *Proc. Natl. Acad. Sci. U. S. A.* **104**, 5163–8 (2007).
 125. Chen, T. W. *et al.* Ultrasensitive fluorescent proteins for imaging neuronal activity. *Nature* **499**, 295–300 (2013).
 126. Helmchen, F. & Denk, W. Deep tissue two-photon microscopy. *Nature Methods* **2**, 932–940 (2005).
 127. Denk, W., Strickler, J. H. & Webb, W. W. Two-photon laser scanning fluorescence microscopy. *Science (80-.)*. **248**, 73–76 (1990).
 128. Hoover, E. E. & Squier, J. A. Advances in multiphoton microscopy technology. *Nat. Photonics* **7**, 93–101 (2013).
 129. Aharoni, D. & Hoogland, T. M. Circuit investigations with open-source miniaturized microscopes: Past, present and future. *Frontiers in Cellular Neuroscience* **13**, (2019).
 130. Zong, W. *et al.* Fast high-resolution miniature two-photon microscopy for brain imaging in freely behaving mice. *Nat. Methods* **14**, 713–719 (2017).
 131. Gunaydin, L. A. *et al.* Natural neural projection dynamics underlying social behavior. *Cell* **157**, 1535–51 (2014).
 132. Cui, G. *et al.* Concurrent activation of striatal direct and indirect pathways during action initiation. *Nature* **494**, 238–242 (2013).
 133. Adelsberger, H., Zainos, A., Alvarez, M., Romo, R. & Konnerth, A. Local domains of motor cortical activity revealed by fiber-optic calcium recordings in behaving nonhuman primates. *Proc. Natl. Acad. Sci. U. S. A.* **111**, 463–468 (2014).
 134. Guo, Q. *et al.* Multi-channel fiber photometry for population neuronal activity recording. *Biomed. Opt. Express* **6**, 3919 (2015).
 135. The study of instinct. - PsycNET. Available at: <https://psycnet.apa.org/record/2004-16480-000>. (Accessed: 19th November 2019)
 136. Walsh, R. N. & Cummins, R. A. The open-field test: A critical review. *Psychol. Bull.* **83**, 482–504 (1976).
 137. Hall, C. S. Emotional behavior in the rat. I. Defecation and urination as measures of individual differences in emotionality. *J. Comp. Psychol.* **18**, 385–403 (1934).
 138. Karl, T., Pabst, R. & von Hörsten, S. Behavioral phenotyping of mice in pharmacological

- and toxicological research. *Exp. Toxicol. Pathol.* **55**, 69–83 (2003).
139. Choleric, E., Thomas, A. W., Kavaliers, M. & Prato, F. S. A detailed ethological analysis of the mouse open field test: Effects of diazepam, chlordiazepoxide and an extremely low frequency pulsed magnetic field. *Neurosci. Biobehav. Rev.* **25**, 235–260 (2001).
140. Wiltschko, A. B. *et al.* Mapping Sub-Second Structure in Mouse Behavior. *Neuron* **88**, 1121–1135 (2015).
141. Handley, S. L. & Mithani, S. Effects of alpha-adrenoceptor agonists and antagonists in a maze-exploration model of 'fear'-motivated behaviour. *Naunyn. Schmiedebergs. Arch. Pharmacol.* **327**, 1–5 (1984).
142. Walf, A. A. & Frye, C. A. The use of the elevated plus maze as an assay of anxiety-related behavior in rodents. *Nat. Protoc.* **2**, 322–328 (2007).
143. Pellow, S., Chopin, P., File, S. E. & Briley, M. Validation of open : closed arm entries in an elevated plus-maze as a measure of anxiety in the rat. *J. Neurosci. Methods* **14**, 149–167 (1985).
144. Handley, S. L. & McBlane, J. W. An assessment of the elevated X-maze for studying anxiety and anxiety-modulating drugs. *J. Pharmacol. Toxicol. Methods* **29**, 129–138 (1993).
145. Carobrez, A. P. & Bertoglio, L. J. Ethological and temporal analyses of anxiety-like behavior: The elevated plus-maze model 20 years on. in *Neuroscience and Biobehavioral Reviews* **29**, 1193–1205 (2005).
146. Tzschentke, T. M. Measuring reward with the conditioned place preference (CPP) paradigm: Update of the last decade. *Addiction Biology* **12**, 227–462 (2007).
147. Stamatakis, A. M. & Stuber, G. D. Activation of lateral habenula inputs to the ventral midbrain promotes behavioral avoidance. *Nat. Neurosci.* **15**, 1105–7 (2012).
148. Peng, Y. *et al.* Sweet and bitter taste in the brain of awake behaving animals. *Nature* **527**, 512–515 (2015).
149. Stamatakis, A. M. *et al.* Lateral Hypothalamic Area Glutamatergic Neurons and Their Projections to the Lateral Habenula Regulate Feeding and Reward. *J. Neurosci.* **36**, (2016).
150. Clarkson, J. M., Dwyer, D. M., Flecknell, P. A., Leach, M. C. & Rowe, C. Handling method alters the hedonic value of reward in laboratory mice. *Sci. Rep.* **8**, (2018).
151. Scheggi, S., De Montis, M. G. & Gambarana, C. Making sense of rodent models of anhedonia. *International Journal of Neuropsychopharmacology* **21**, 1049–1065 (2018).
152. Chevallier, C., Kohls, G., Troiani, V., Brodtkin, E. S. & Schultz, R. T. The social

- motivation theory of autism. *Trends in Cognitive Sciences* **16**, 231–239 (2012).
153. Trezza, V., Campolongo, P. & Vanderschuren, L. J. M. J. Evaluating the rewarding nature of social interactions in laboratory animals. *Developmental Cognitive Neuroscience* **1**, 444–458 (2011).
 154. Crawley, J. N. Designing mouse behavioral tasks relevant to autistic-like behaviors. *Ment. Retard. Dev. Disabil. Res. Rev.* **10**, 248–58 (2004).
 155. Allen, G. V, Saper, C. B., Hurley, K. M. & Cechetto, D. F. Organization of visceral and limbic connections in the insular cortex of the rat. *J. Comp. Neurol.* **311**, 1–16 (1991).
 156. Cauda, F. *et al.* Meta-analytic clustering of the insular cortex. Characterizing the meta-analytic connectivity of the insula when involved in active tasks. *Neuroimage* **62**, 343–355 (2012).
 157. Cechetto, D. F. & Saper, C. B. Evidence for a viscerotopic sensory representation in the cortex and thalamus in the rat. *J. Comp. Neurol.* **262**, 27–45 (1987).
 158. Menon, V. & Uddin, L. Q. Saliency, switching, attention and control: a network model of insula function. *Brain Struct. Funct.* **214**, 655–67 (2010).
 159. Foilb, A. R., Flyer-Adams, J. G., Maier, S. F. & Christianson, J. P. Posterior insular cortex is necessary for conditioned inhibition of fear. *Neurobiol. Learn. Mem.* **134**, 317–327 (2016).
 160. Contreras, M. *et al.* A role for the insular cortex in long-term memory for context-evoked drug craving in rats. *Neuropsychopharmacology* **37**, 2101–8 (2012).
 161. Shi, C. J. & Cassell, M. D. Cortical, thalamic, and amygdaloid connections of the anterior and posterior insular cortices. *J. Comp. Neurol.* **399**, 440–68 (1998).
 162. Shi, C. J. & Cassell, M. D. Cascade projections from somatosensory cortex to the rat basolateral amygdala via the parietal insular cortex. *J. Comp. Neurol.* **399**, 469–91 (1998).
 163. Moraga-amaro, R. & Stehberg, J. The Insular Cortex and the Amygdala : Shared Functions and Interactions. (2012).
 164. Santiago, A. C. & Shammah-Lagnado, S. J. Afferent connections of the amygdalopiriform transition area in the rat. *J. Comp. Neurol.* **489**, 349–71 (2005).
 165. Gehrlach, D. A. *et al.* Aversive state processing in the posterior insular cortex. *Nat. Neurosci.* **22**, 1424–1437 (2019).
 166. Malach, R. & Graybiel, A. M. Mosaic architecture of the somatic sensory-recipient sector of the cat's striatum. *J. Neurosci.* **6**, 3436–3458 (1986).
 167. Alexander, G. Parallel Organization of Functionally Segregated Circuits Linking Basal

- Ganglia and Cortex. *Annu. Rev. Neurosci.* **9**, 357–381 (1986).
168. Graybiel, A. M. & Grafton, S. T. The striatum: where skills and habits meet. *Cold Spring Harb. Perspect. Biol.* **7**, a021691 (2015).
169. Hunnicutt, B. J. *et al.* A comprehensive excitatory input map of the striatum reveals novel functional organization. *Elife* **5**, (2016).
170. Craig, A. D. B. How do you feel--now? The anterior insula and human awareness. *Nat. Rev. Neurosci.* **10**, 59–70 (2009).
171. Gehrlach, D. A. *et al.* Aversive state processing in the posterior insular cortex. *Nat. Neurosci.* **22**, 1424–1437 (2019).
172. Christianson, J. P. *et al.* Safety signals mitigate the consequences of uncontrollable stress via a circuit involving the sensory insular cortex and bed nucleus of the stria terminalis. *Biol. Psychiatry* **70**, 458–464 (2011).
173. Tye, K. M. *et al.* Amygdala circuitry mediating reversible and bidirectional control of anxiety. *Nature* **471**, 358–62 (2011).
174. Felix-Ortiz, A. C. *et al.* BLA to vHPC inputs modulate anxiety-related behaviors. *Neuron* **79**, 658–664 (2013).
175. Corral-Frias, N. S., Lahood, R. P., Edelman-Vogelsang, K. E., French, E. D. & Fellous, J. M. Involvement of the ventral tegmental area in a rodent model of post-traumatic stress disorder. *Neuropsychopharmacology* **38**, 350–363 (2013).
176. Fadok, J. P., Markovic, M., Tovote, P. & Lüthi, A. New perspectives on central amygdala function. *Curr. Opin. Neurobiol.* **49**, 141–147 (2018).
177. Russo, S. J. & Nestler, E. J. The brain reward circuitry in mood disorders. *Nat. Rev. Neurosci.* **14**, 609–25 (2013).
178. Schiff, H. *et al.* An insula-central amygdala circuit for guiding tastant-reinforced choice behavior. *J. Neurosci.* (2018). doi:10.1523/JNEUROSCI.1773-17.2017
179. Castro, D. C. & Berridge, K. C. Opioid hedonic hotspot in nucleus accumbens shell: Mu, delta, and kappa maps for enhancement of sweetness ‘liking’ and ‘wanting’. *J. Neurosci.* **34**, 4239–4250 (2014).
180. O’Connor, E. C. *et al.* Accumbal D1R Neurons Projecting to Lateral Hypothalamus Authorize Feeding. *Neuron* **88**, 553–564 (2015).
181. Cai, H., Haubensak, W., Anthony, T. E. & Anderson, D. J. Central amygdala PKC- δ (+) neurons mediate the influence of multiple anorexigenic signals. *Nat. Neurosci.* **17**, 1240–8 (2014).

182. Douglass, A. M. *et al.* Central amygdala circuits modulate food consumption through a positive-valence mechanism. *Nat. Neurosci.* **20**, 1384–1394 (2017).
183. Mufson, E. J., Mesulam, M.-M. & Pandya, D. N. Insular interconnections with the amygdala in the rhesus monkey. *Neuroscience* **6**, 1231–1248 (1981).
184. Stuber, G. D. *et al.* Excitatory transmission from the amygdala to nucleus accumbens facilitates reward seeking. *Nature* **475**, 377–80 (2011).
185. Carlezon, W. A. & Thomas, M. J. Biological substrates of reward and aversion: A nucleus accumbens activity hypothesis. *Neuropharmacology* **56**, 122–132 (2009).
186. Mahn, M., Prigge, M., Ron, S., Levy, R. & Yizhar, O. Biophysical constraints of optogenetic inhibition at presynaptic terminals. *Nat. Neurosci.* **19**, 554–6 (2016).
187. Contreras, M., Ceric, F. & Torrealba, F. Inactivation of the interoceptive insula disrupts drug craving and malaise induced by lithium. *Science* **318**, 655–8 (2007).
188. Blonde, G. D., Bales, M. B. & Spector, A. C. Extensive Lesions in Rat Insular Cortex Significantly Disrupt Taste Sensitivity to NaCl and KCl and Slow Salt Discrimination Learning. *PLoS One* **10**, e0117515 (2015).
189. Schier, L. A., Blonde, G. D. & Spector, A. C. Bilateral lesions in a specific subregion of posterior insular cortex impair conditioned taste aversion expression in rats. *J. Comp. Neurol.* (2015). doi:10.1002/cne.23822
190. Fendt, M. & Endres, T. 2,3,5-Trimethyl-3-thiazoline (TMT), a component of fox odor – Just repugnant or really fear-inducing? *Neurosci. Biobehav. Rev.* **32**, 1259–1266 (2008).
191. Sparta, D. R., Jennings, J. H., Ung, R. L. & Stuber, G. D. Optogenetic strategies to investigate neural circuitry engaged by stress. *Behav. Brain Res.* **255**, 19–25 (2013).
192. Grossman, N. *et al.* The spatial pattern of light determines the kinetics and modulates backpropagation of optogenetic action potentials. *J. Comput. Neurosci.* **34**, 477–88 (2013).
193. Kuczewski, N., Porcher, C., Lessmann, V., Medina, I. & Gaiarsa, J.-L. Back-propagating action potential: A key contributor in activity-dependent dendritic release of BDNF. *Commun. Integr. Biol.* **1**, 153–5 (2008).
194. Accolla, R. & Carleton, A. Internal body state influences topographical plasticity of sensory representations in the rat gustatory cortex. *Proc. Natl. Acad. Sci. U. S. A.* **105**, 4010–5 (2008).
195. Samuelson, C. L., Gardner, M. P. H. & Fontanini, A. Thalamic contribution to cortical processing of taste and expectation. *J. Neurosci.* **33**, 1815–27 (2013).

196. Beier, K. T. *et al.* Circuit Architecture of VTA Dopamine Neurons Revealed by Systematic Input-Output Mapping. *Cell* **162**, 622–634 (2015).
197. Do, J. P. *et al.* Cell type-specific long-range connections of basal forebrain circuit. *Elife* **5**, e13214 (2016).
198. Wall, N. R. *et al.* Brain-wide maps of synaptic input to cortical interneurons. *J. Neurosci.* **36**, 4000–4009 (2016).
199. Kim, J., Pignatelli, M., Xu, S., Itohara, S. & Tonegawa, S. Antagonistic negative and positive neurons of the basolateral amygdala. *Nat. Neurosci.* **19**, 1636–1646 (2016).
200. Alheid, G. F., Shammah-Lagnado, S. J. & Beltramino, C. A. The interstitial nucleus of the posterior limb of the anterior commissure: A novel layer of the central division of extended amygdala. in *Annals of the New York Academy of Sciences* **877**, 645–654 (New York Academy of Sciences, 1999).
201. Shammah-Lagnado, S. J., Alheid, G. F. & Heimer, L. Afferent connections of the interstitial nucleus of the posterior limb of the anterior commissure and adjacent amygdalostratial transition area in the rat. *Neuroscience* **94**, 1097–123 (1999).
202. Avery, J. A. *et al.* Major depressive disorder is associated with abnormal interoceptive activity and functional connectivity in the insula. *Biol. Psychiatry* **76**, 258–266 (2014).
203. Guo, W. *et al.* Decreased insular connectivity in drug-naive major depressive disorder at rest. *J. Affect. Disord.* **179**, 31–37 (2015).
204. Yarmolinsky, D. A., Zuker, C. S. & Ryba, N. J. P. Common Sense about Taste: From Mammals to Insects. *Cell* **139**, 234–244 (2009).
205. Livneh, Y. *et al.* Homeostatic circuits selectively gate food cue responses in insular cortex. *Nature* **546**, 611–616 (2017).
206. Schiff, H. C. *et al.* An Insula-Central Amygdala Circuit for Guiding Tastant-Reinforced Choice Behavior. *J. Neurosci.* **38**, 1418–1429 (2018).
207. Berret, E. *et al.* Insular cortex processes aversive somatosensory information and is crucial for threat learning. *Science* **364**, eaaw0474 (2019).
208. Zucker, N. L. *et al.* The Clinical Significance of Posterior Insular Volume in Adolescent Anorexia Nervosa. *Psychosom. Med.* **79**, 1025–1035
209. Jaramillo, A. A., Van Voorhies, K., Randall, P. A. & Besheer, J. Silencing the insular-striatal circuit decreases alcohol self-administration and increases sensitivity to alcohol. *Behav. Brain Res.* **348**, 74–81 (2018).
210. Jaramillo, A. A. *et al.* Functional role for cortical-striatal circuitry in modulating alcohol

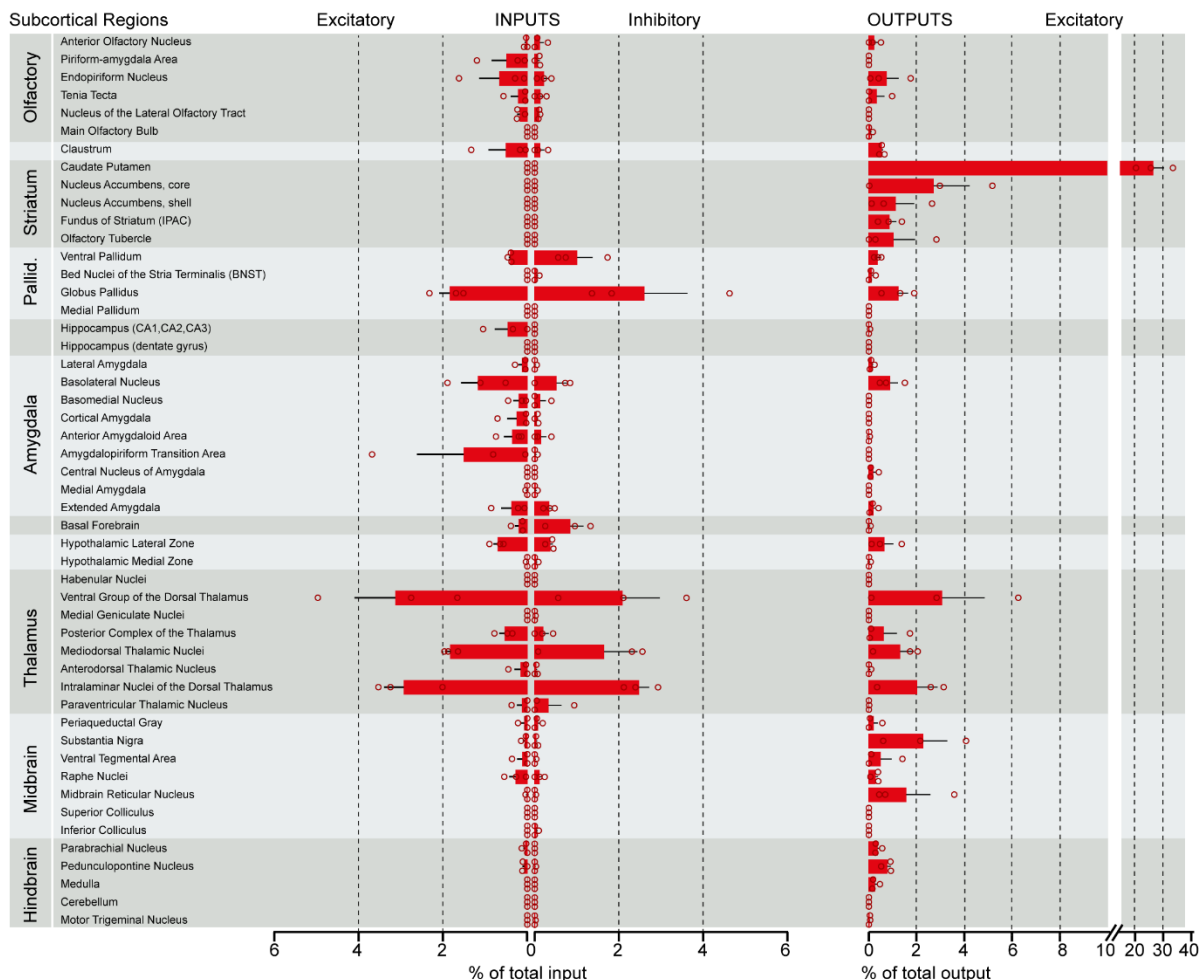
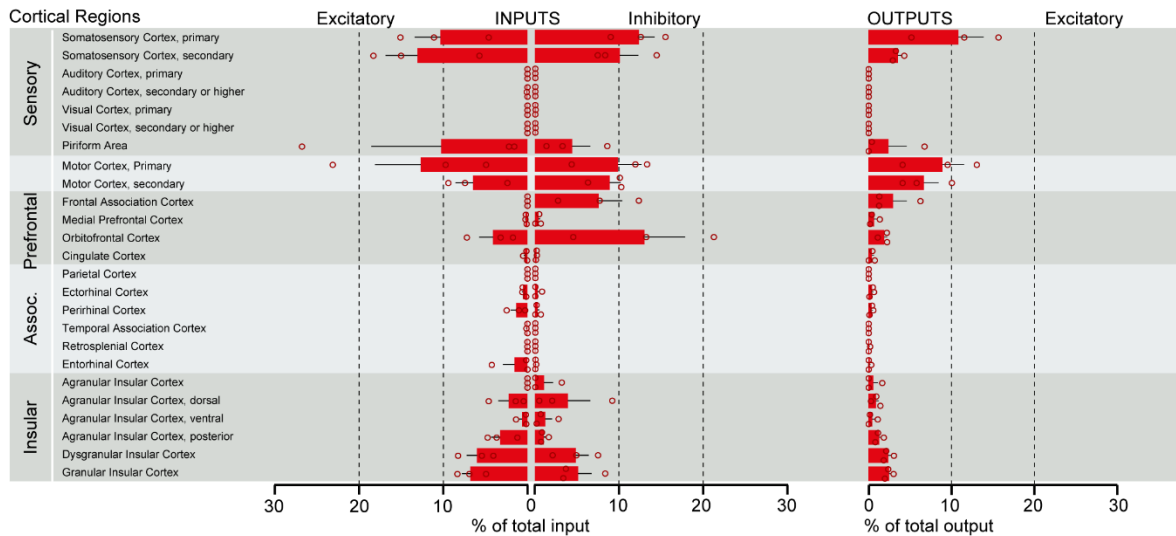
- self-administration. *Neuropharmacology* **130**, 42–53 (2018).
211. Parkes, S. L., Bradfield, L. A. & Balleine, B. W. Interaction of insular cortex and ventral striatum mediates the effect of incentive memory on choice between goal-directed actions. *J. Neurosci.* **35**, 6464–6471 (2015).
212. Zhang, R. *et al.* A glutamatergic insular-striatal projection regulates the reinstatement of cue-associated morphine-seeking behavior in mice. *Brain Res. Bull.* **152**, 257–264 (2019).
213. Knowland, D. *et al.* Distinct Ventral Pallidal Neural Populations Mediate Separate Symptoms of Depression. *Cell* **170**, 284–297.e18 (2017).
214. Zingg, B. *et al.* AAV-Mediated Anterograde Transsynaptic Tagging: Mapping Corticocollicular Input-Defined Neural Pathways for Defense Behaviors. *Neuron* **93**, 33–47 (2017).
215. Hintiryan, H. *et al.* The mouse cortico-striatal projectome. *Nat. Neurosci.* **19**, 1100–1114 (2016).
216. Maffei, A., Haley, M. & Fontanini, A. Neural processing of gustatory information in insular circuits. *Curr. Opin. Neurobiol.* **22**, 709–716 (2012).
217. McDonald, A. J., Shammah-Lagnado, S. J., Shi, C. & Davis, M. Cortical afferents to the extended amygdala. in *Annals of the New York Academy of Sciences* **877**, 309–338 (New York Academy of Sciences, 1999).
218. Reep, R. L. & Winans, S. S. Efferent connections of dorsal and ventral agranular insular cortex in the hamster, *Mesocricetus auratus*. *Neuroscience* **7**, 2609–2635 (1982).
219. Mowiol mounting medium. *Cold Spring Harb. Protoc.* **2006**, pdb.rec10255 (2006).
220. Kamentsky, L. *et al.* Systems biology Improved structure, function and compatibility for CellProfiler: modular high-throughput image analysis software. *Bioinforma. Appl. NOTE* **27**, 1179–1180 (2011).
221. Grider, M. H., Chen, Q. & David Shine, H. Semi-automated quantification of axonal densities in labeled CNS tissue. *J. Neurosci. Methods* **155**, 172–179 (2006).

6 APPENDICES

APPENDIX 1	108
APPENDIX 2	109
APPENDIX 3	110
APPENDIX 4	111
APPENDIX 5	112
APPENDIX 6	113
APPENDIX 7	114

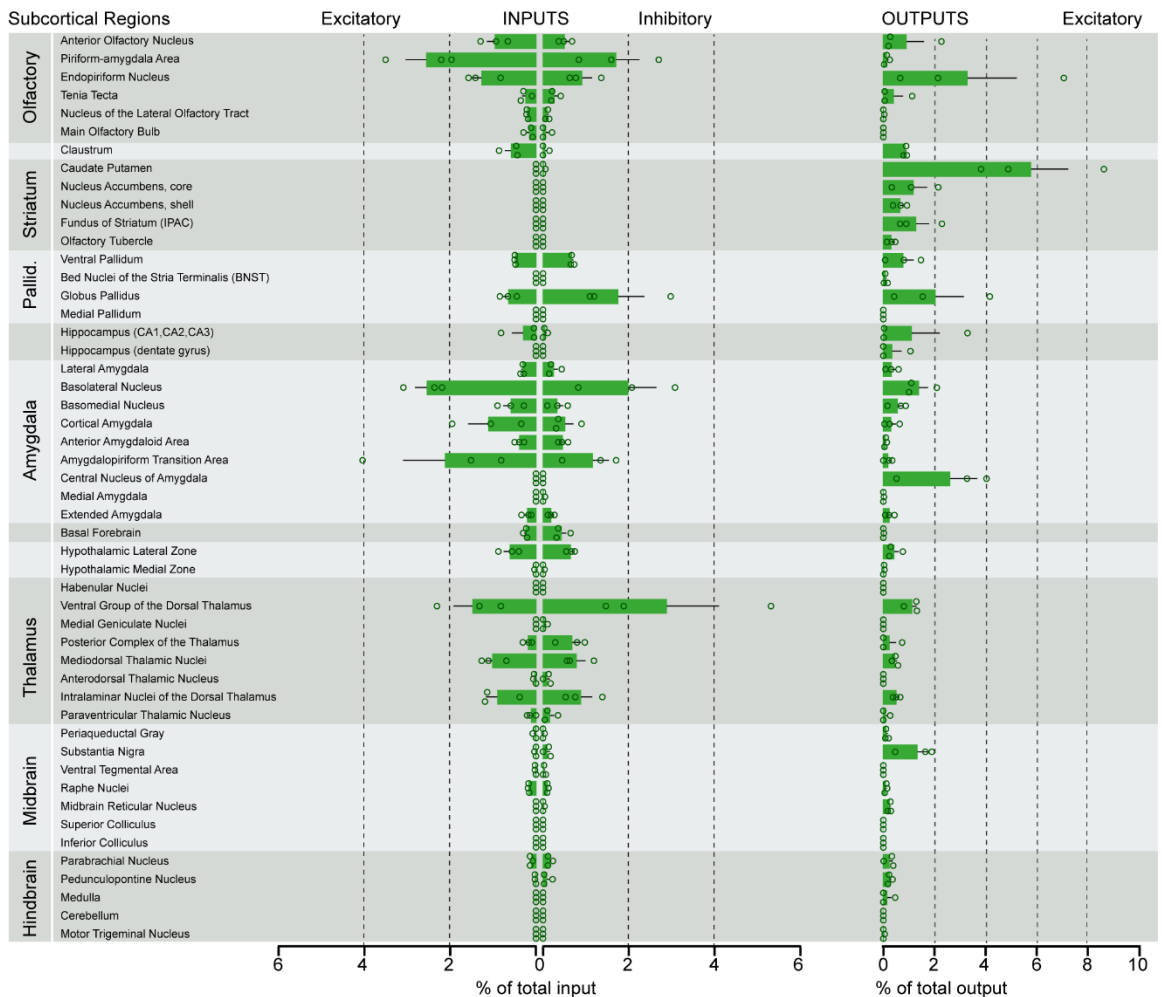
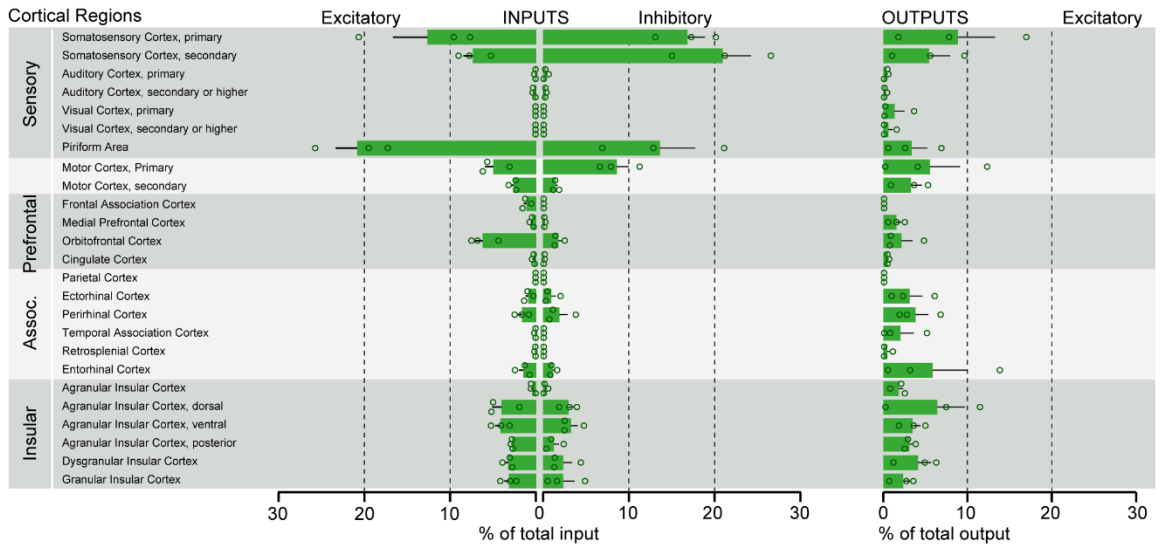
APPENDIX 1

Input/Output map for aIC



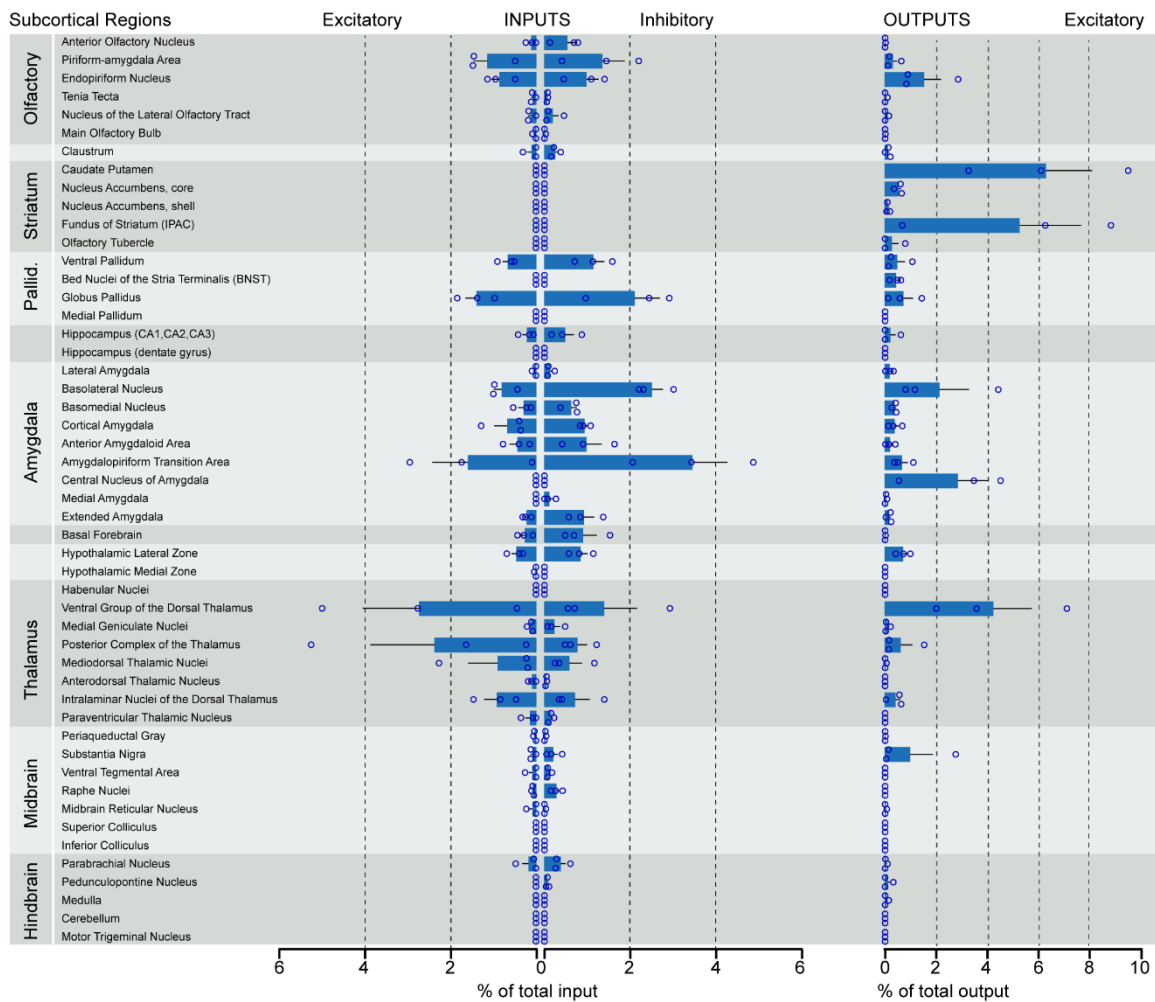
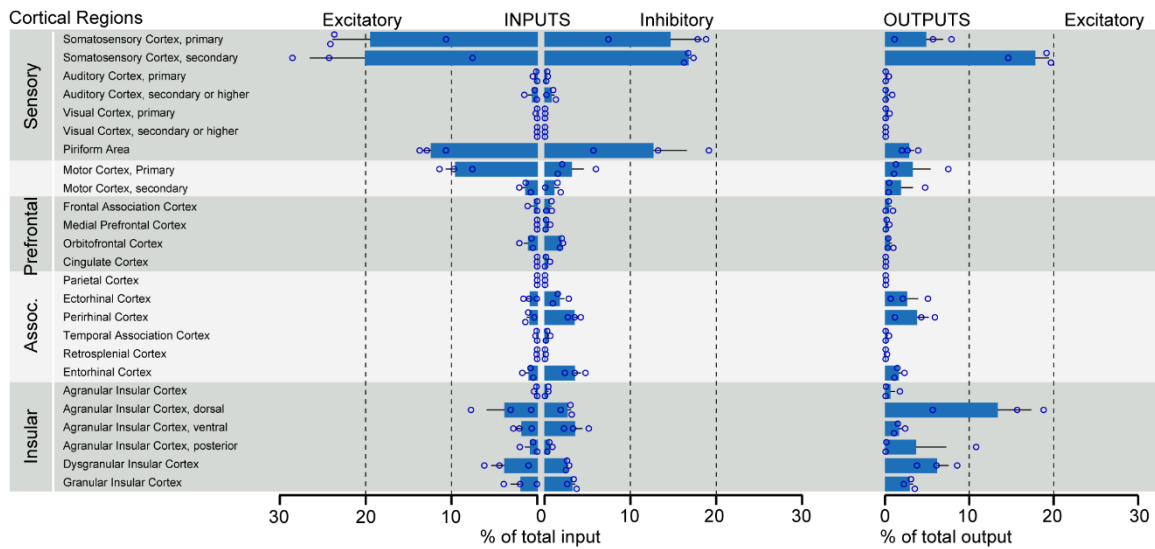
APPENDIX 2

Input/Output map for mIC

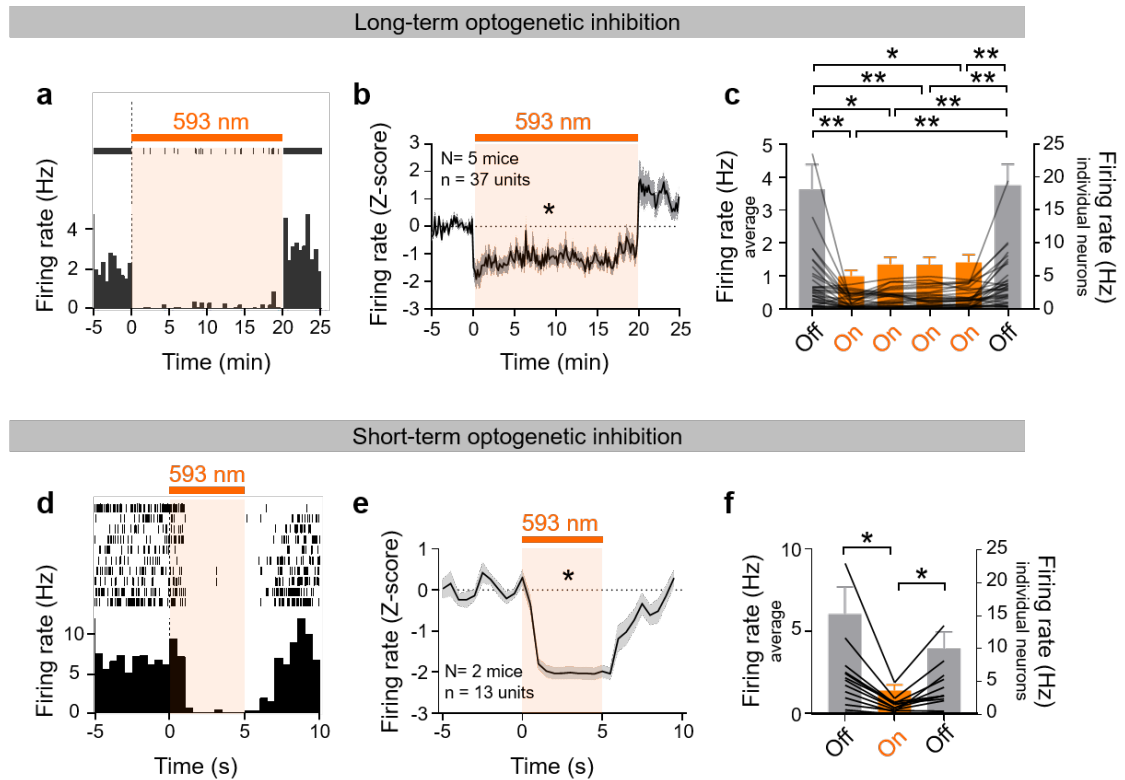


APPENDIX 3

Input/Output map for pIC

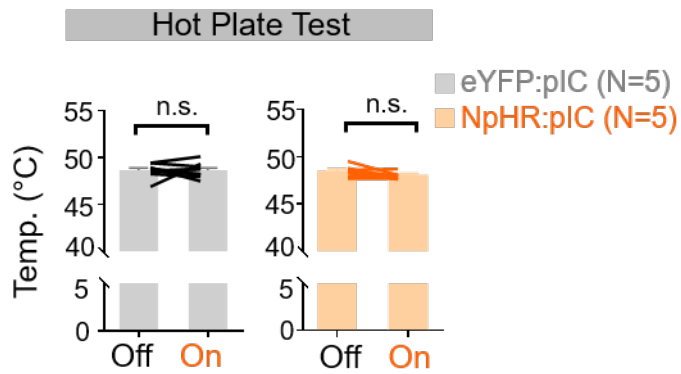


APPENDIX 4



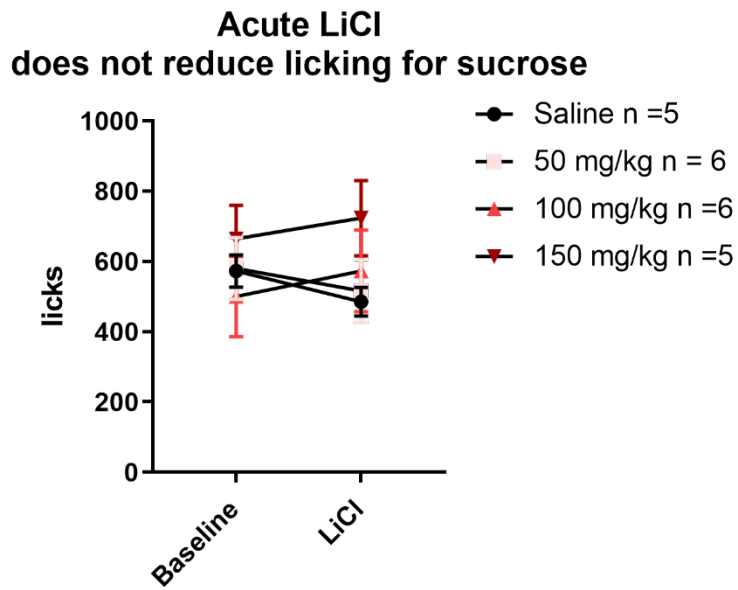
a - c, Long-term optogenetic inhibition in mice expressing AAV2/5-CaMKIIa-eNpHR3.0-EYFP. **a**, Reduced firing rate of a representative pIC neuron during 20 min photostimulation (bin size = 30 s). **b**, Average z-scored firing rates from 37 single units recorded in 5 mice reveal significantly reduced activity during 20 min photostimulation (bin size = 10 s, one sample t-test with theoretical mean = 0, $t = 42.95$, $df = 119$, $*P < 0.0001$). **c**, Average and individual firing rates of 37 pIC neurons in 5 min bins are significantly reduced during 20 min photostimulation (one-way repeated measures ANOVA $F_{1,814,65,29} = 12.37$, $P < 0.0001$, Bonferroni post-hoc analysis revealed significant differences pre- or post-inhibition $**P < 0.01$, $*P < 0.05$). **d-f**, Short-term optogenetic inhibition in mice expressing AAV2/5-CaMKIIa-eNpHR3.0-EYFP. **d**, Peri-stimulus time histogram (PSTH) indicates reliably reduction of firing rates of a representative pIC neuron during 10 repetitions of 5 s long photostimulations (bin size = 500 ms). **e**, Average z-scored firing rates from 13 single units recorded in 2 mice reveal significantly reduced activity during 5 s long photostimulations (bin size = 500 ms, one sample t-test with theoretical mean = 0, $t = 5.967$, $df = 9$, $*P = 0.0002$). **f**, Average and individual firing rates of 13 pIC neurons in 5 s bins are significantly reduced during 5 s photostimulation (one-way repeated measures ANOVA $F_{1,295,15,54}$, $P = 0.0026$, Bonferroni post-hoc: significant for pre- or post-inhibition $*P < 0.05$).

APPENDIX 5



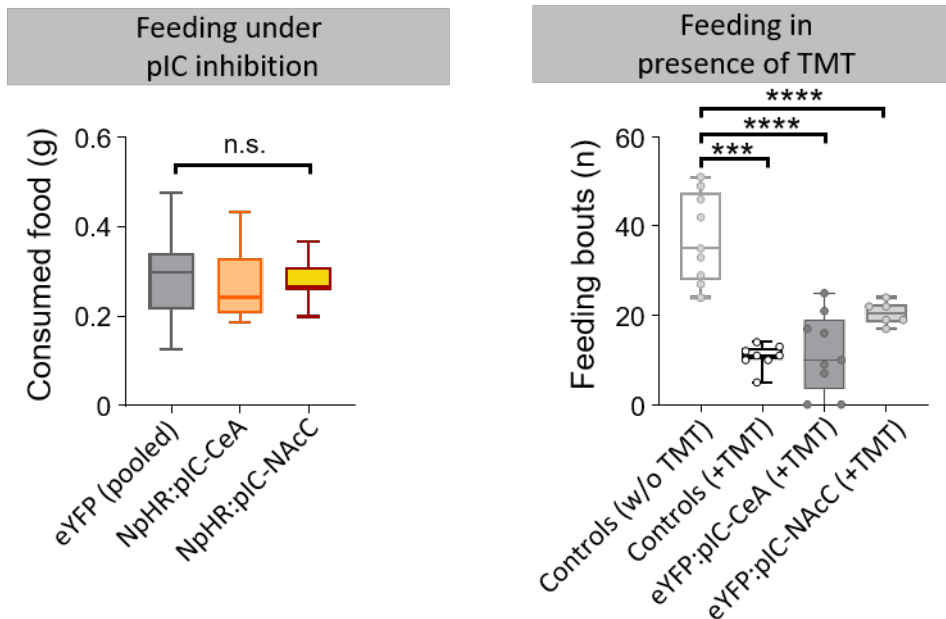
Ramping hot plate test (nociception control). Temperature thresholds did not change for NpHR-expressing or eYFP-expressing mice between light 'off' and 'on' conditions ($n = 5$ eYFP mice: two-tailed paired t test, $t = 0.02949$, $df = 9$, $p = 0.9771$; $n = 5$ NpHR mice: two-tailed paired t test, $t = 1.967$, $df = 9$, $p = 0.0807$). Data is shown as means + s.e.m.

APPENDIX 6



24-h water-deprived mice were administered (i.p.) with Saline or escalating doses of LiCl, but they did not significantly reduce their licking for a 10 % sucrose solution (for LiCl-dose: 2-way ANOVA, $F(3, 18) = 0.9164$, $p=0.4528$). This indicated that visceral malaise couldn't overcome thirst or the reward value of sucrose.

APPENDIX 7



left, Under naïve conditions, neither NpHR-mediated inhibition of the pIC-CeA ($n=7$) nor the pIC-NAcc ($n=10$) pathway changes feeding behavior in 24-h food deprived animals compared to controls (controls were pooled: eYFP:pIC-CeA, $n=10$, and eYFP:pIC-NAcc, $n=10$; one-way ANOVA, $F(2, 34) = 0.1531$, $p = 0.8586$). Trial duration 20 min.

right, Feeding bouts are significantly reduced in presence of TMT. Control feeding in absence of TMT (controls w/o TMT, $n = 9$) was significantly more frequent than in presence of TMT (controls +TMT, $n = 8$), in eYFP expressing controls as shown in Fig. 8q (eYFP:pIC-CeA (+TMT), $n = 9$), or than in eYFP-expressing controls shown in Fig. 8r (eYFP:pIC-NAcc (+TMT), $n = 6$). One-way ANOVA, $F(3, 28) = 24.98$, $****p = 0.0043$; Bonferroni post-hoc analyses comparing all TMT treated conditions to the no TMT control revealed significant differences ($****p < 0.0001$, $***p = 0.0005$)